DISSERTATION

PRECISION MEASUREMENT AND SYMMETRY PROPERTIES OF METASTABLE HYDROGEN

Submitted by

Cory M. Rasor

Department of Physics

In partial fulfillment of the requirements

For the Degree of Doctor of Philosophy

Colorado State University

Fort Collins, Colorado

Fall 2022

Doctoral Committee:

Advisor: Dylan Yost

Jacob Roberts
Michael Mooney
Randy Bartels

ABSTRACT

PRECISION MEASUREMENT AND SYMMETRY PROPERTIES OF METASTABLE HYDROGEN

Hydrogen has been an indispensable system to study during the development of quantum mechanics due to the simplicity of its atomic structure. Hydrogen maintains its utility today as an important tool for determining fundamental values such as the Rydberg and fine structure constants, as well as the proton charge radius. The work described in this thesis aims to use hydrogen for determining the proton Zemach radius, to search for anomalous spin-dependent forces, and to provide means for measuring the degree of parity violation within this simple system. An overview of a $2S_{1/2}$ hyperfine interval measurement is described, followed by a description of the apparatus used and finally a discussion of the systematic effects to be characterized. A proposed parity violation experiment is also described.

DEDICATION

For Haidyn, to whom I owe everything.

TABLE OF CONTENTS

LIST OF TABLES

LIST OF FIGURES

Chapter 1

Introduction

The Standard Model of Particle Physics (SM) is a well-grounded theory of interactions involving leptons and quarks, mediated by a variety of gauge bosons. Since the unification of electroweak interactions during the 1970s, the SM has been incredibly accurate in describing interactions between constituent particles and has also been very precise in its predictive power; for example, the electron magnetic moment is predicted at 0.24 ppt and has been measured in good agreement at a level of 0.28 ppt [3]. Despite its great success, however, the SM is incomplete, as many unanswered questions exist which cannot be explained with this model alone. For example, phenomena such as gravity, dark matter, dark energy are entirely absent from the Model. Matter-antimatter asymmetry and inflation are also unexplained. To aide in the resolution of these deficiencies, or perhaps work towards a so-called "theory of everything," many experiments look for signs of physics beyond the standard model that may help bridge the knowledge gap between the current SM and unexplained phenomenon. The work presented in this thesis works towards searching for BSM physics by exploring high precision measurements in metastable atomic hydrogen.

1.1 Outline of Thesis

An experiment designed to search for an anomalous, spin-dependent force through hydrogen spectroscopy of the $2S_{1/2}$ hyperfine interval is the main topic of this thesis. This force could be caused by the elusive, proposed dark matter candidate – the axion. Chapter 2 discusses a radio-frequency Ramsey-spectroscopy apparatus, built to drive magnetic dipole transitions of the $2S$ hyperfine interval. To produce metastable hydrogen atoms for this experiment, a 243 nm radiation system was developed. Section 2.6 describes the details of this system. Systematic characterizations and future work in measuring the hyperfine interval are discussed.

Having generated a beam of metastable hydrogen atoms, the prospect of designing a new experiment involving symmetry arose. Chapter 3 discusses an experimental proposal to measure parity

violation in a cold atomic beam of hydrogen, with the intention of extracting the Weinberg mixing angle at low momentum transfer and checking for deviations from the SM predictions, possibly caused by dark Z bosons.

Lastly, in Appendix A, work towards laser cooling antihydrogen is described. Goals to perform high precision spectroscopy on antihydrogen required trapped, laser-cooled antihydrogen atoms. However, the laser-cooling cycling transition for antihydrogen atoms involves 121 nm (Lyman-α) radiation, which has been historically difficult to generate. To this end, a record-setting Lyman-α source is detailed here.

Chapter 2

Hydrogen 2S Hyperfine Interval

2.1 Background

Hydrogen is an excellent testing ground for developing our understanding of bound-state physics. Due to its simple structure, comprising one electron and one proton, it has been paramount in pushing the bounds of our theoretical framework for over a century. Numerous comparisons between theory and experimental results have continually verified and refined models of electromagnetic interactions within bound-state systems. Additionally, measuring frequency transitions in hydrogen has led to the extraction of fundamental constants such as the Rydberg constant, from which the fine structure constant can be determined, and the proton radius [4].

One value of particular interest is the Zemach radius, defined as the convolution of electric charge radius $\rho_e(\mathbf{r})$ and magnetic moment $\rho_m(\mathbf{r})$ distribution [5]:

$$r_Z = \int \mathbf{r} \int \rho_e(\mathbf{r}-\mathbf{r}')\rho_m(\mathbf{r}')d\mathbf{r}'d\mathbf{r}. \tag{2.1}$$

The presence of this electric charge and magnetic moment distribution provides an additional frequency shift to the $S_{1/2}$ state energy levels within the hydrogen atom in the form

$$\Delta\nu_{\text{hfs}} = \nu_F(1-2\alpha m_r r_Z), \tag{2.2}$$

where α is the fine structure constant, m_r is the reduced mass of hydrogen and ν_F is the Fermi energy. Similar to the electric charge radius, the Zemach radius has been measured through means of electron-proton scattering, hydrogen spectroscopy, and muonic hydrogen spectroscopy [6–8]. While there is currently no discrepancy between Zemach radius results like there is with the electric charge radius alone, the uncertainties on the Zemach radius are too large to note any significant disagreement [7]. One aim of this work is to measure the $2S_{1/2}$ hyperfine interval in hydrogen for

the purpose of making a more precise determination of the Zemach radius for later comparisons with ongoing muonic hydrogen experiments [7].

Moreover, the main goal, in conjunction with measuring the proton Zemach radius, is to test high-order QED theory with the same precision measurement of $2S_{1/2}^{\text{hfs}}$ by determining the Sternheim interval [9], defined as

$$D_{21} = 8\nu_2^{\text{hfs}} - \nu_1^{\text{hfs}}. \tag{2.3}$$

Due to complicated proton structure, theoretical predictions for the hyperfine intervals are limited to fractional uncertainties on the order of $10^4 - 10^5$ [10, 11]. However, because the proton structure effects are nearly identical in S states, the difference between $2S_{1/2}^{\text{hfs}}$ and $1S_{1/2}^{\text{hfs}}$ mitigates the proton structure and allows higher order effects to be considered. The predicted value for this value is $D_{21}^{\text{th}} = 48.953(3)$ kHz [12], while measured values taking the best known $1S_{1/2}$ and $2S_{1/2}$ hyperfine values gives $D_{21}^{\text{exp}} = 48.923(54)$ kHz [12]. The leading effects in D_{21} which limit the precision to 3 Hz are due to third- and fourth-order QED corrections, while the limiting factor in the experimental precision is the $2S_{1/2}$ hyperfine interval uncertainty of 6.7 Hz.

This thesis describes progress towards measuring the $2S_{1/2}$ hyperfine interval to a precision of 1 Hz in order to perform a high precision comparison to theory as a test of QED. Any deviation from QED predictions could have implications hinting at beyond-standard-model (BSM) physics. Specifically, a shift in the Sternheim interval could exist in the presence of an anomalous spin-dependent force [12]. Such a force could be an indication of the axion – a proposed dark matter candidate [13–16].

2.2 Previous Measurements

To determine the Sternheim interval D_{21}, a high precision measurement of both the ground and metastable hyperfine intervals are needed. The ground state hyperfine interval has been measured using masers, making it one of the most precisely known frequency splittings in hydrogen with a fractional frequency uncertainty of on the order of 10^{-13} [17]. Conversely, the metastable hyper-

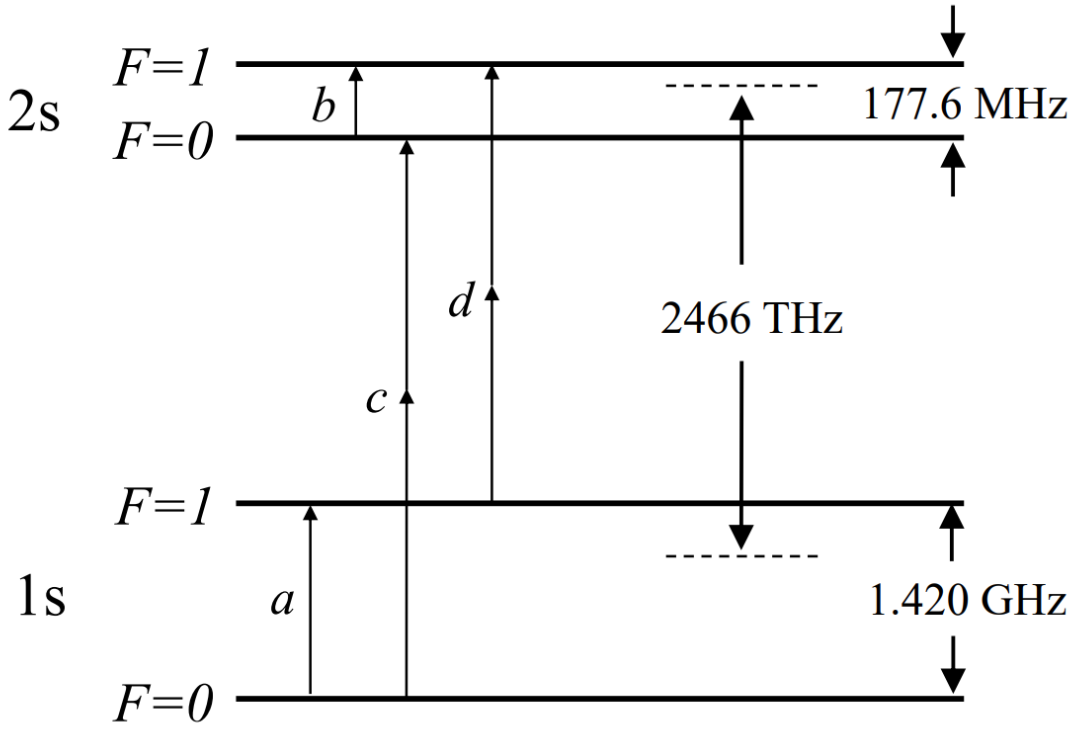

Figure 2.1: Relevant energy levels for each of the previous hyperfine measurements. The two RF experiments measure b directly. Optical determinations were performed by measuring c and d directly and using the highly precise measured value of the ground state hyperfine interval a. The combination $a+d-c$ results in the $2s$ hyperfine interval.

fine interval has only been measured four times before and currently holds a fractional frequency uncertainty of about 4×10^{-8} [18]. Each of the measurements has improved upon prior results as technology and scientific techniques have been invented and refined. The basic idea behind each of these measurements are as follows:

1. 1956 – RF Ramsey spectroscopy using a hydrogen beam traveling at 500 m/s lead to an uncertainty of 50 Hz [19]

2. 2000 – RF Rabi frequency in a 1 m long waveguide with atoms traveling at 2600 m/s lead to an uncertainty of 29 Hz. [20]

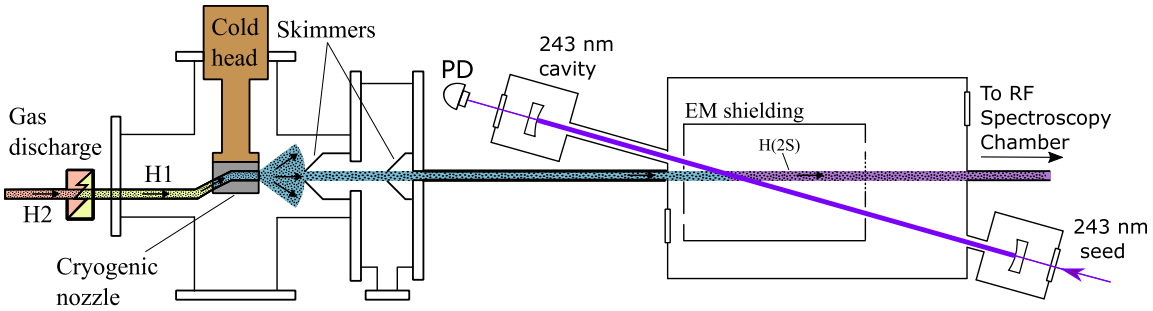

Figure 2.2: Metastable hydrogen beam apparatus. Hydrogen molecules are dissociated in an RF discharge and the atoms are then cooled on a cryogenic nozzle through wall collisions down to 4.5 K. Skimmers are used to generate a collimated beam, which then intersects 243 nm radiation for $1S \rightarrow 2S$ excitation. Following excitation, the beam flows to a spectroscopy chamber.

3. 2004 – Optical spectroscopy of the $1S_{1/2} \rightarrow 2S_{1/2}$ transition from $F = 0 \rightarrow F = 0$ and $F = 1 \rightarrow F = 1$ with atoms cooled to cryogenic temperatures of 5 K, leading to an uncertainty of 16 Hz. [21]

4. 2009 – Optical spectroscopy, with improved frequency referencing leads to the most precise measurement to date with an uncertainty of 6.7 Hz. [18]

While RF Ramsey spectroscopy has been performed before, as well as spectroscopy of a cryogenic hydrogen beam, our goal was to combine the benefits of both systems to conduct a spectroscopic measurement using Ramsey spectroscopy on a cryogenic beam. The main advantage of using separated oscillatory fields is the long interaction length that is possible with this setup, which along with the use of a cold atomic beam, nets a long interaction time. With a cryogenically-cooled atomic hydrogen beam (at 4.5 K) with a well characterized velocity distribution at an average of 450 m/s (as we have demonstrated [22]), an interaction region of only 30 cm can produce Ramsey fringes with linewidths of $2S^{\text{hfs}}_{1/2}$ as low as 700 Hz. For an initial goal of measuring $2S^{\text{hfs}}_{1/2}$ with a 1 Hz uncertainty, we only need to determine the line center of such a line by about 0.1%. Increasing the precision is straightforward after the first demonstrations by either lengthening the interaction region, or by only measuring the slowest velocity classes by time-of-flight selection.

2.3 Overview of Measurement

This experiment starts with a bottle of molecular hydrogen whose gas flows into a microwave discharge to separate the molecules into atomic hydrogen. These atoms are cooled through collisions on a cryogenically-cooled nozzle before passing through a pair of skimmers to generate a collimated beam. The atoms intersect a 243 nm radiation source to selectively populate the metastable $2S_{1/2}$, $F = 0$ state. The beam of metastable atoms flows into another chamber where Ramsey spectroscopy is conducted using a pair of coils to produce separated oscillatory fields. The entire interaction region is magnetically shielding. After atoms are transferred to the $F = 1$ state, a second resonant RF region quenches remaining $F = 0$ population to the fast-decaying $2P_{1/2}$ state. The remaining $F = 1$ atoms are then detected on a channel-electron multiplier and used as our signal. Measurements are taken at a variety of transition frequencies to plot lineshapes and to extract the line center. Ramsey spectroscopy produces lines which are shaped as $A\text{sinc}^2(Bf)$ functions (A being the amplitude, f the frequency, and B being a scale factor), allowing the line fits near the center frequency to be fit with high fidelity. Following is a more detailed description of the experimental setup and procedure.

To measure $2S_{1/2}^{\text{hfs}}$, we first prepare metastable hydrogen in the $F = 0, m_F = 0$ magnetic sublevel using the method shown in Fig. 2.2. Molecular hydrogen is first disassociated in a microwave discharge cell with approximately 1 Torr of hydrogen and 40 W of microwave power operating at 2.45 GHz. The atoms then travel into a bent nozzle contacting a cryogenic cold head. Through collisions with the cold nozzle, atoms exit as a cold, diffusive beam. By adjusting the temperature of the nozzle in the range of 300 K to 5 K, atomic beam's Maxwell-Boltzmann velocity peaks are moved between 400 and 3000 m/s. The atoms then enter a state preparation chamber that contains a cavity-enhanced 243 nm radiation (the subject Section 2.6). This radiation beam is angled by about 6° to the flow direction of hydrogen in order to lengthen the interaction time, compared to a perpendicular crossing. Two-photon excitation excites some ground-state hydrogen to the metastable state, and due to the fine frequency control of our radiation, we can selective excite

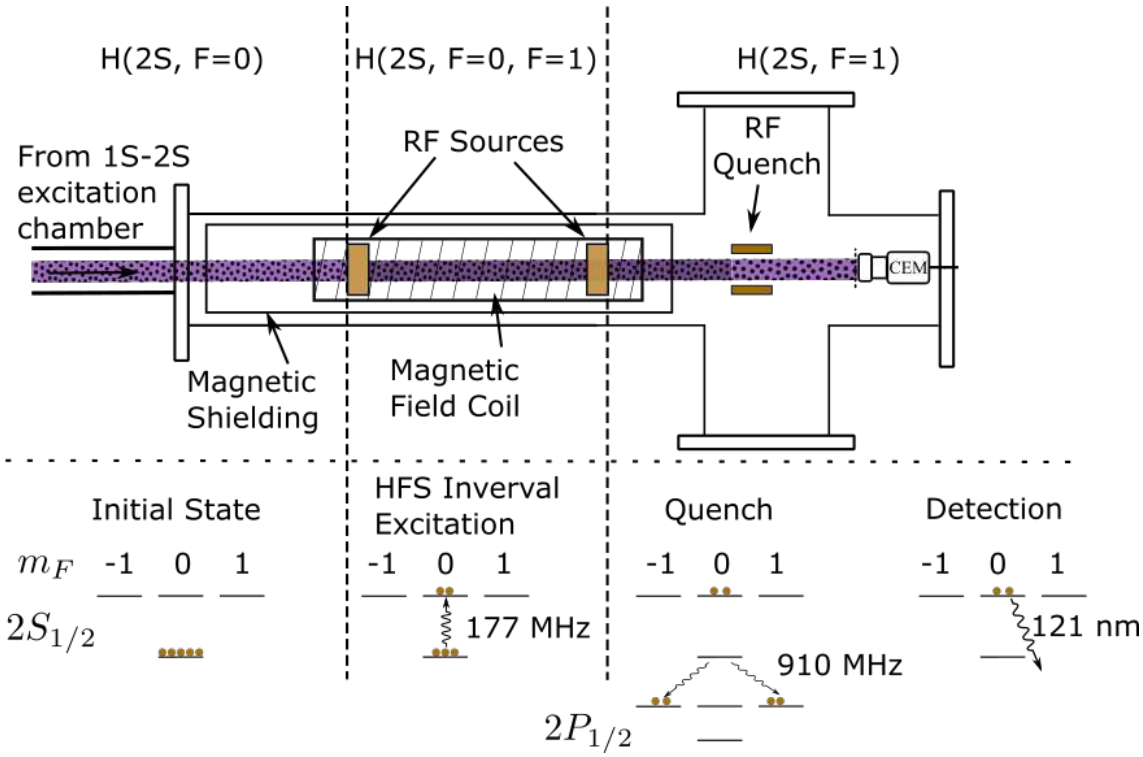

Figure 2.3: RF spectroscopy region. Metastable hydrogen in the $F = 0$ state travel through two RF coils, separated by 30 cm. The RF sources at 177 MHz drive a large percentage of the population to the $F = 1$ state. A second RF transition at 909 MHz will quench the remaining population from $F = 0$ to the $2P_{1/2}$ state, which decays quickly to the ground state. Metastable atoms which made the transition to $F = 1$ are then detected using a channel-electron-multiplier by quenching the remaining metastable atoms to the ground state and detecting 121 nm radiation.

only the $F = 0, m_F = 0$ state. On a typical day, we seed the buildup cavity with $\sim$100 mW of 243 nm power.

After metastable excitation, the atoms exit the preparation chamber and enter a magnetically shielded interaction region in a separate chamber, shown in Fig. 2.3. Some percentage of atoms are excited to the $2S_{1/2}$, $F = 1, m_F = 0$ state using two separated oscillatory RF fields at approximately 177 MHz. The remaining $F = 0$ atoms are then driven to the $2P_{1/2}$ state with a 910 MHz RF field and quickly (1.6 ns) decay to the ground state. The metastable atoms which made the hyperfine transition to the $F = 1$ state are then detected on a channel-electron-multiplier. The atomic lineshape is measured by sweeping the RF frequency near the resonance. Determining the line-center involves averaging many individual scans and fitting simplified models to the central peak of the Ramsey fringe pattern.

In the following sections, details of the theoretical model, experimental design, and the radiation sources are presented. Progress in determining the robustness and repeatability of the hyperfine measurement is discussed, as well as an outlook for the next steps and future of this experiment.

2.4 Theoretical Model

To build a simple theoretical model of the expected lineshape of the hyperfine transition, we can assume a two-state system with a Rabi rate Ω (defined in our specific case in the following section) between ground c_g and excited c_e states. Applying the rotating wave approximation and transforming to the rotating frame, Schrodinger's equation produces population dynamics given by

$$i\dot{c}_g = -\frac{\Omega}{2}c_e \tag{2.4}$$

$$i\dot{c}_e = -\frac{\Omega}{2}c_g + \Delta c_e, \tag{2.5}$$

where Δ is the detuning frequency between the atomic and microwave coil resonance. This set of equations can be solved by taking the derivative of the top equation, solving for $\dot{c}_e$ and inserting the result into the bottom equation. This results in a second-order differential equation in c_g:

$$\ddot{c}_g + i\Delta\dot{c}_g + \frac{\Omega^2}{4}c_g = 0. \tag{2.6}$$

The general form for the solution of this equation is $c_g = c_1 e^{r_1 t} + c_2 e^{r_2 t}$, where $r_{1,2}$ are the roots of the characteristic equation and coefficients $c_{1,2}$ can be found after initial conditions are applied. After inserting the roots $r_{1,2} = -i\Delta/2 \pm i\bar{\Omega}/2$, where $\bar{\Omega} = \sqrt{\Omega^2 + \Delta^2}$, into the general equation, we can solve for the population coefficients to get

$$c_g(t) = e^{-i\Delta t/2}(c_1 e^{i\bar{\Omega}t/2} + c_2 e^{-i\bar{\Omega}t/2}) \tag{2.7}$$

$$c_e(t) = -\frac{1}{\Omega^*} e^{-i\Delta t/2}(c_1 e^{i\bar{\Omega}t/2}(\Delta - \bar{\Omega}) + c_2 e^{-i\bar{\Omega}t/2}(\Delta + \bar{\Omega})). \tag{2.8}$$

Now we can solve for the unknown coefficients $c_{1,2}$ in terms of population coefficients by considering the set of equations at $t = 0$. The result for these coefficients is

$$c_1 = c_g(0)\left(\frac{\bar{\Omega} + \Delta}{2\bar{\Omega}}\right) - c_e(0)\frac{\Omega^*}{2\bar{\Omega}} \tag{2.9}$$

$$c_2 = c_g(0)\left(\frac{\bar{\Omega} - \Delta}{2\bar{\Omega}}\right) + c_e(0)\frac{\Omega^*}{2\bar{\Omega}}. \tag{2.10}$$

Inserting these values back into our general solution and simplifying, we get

$$c_g(t) = e^{-i\Delta t/2}\left[c_g(0)\left(\cos\bar{\Omega}t/2 + i\frac{\Delta}{\bar{\Omega}}\sin\bar{\Omega}t/2\right) + c_e(0)i\frac{\Omega^*}{\bar{\Omega}}\sin\bar{\Omega}t/2\right] \tag{2.11}$$

$$c_e(t) = e^{-i\Delta t/2}\left[c_e(0)\left(\cos\bar{\Omega}t/2 - i\frac{\Delta}{\bar{\Omega}}\sin\bar{\Omega}t/2\right) + c_g(0)i\frac{\Omega}{\bar{\Omega}}\sin\bar{\Omega}t/2\right] \tag{2.12}$$

This set of equations describes the amplitudes of both ground and excited states after some amount of time t. The next steps in the analysis involve solving for the amplitudes after an amount of time τ of interaction with a constant strength RF field, followed by a dead time T of zero applied RF field, and finally another time τ of applying the RF field. After the first interaction time τ and the dead time T, Eqns. 2.11 and 2.12 simplify to

$$c_g(\tau + T) = e^{-i\Delta T/2}\left[c_g(\tau)(\cos\Delta T/2 + i\sin\Delta T/2)\right] \tag{2.13}$$

$$c_e(\tau + T) = e^{-i\Delta T/2}\left[c_e(\tau)(\cos\Delta T/2 - i\sin\Delta T/2)\right] \tag{2.14}$$

We can easily see that these expressions simplify down to

$$c_g(\tau + T) = c_g(\tau) \tag{2.15}$$

$$c_e(\tau + T) = e^{-i\Delta T} c_e(\tau) \tag{2.16}$$

This last pair of relations lets us write down amplitudes for the final coefficients after $2\tau + T$.

$$c_g(2\tau + T) = e^{-i\Delta T/2}\left[c_g(\tau)\left(\cos\bar{\Omega}\tau/2 + i\frac{\Delta}{\bar{\Omega}}\sin\bar{\Omega}\tau/2\right) + c_e(\tau)e^{-i\Delta T} i\frac{\Omega^*}{\bar{\Omega}}\sin\bar{\Omega}\tau/2\right] \tag{2.17}$$

$$c_e(2\tau + T) = e^{-i\Delta T/2}\left[c_e(\tau)e^{i\Delta T}\left(\cos\bar{\Omega}\tau/2 - i\frac{\Delta}{\bar{\Omega}}\sin\bar{\Omega}\tau/2\right) + c_g(\tau) i\frac{\Omega}{\bar{\Omega}}\sin\bar{\Omega}\tau/2\right] \tag{2.18}$$

Now we only need to solve for the amplitudes at time τ. Using initial conditions of $c_g(0) = 1$ and $c_e(0) = 0$, we get the result for the excited state population coefficient being

$$c_e(2\tau + T) = e^{-i\Delta T}\left[i\frac{\Omega}{\bar{\Omega}}\sin\bar{\Omega}\tau/2\cos\bar{\Omega}\tau/2(e^{-i\Delta T} + 1) + \frac{\Delta\Omega}{\bar{\Omega}^2}\sin^2\bar{\Omega}\tau/2(e^{-i\Delta T} - 1)\right]. \tag{2.19}$$

Multiplying this term by it's complex conjugate, using some trig identities and simplifying gives our final result for the population in the excited state:

$$|c_e(2\tau + T)|^2 = \left(\frac{\Omega}{\bar{\Omega}}\sin\bar{\Omega}\tau\cos\frac{\bar{\Delta T}}{2} - 2\frac{\Omega\Delta}{\bar{\Omega}^2}\sin^2\frac{\bar{\Omega}\tau}{2}\sin\frac{\bar{\Delta T}}{2}\right)^2, \tag{2.20}$$

where the term $\bar{\Delta T} = \Delta T + \phi_1 - \phi_2$ holds all of the phase difference information about the fields in first and second oscillatory field regions.

2.4.1 Magnetic Rabi Rate

To accurately compare theory results to experiment, we need to determine the Rabi rate for a magnetic transition in terms of experimental parameters. The Rabi rate is given by

$$\Omega = \frac{g_J \mu_0 \mu_B}{\hbar} \langle F, m_F | J | F+1, m_F \rangle \, H. \tag{2.21}$$

The constants in this expression are tabulated below in Table 2.1.

Table 2.1: Definition of terms used in calculating the magnetic Rabi rate.

Lande g-factor	g_J	2 [dimensionless]
Vacuum permeability	μ_0	$4\ \pi \times 10^{-7} N/A^2$
Bohr magneton	μ_B	9.274×10^{-24} J/T
Magnetic field strength	H	[A/m]
Reduced Planck's constant	$\hbar$	$1.055 \times 10^{-34} J \cdot s$
Matrix element	$\langle F, m_F \vert J \vert F+1, m_F \rangle$	1/2 [dimensionless]

Multiplying all of the constants together, we get that the Rabi rate is proportional to the magnetic field strength, $\Omega = 1.105 \times 10^5 H[\frac{m}{A \cdot s}]$. To convert to units of magnetic flux, we assume $H \approx B/\mu_0$ for copper, since this is the material used to make the RF coils. This gives us $\Omega = 8.79 \times 10^{10} B[T \cdot s]^{-1}$. Multiplying by 10^{-4} to consider the magnetic field in Gauss instead of Telsa gives us $\Omega = 8.79 \times 10^6$ B $[G \cdot s]^{-1}$ for the final Rabi rate.

2.5 Experimental Design

An overview of the experimental design is shown in Fig. 2.2 and Fig. 2.3 and briefly discussed in Section 2.3. In this section, more details are discussed of the apparatus along with some of the systematic effects which drove design decisions.

2.5.1 Atomic Beam

The atomic hydrogen beam is generated by flowing hydrogen through a microwave discharge tube as described in [22], closely following the design of Walraven [23]. Hydrogen gas, H_2, flows through an hourglass-shaped quartz tube with a 500 μm diameter orifice at its center. The molecular hydrogen pressure on the H_2 side is maintained between 700-800 mTorr, while the chamber pressure on the atomic side is around $10^{-7} - 10^{-8}$ Torr. An Evenson-design cavity

(Opthos Instrument Company) encompasses the discharge tube and is supplied with a 2.45 GHz microwave signal with 40-45 W of power. A high voltage, high frequency generator (Electro Technic Products) is used to spark the discharge.

Following the quartz discharge tube, the atoms flow through teflon tubing into a chamber, held at about 10^{-7} Torr. The atoms are sent into a bent nozzle design which, unlike straight nozzles, forces contact with the nozzle and leads to a lower average thermal distribution. Both aluminum and copper nozzles were tested in the design phase, and aluminum seems to allows less recombination on its surface. The nozzle is mounted to a cryogenic cold head and surrounded by a cylindrical heat shield. Nozzle temperatures between 4.5 K and 300 K are achievable and through time-of-flight tests using a residual gas analyzer, we have shown the atomic beam efficiently thermalizes to the nozzle temperature [22]. Furthermore, atoms produced and cooled in this way are strictly in the ground state since nozzle collisions will quench any atoms excited during the disassociation process.

2.5.2 RF Coils

In order to drive the hyperfine transition, approximately 177 MHz radiation is required. Because the orbital angular momentum for this transition is not changing ($\Delta l = 0$), a simple electric dipole transition is not possible, and instead we must use the magnetic moment interaction. Several designs for such a transition exist. For example, Herberle *et. al.* in the first measurement of the $2S_{1/2}$ hyperfine transition designed a rectangular box with a sheet of current flowing down its center [19], while Rothery *et. al.* used a 1 meter-long transmission line consisting of a grounded rectangular waveguide and copper rod as an inner conducting core [20]. Our approach was aimed at generating a compact, uniform magnetic field along the direction of atomic flow, so we opted for a current loop design, as shown in Fig. 2.4.

Our RF coil design consists of 2 cm long copper ring with a 1.5 inch inner diameter. The two coils are separated by 26 cm to give a total interaction length of 30 cm. For impedance matching and setting the resonant circuit frequency, a 50 Ω resistor and variable 1-10 pF capacitors are placed

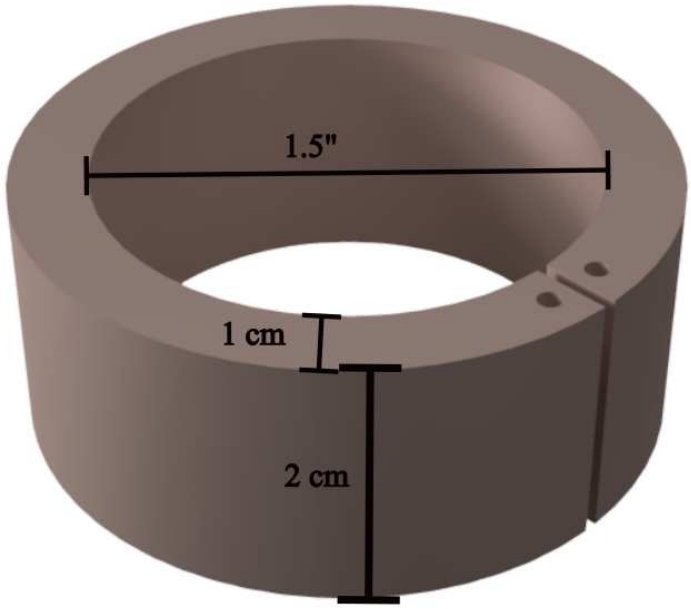

Figure 2.4: The general design of the RF loops used to drive the magnetic hyperfine transition. The loops are made from copper and each one contains a 50 Ω resistor and variable capacitor in series in order to resonantly drive the coil. The inner diameter is 1.5 inches and the width is 2 cm long.

in series with the loops. The variable capacitor is tuned while monitoring the circuit resonance using a Real-Time Spectrum Analyzer. Each of the coils is controlled on a different output channel of an arbitrary waveform generator (Rigol 4202) and connected with coaxial cables.

2.5.3 Magnetic Shielding

In low magnetic fields, the $F = 0, m_F = 0$ state and the $F = 1, m_F = 0$ state do not have a linear component to their Zeeman shifted energy (for example, see Section 3.3.1 for Zeeman energy shift calculations). However, the $2S_{1/2}$ hyperfine splitting is Zeeman shifted at a quadratic rate of 22.184 kHz/G^2. Because of this, Earth's magnetic field would shift the line on the order of 5 kHz if left unaddressed. While active field cancellation using Helmholtz coils and various

Figure 2.5: Magnetic shield used to mitigate Earth's magnetic field. The outermost length is 485 mm, the innermost is 400 mm. The inner cylinder diameter is 8 cm with a 5 mm gap between layers. Thru holes were made to allow electronic connections to the RF loops.

orthogonal shim solenoids is a commonly used technique to reduce Earth's field, we instead shield the magnetic field using mu-metal. Mu-metal is a nickle and iron alloy with a high relative permeability. This high permeability causes magnetic field lines to divert their path through the material, leading to a magnetic field shield when the material is wrapped around an interaction region.

To achieve our initial goal of measuring the hyperfine transition at the 1 Hz level, we need to ensure stray magnetic fields are reduced as far as possible; a field strength of 5 mG, for example, would shift the line by only 0.5 Hz, which would make for a reasonable correction, but reducing the field to 2 mG shifts the line by only 100 mHz, which is negligible in this measurement. To determine the efficacy of the mu-metal shield across the entire interaction region, we used a boundary integral methods software package created by the Insertions Devices Group at the European Synchrotron Radiation Facility called Radia [24]. This software subdivides volumes of a given material and through iterative steps applies several neighbor interactions through a relaxation process in order to compute the net field surrounding an object.

For our initial experiment, we planned a 30 cm interaction region. To ensure the entire interaction region has a low field, we created a 48.5 cm long cylinder, since there is some level of fringing field that enters the shields at the ends. Three layers of shielding is necessary to guarantee the

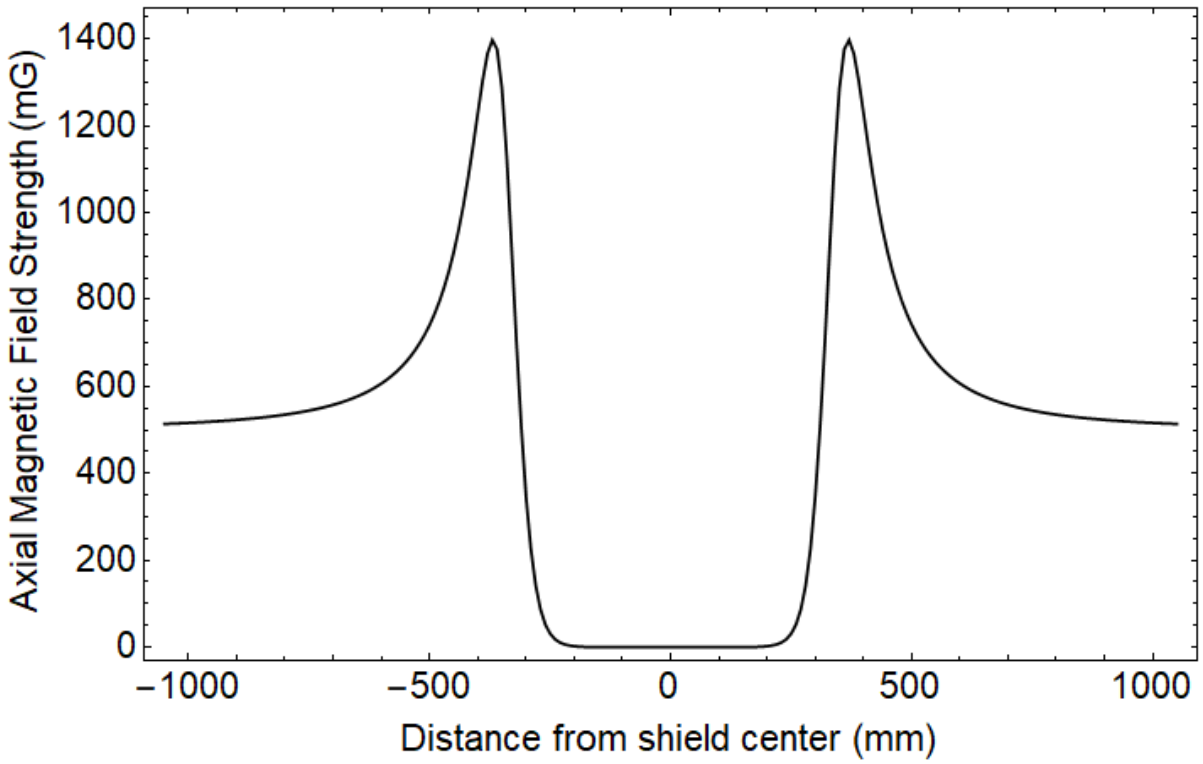

Figure 2.6: Effect of magnetic shielding on-axis through the center of the triple-layer mu-metal shield. In this Radia simulation, a uniform field strength of 500 mG along the axis of the shield is assumed. The presence of the shield causes the field lines to bunch at the shield boundary, but rapidly diminish inside of the concentric cylinders. Within the interaction region ($\pm$ 150 mm), the maximum field strength is reduced to 10 mG with a mean value of only 2 mG.

field is low across the 30 cm central region, with subsequent layers receding inwards and becoming shorter. A schematic of the shields is shown in Fig. 2.5. Thru holes were inserted for both mounting and for electric feedthroughs, but these are small enough to have negligible effect on the shielding efficiency.

Figure 2.6 shows the magnitude of field along the $z-$direction down the magnetic shields. The initial assumed magnitude of Earth's field is 500 mG in these simulations, and the average size of the field is only calculated to be 2 mG within the interaction length. Such a field size shifts the hyperfine line center by around 100 mHz. Electronic feedthroughs were drilled into the shielding, but the size of the holes are small enough as to not interfere with the shielding performance. The z-axis within the text is described as being transverse through the center of this shield.

2.5.4 RF Quench

Before the metastable hydrogen beam is detected, the $F = 0$ atoms have to be quenched to the ground state. This has been accomplished in a variety of ways: an RF driven stub, parallel plates in the vertical plane, and parallel grids along the z-axis. Each method was capable of driving the 909 MHz transition between the $2S_{1/2}$ and $2P_{1/2}$ state to quench the majority of $F = 0$ atoms. Although, due to leakage fields affecting atoms within the interaction region, the vertical parallel plates were implemented in the final apparatus. Note, however, that all of the data presented later in this chapter used the stub design. This quench region mounts directly onto a support tube holding the Ramsey RF loops and the CEM mounts directly onto the back of this part. A coaxial cable drives a small wire stub that protrudes into the atomic beam path, while the rest of the casing is held at ground.

2.5.5 Metastable Detector

To detect metastable hydrogen atoms, the beam flows into a channel electron multiplier (CEM). Excited atoms enter the CEM, mix with the $2P_{1/2}$ state due to a strong electric field and decay to the ground state, emitting a Lyman-α photon, which hits the CEM walls. Electrons are ejected and a 2.8 kV voltage across the CEM causes an electron cascade which leads to an approximately 100 mV pulse taken as the signal output. Pulsed signals are amplified, filtered, and then sent to a frequency counter (Hewlett-Packard 53131A) and integrated. In some experiments within our lab, a rejection grid has also been attached to the CEM. This grid helps to eliminate background counts caused by scattered 243 nm radiation striking the graphite coated walls, which eject electrons. These electrons make their way to the CEM, resulting in a large background on the counter. However, the hyperfine experiment is placed in a chamber much further away than where other experiments have been performed and the rejection grid is not needed.

2.6 UV Radiation Source

One of the primary advantages of performing the $2S_{1/2}$ hyperfine experiment using RF Ramsey spectroscopy is our method of generating the initial metastable beam. While the earlier RF experiments used electron bombardment to excite hydrogen to the metastable state, we have developed a high-power UV radiation system at 243 nm in order to drive two-photon excitation from the ground state. Fine frequency control of this system allows us to strictly populate either the singlet $F = 0$ or triplet $F = 1$ state. Other experiments in the lab have utilized the triplet state (the $2S_{1/2} \rightarrow 8D_{5/2}$ transition measurement and laser slowing of hydrogen [4]), but for the hyperfine measurement we want the atoms to enter the RF region solely in the singlet state.

In order to effectively populate the metastable state, several watts of power are required to intersect the atomic beam due to the inherently low two-photon transition rate. To this end, the design of such a high power system is as follows: an extended-cavity-diode-laser (ECDL) generates power at 972 nm. That radiation is split between a frequency stabilization path and a power amplification path. The amplification path consists of two amplifiers, a tapered amplifier (TA) and a ytterbium (Yb) fiber amplifier. After amplification, the 972 nm radiation enters a bow-tie cavity with a lithium triborate (LBO) crystal at the focus, acting as a resonant frequency doubler. The frequency doubled light at 486 nm then enters a second resonant doubling stage containing a cesium lithium borate (CLBO) crystal to frequency double to the required 243 nm radiation. The generated 243 nm radiation is then coupled to a buildup cavity to further enhance the power. Each of these stages are discussed in subsequent subsections.

2.6.1 Extended Cavity Diode Laser

The 243 nm radiation system begins with a master oscillator consisting of an extended-cavity diode laser producing infrared radiation at 972 nm. The ECDL, shown schematically in Fig. 2.7 and as a picture in Fig. 2.8, is composed of a single-mode laser diode (QPHOTONICS:QLD980-3000) collimated with an 11 mm aspheric lens and a 1200/mm diffraction grating. The ECDL is arranged in a Littrow configuration which offers the advantage of more power over the more

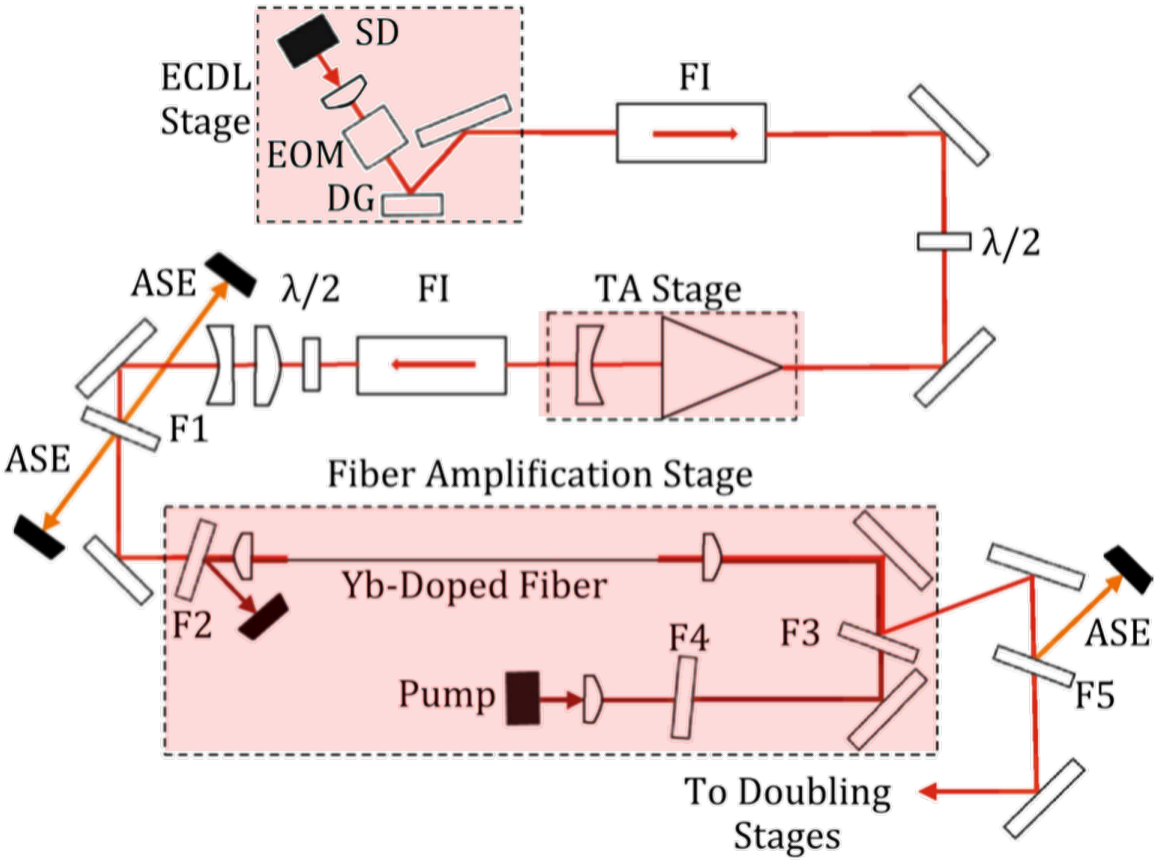

Figure 2.7: 972 nm generation – The three shaded regions show the ECDL, the tapered amplifier, and the fiber amplification stages of the 972 nm radiation system. The ECDL is composed of a seed diode (SD), and electro-optical modulator (EOM), and a diffraction grating (DG). Between the ECDL and TA and between the TA and Fiber amplifier are Faraday isolators (FI) and half waveplates (λ/s). Bandpass filters (F1 and F5), a longpass filter (F2), and shortpass filters (F3 and F4) are used to mitigate ASE and used to separate pump power from 972 nm power.

frequency-tunable Littman-Metcalf configuration. However, large tuning ranges are unnecessary for the application of this laser, so the Littrow is the better option for us. The diode current is controlled with a Thorlabs laser diode driver (LDC205C) while the temperature is controlled using a peltier contacted to the diode mount and driven by a Thorlabs temperature controller (TEC200C). An Analog Devices temperature sensor (AD590) is bored into the diode mount and used with the TEC200C. A diode protection circuit (Thorlabs SR9C-DB9) containing a Zener diode and a Schottky diode are used to prevent voltage spikes from damaging the laser diode.

An electro-optical modulator (EOM) is within the cavity to be used as fast frequency control. Additionally, the diffraction grating is mounted on a translation stage containing a long-throw PZT

for fine control of the cavity length and an ability to correct for slow frequency drifts. The methods and signals used for frequency stabilization are discussed in section 2.6.8.

While the laser diode can operate at a current up to 350 mA and produce 300 mW of power, we have noticed much better mode-hop free stability running it far below the maximum current. A typical current is in the 100-120 mA range, producing between 40-50 mW of 972 power.

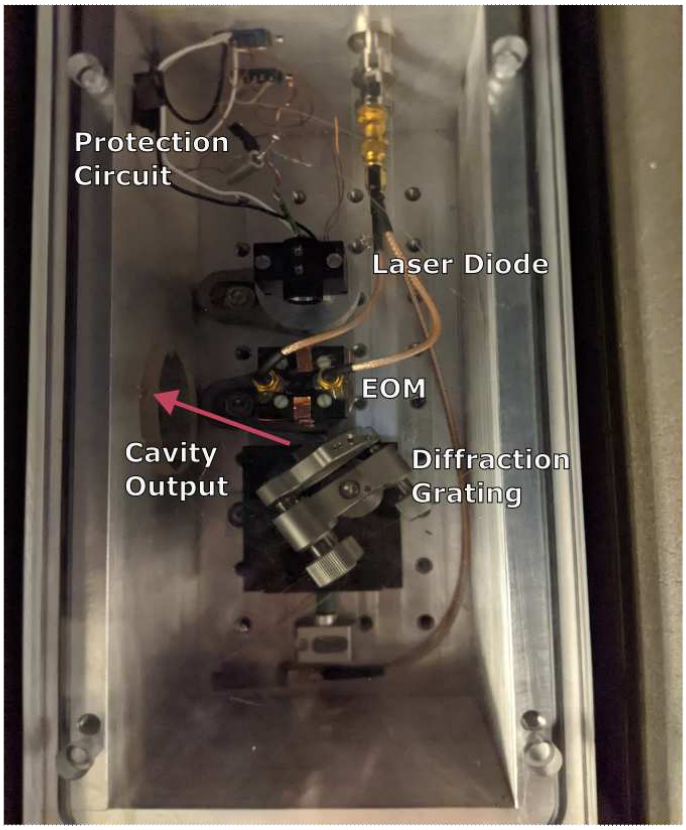

Figure 2.8: Picture of the ECDL. The main components of the ECDL are shown in this image; radiation from the laser diode passes through the EOM and reflects off of the diffraction grating to form a cavity. Each of the feedback controls for frequency stabilization can also be seen here: both sides of the EOM and the translation stage holding the diffraction grating contain error correction signals from the servo loop to maintain a Pound-Drever-Hall (PDH) lock to our prestabilization cavity.

To mitigate vibration instability and to prevent acoustic noise coupling to the ECDL, the cavity is built atop a small optical breadboard, which rests on vibration dampening sorbothane inside of an aluminum box. The aluminum box is placed in a wooden box containing sound-dampening foam. The aluminum box contains a an AR coated window to output the 972 nm power from the cavity and the wooden box has a small hole bored out for the same reason.

Following the output of the ECDL are two optical isolators (Conoptics M714 and Thorlabs IO-5-980-vlp) to prevent any back-reflections from destabilizing the laser diode. Between the isolators is a glass pickoff to split the radiation into the amplification path and the frequency stabilization path. After the isolators is another EOM; this EOM applies 3.6 MHz sidebands to the radiation, which will be useful for locking the frequency doubling cavities downstream. We chose add the sidebands at this point while the power is relatively low to avoid damaging the electro-optical crystal.

2.6.2 Tapered Amplifier

From the ECDL pickoff, 30 mW of 972 nm power is seeded into a tapered amplifier (DILAS TA-0976-3000). The TA is driven by up to 5 A of current using a Wavelength Electronics current controller (PLD10K-CH). To dissipate heat and temperature control the TA, a water-cooled aluminum plate is mounted to the copper housing the amplifier rests in and temperatures are maintained at about 65° F. The alignment of seed power into the TA is extremely sensitive for generating stable ouput. To achieve proper, long-term alignment, a 4.6 mm aspheric lens was mounted to an XYZ translation stage while the seed was injected into the TA. After alignment for maximal power was accomplished, an adhesive (TorrSeal) was used to fix the coupling lens to the TA mounting block and the XYZ stages were removed.

Driving the TA with 5 A and seeding with 30 mW of 972 nm power, an amplification of 3.2 W is achieved. The output beamshape is roughly rectangular with a manufacturer quoting an $M^2 < 1.7$, so beam shaping is required before the next stage of amplification. At the direct output from the TA is a 4.6 mm collimating lens followed by a 100 mm cylindrical lens and a 2x beam reducer

telescope for shaping and sizing the beam. An isolator follows to prevent back reflections from destabilizing the TA. Because the TA chip produces radiation at a band of frequencies, (amplified spontaneous emission [ASE]) and we want to prevent gain from building up in frequencies other than 972 nm in the next amplification stage, a 4nm FWHM band-pass filter angled to work at 972 nm is placed before the fiber amplifier. This ensures that the problematic wavelengths are reduced as much as possible before seeding the Yb fiber, an issue which is discussed in the next subsection. Accounting for all of the losses through the beam shaping optics, we send about 2.5 W of 972 nm power into the next amplifier.

2.6.3 Yb Fiber Amplifier

The Yb fiber amplifier is the primary gain mechanism within this system and was a novel approach to generating high powered UV at the time of building. We use a CorActive (DCF-YB-20/128P-FAC) fiber which has a core diameter of 20 μm, cladding diameter of 128 μm, a coating diameter of 260 μm, and is octagonal in cross-section. These fibers are phosphorous-doped, which prevents a phenomenon known as photodarkening – a process which tends to ionize the Yb atoms over time, which eventually leads to a loss in absorption. As shown in Fig. 2.9, the fiber is placed in a v-groove mount and held in place with stainless steel clamps. Water cooling lines through the baseplate of these mounts allow thermal control and stability while pumping the system. The fiber ends are hand-polished at an 8° angle by successively holding each tip in a ceramic APC ferrule and using Thorlabs diamond and silicon-oxide lapping sheets (LFCF) to slowly grind and polish.

Seed light from the TA is coupled into the Yb fiber using a 10 mm aspheric lens (Thorlabs AL1210B). The lens is mounted into a z-axis translation stage (Thorlabs SM1ZP), which is then mounted with high thermal contact to an aluminum, water-cooled block. The output from the Yb fiber has the same mounting and water-cooling setup. Prior to installing water-cooling lines on the lens system, thermal lensing from the pump radiation led to instability in the amplifier and was a likely cause of fiber becoming damage.

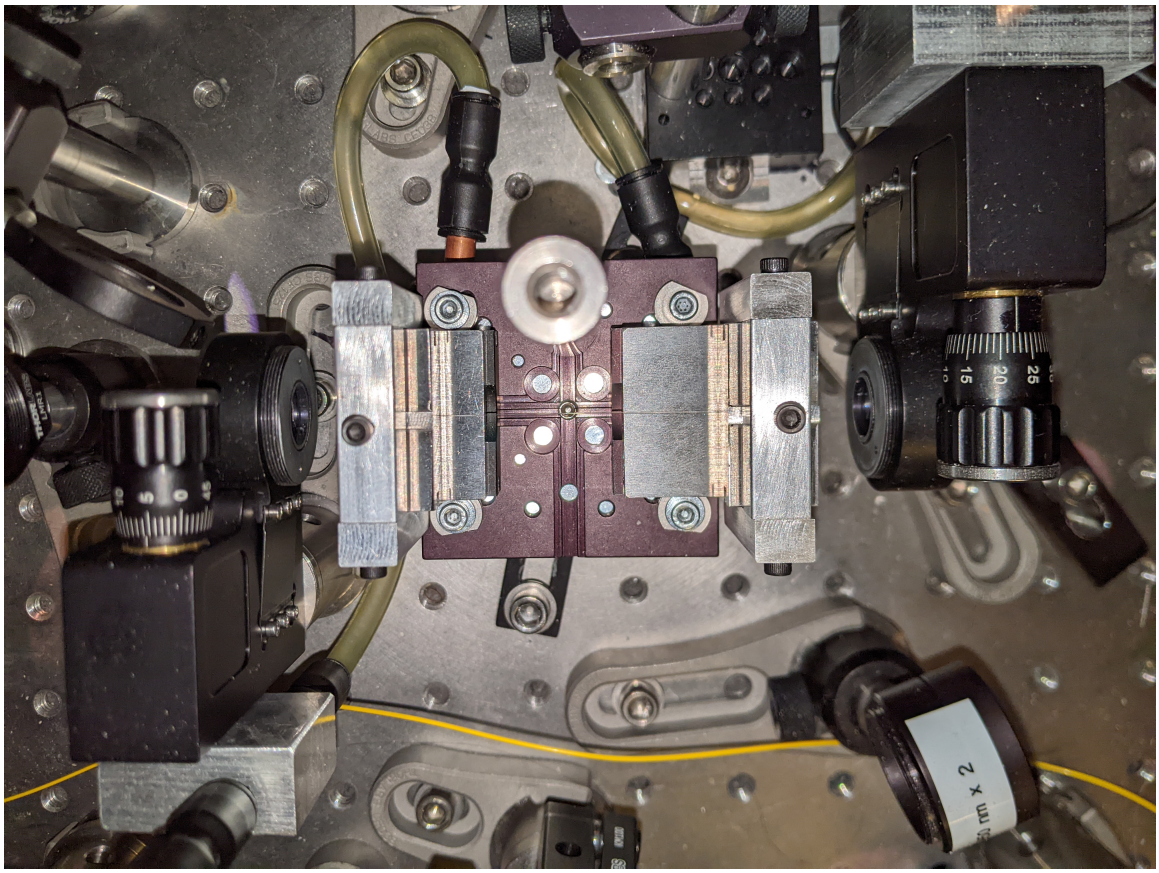

Figure 2.9: Picture of the mounting setup of the Yb-fiber amplifier. This image shows the v-groove mount the fiber is held and clamped in, along with the water cooling lines to maintain a stable temperature while operating the amplifier.

The fiber is pumped by a 155 W fiber-coupled laser diode at 915 nm (nLight e18). While this pump fiber has a nominal wavelength of 915 nm, the actual wavelength varies as a function of current. Measured values for the pump wavelength is shown in Table 2.2. This variation is important in modeling and understanding the amplifier dynamics, as the Yb fiber absorption coefficient shifts by more than a factor of 2 over the range measured.

2.6.4 Yb Amplifier Model

One of the difficulties in developing this amplifier was getting a high population inversion at 972 nm. To achieve this, we need a high pump intensity along the entire length of fiber, leading to a relatively low pump absorption. From the high inversion, however, there is significant gain at both 976 nm and 1030 nm because, as shown in Fig. 2.10, the emission cross sections peak

Table 2.2: Pump power vs. central wavelength data measured at 1.0 A increments. Notably, a peak absorption coefficient occurs at 915 nm within Yb, indicating ideal performance at 10.0 A of pump current.

Current (A)	Pump Power (W)	Central Wavelength (nm)
0.7	0.32	NA
1.0	3.82	903.8
2.0	16.34	904.9
3.0	28.74	905.7
4.0	41.88	906.8
5.0	55.20	907.8
6.0	71.17	909.4
7.0	83.24	910.4
8.0	96.61	912.1
9.0	109.98	913.6
10.0	123.34	915.1
11.0	136.71	917.1
12.0	150.08	919.1

at both of these wavelengths. This gain is problematic in our case due to the resultant amplified spontaneous emission (ASE), which not only propagates back into the laser system, destabilizing it, but also steals potential gain from 972 nm, lowering the net effectiveness of the amplifier.

Several factors affect the amount of ASE produced: fiber length, core and cladding diameters, Yb doping concentration, seed power, and pump power. To combat ASE, an amplifier model was developed to understand and optimize the amount of 972 nm gain produced while mitigating as much ASE as possible. Following the outline given in [25], we can set up a coupled set of differential equations which solves the steady-state case of the population dynamics of the Yb atoms in their excited and ground states. These equations allow the solution of the intensity of the pump beam in both the forwards and backwards directions, as well as the intensity of a set of discrete wavelengths of interest, both in the forwards and backwards directions. In our case, we were supplied with absorption and emission cross sections of 300 wavelengths ranging from 850 nm to 1150 nm, and so adding the pump beam dynamics, our goal is to solve a set of 302 coupled differential equations of the form

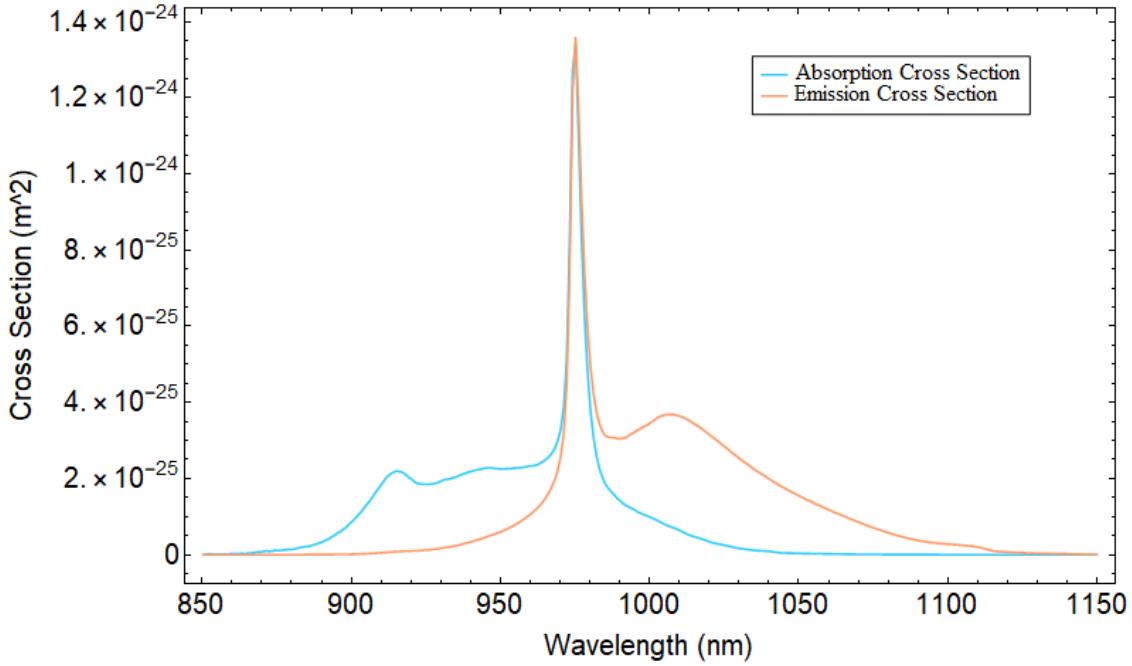

Figure 2.10: Absorption and emission cross sections for Yb fiber. Note the peak emission cross-section is at 976 nm, which leads to problematic ASE. By choosing an appropriate length of gain fiber for our available seed power, based on simulation results, we can mitigate the generated ASE.

$$
\begin{aligned}
N &= N_1 + N_2 \\
N_2 &= \frac{\Gamma_{\text{pump}}\lambda_{\text{pump}}\tau}{hcA}\left[\sigma_a(\lambda_{\text{pump}})N_1 - \sigma_e(\lambda_{\text{pump}})N_2\right]\left(I^+_{\text{pump}} + I^-_{\text{pump}}\right)A_{\text{pumpeff}} + \\
&\quad \sum_i \frac{\Gamma_{\text{s}_i}\lambda_{\text{s}_i}\tau}{hcA}\left[\sigma_a(\lambda_{\text{s}_i})N_1 - \sigma_e(\lambda_{\text{s}_i})N_2\right]\left(I^+_{\text{s}_i} + I^-_{\text{s}_i}\right)A_{\text{eff}} \\
\frac{dI^\pm_{\text{pump}}}{dz} &= \mp\Gamma_{\text{pump}}\left[\sigma_a(\lambda_{\text{pump}})N_1 - \sigma_e(\lambda_{\text{pump}})N_2\right]I^\pm_{\text{pump}} \mp \alpha_{\text{pump}}I^\pm_{\text{pump}} \\
\frac{dI^\pm_{\text{s}_i}}{dz} &= \mp\Gamma_{\text{s}_i}\left[\sigma_a(\lambda_{\text{s}_i})N_1 - \sigma_e(\lambda_{\text{s}_i})N_2\right]I^\pm_{\text{s}_i} \mp \alpha_{\text{s}_i}I^\pm_{\text{s}_i} \pm 2\sigma_e(\lambda_{\text{s}_i})\frac{N_2}{A_{\text{eff}}}\frac{hc^2}{\lambda^3_{\text{s}_i}}\Delta\lambda_{\text{s}}.
\end{aligned}
\tag{2.22}
$$

These equations are taken direction from Eqn. (1) in [25]. For quick reference, definitions for each of the variables are defined in Table 2.3.

In order to solve this set of equations, we need to have a initial conditions for each of the equations. We can measure the seed on the input side of the fiber, as well as the pump on the output side. However, we do not have initial conditions for the backwards propagating ASE/seed,

Table 2.3: Definitions of variables for Eqn. 2.22.

Variable	Definition
N	Yb ion concentration
N_1	population density of Yb ground state
N_2	population density of Yb excited state
Γ	overlap factor between doping area and pump (ASE)
λ	wavelength of pump (ASE)
τ	spontaneous emission lifetime
h	Planck's constant
c	speed of light
A	doped area of the fiber
A_{eff}	effective modal area of ASE
A_{pumpeff}	effective modal area of pump
$\sigma_a(\lambda)$	wavelength-dependent absorption cross-section
$\sigma_e(\lambda)$	wavelength-dependent emission cross-section
$I^{\pm}$	intensity of the forward (+) or backward (-) propagating pump or ASE
α	attenuation factor of the pump (ASE)
$\Delta\lambda_{\text{s}}$	spectral resolution of simulation

nor the forward propagating pump. Because of this, we must use a shooting method to solve for the initial conditions. This involves solving for the forward propagating ASE, then using the reflected power from the tip as initial conditions for the full set of equations. This iterative process is performed until a stable solution is reached for the intensities of all wavelengths.

As an example showing the performance of the model, Fig. 2.11 shows power scaling of 972 nm output with increasing pump power overlaid with the model predictions. This figure shows results from a previously used, smaller pump laser, which could only produce 45 W. Having confidence in the model, though, we were able to optimize fiber length and corresponding Yb doping level to minimize ASE and produce the most 972 nm power as possible. After upgrading our pump laser, we were able to demonstrate power scaling of this amplifier and produce up to 10.8 W of 972 nm radiation with 120 W of pump power.

2.6.5 LBO Doubling Stage

Power from the Yb fiber amplifier is coupled into a resonant, frequency doubling, bow-tie cavity with an LBO crystal at its focus (see Fig. 2.12). This cavity consists of a flat input coupler

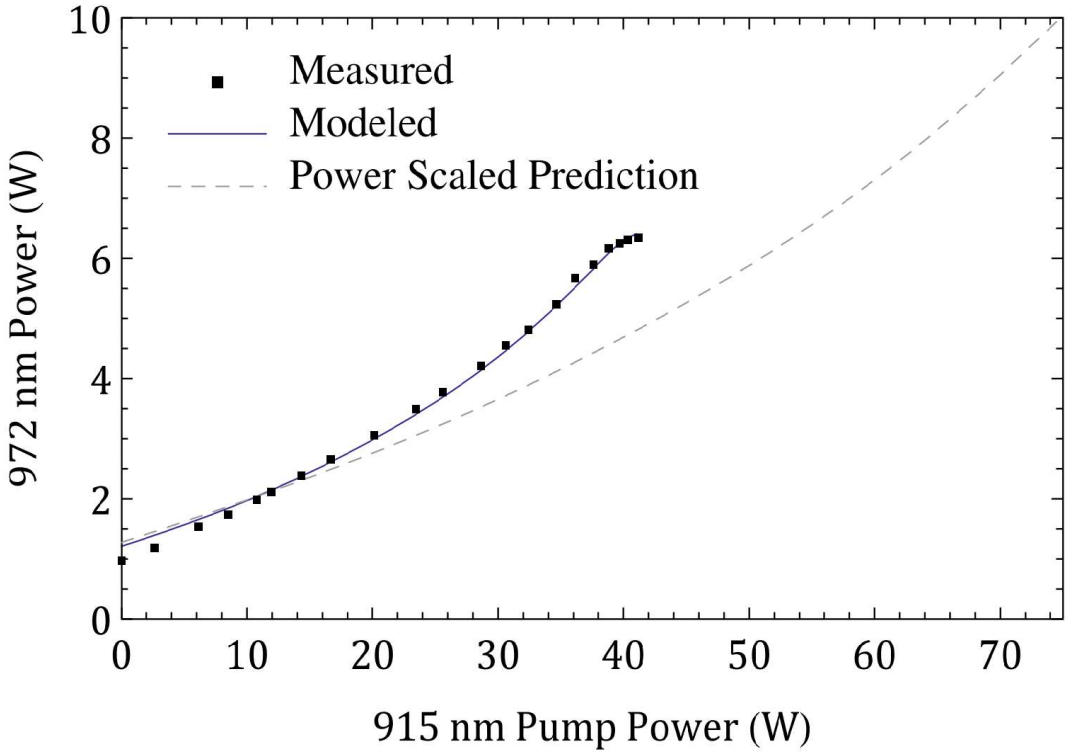

Figure 2.11: Measured data and simulation comparison of Yb fiber amplifier.

with 2 % transmission, followed by a flat high reflector (HR), a 150 mm radius-of-curvature (ROC) mirror, and AR coated, 15 mm LBO crystal, and lastly another 150 mm ROC mirror used as the 486 nm output coupler. Mode matching is accomplished with a single, 1 m focal length lens which focuses seed light into the LBO crystal. To lock the cavity onto the 972 nm resonance, the HR is adhered to a small, fast PZT, while the output coupler is mounted on a single-axis translation stage with a long-throw PZT to allow long term stability. As mentioned in the ECDL section, an EOM applies 10 MHz sidebands to the 972 nm radiation; a small percentage (≈ 0.3 %) of light transmits through the first curved mirror and is detected on a photodiode. An error signal is produced by demodulating the 10 MHz signal through a mixer. This error signal feeds back onto both PZTs through a loops filter and an integrator to maintain a cavity resonance.

Phase matching is performed by adjusting the tip-tilt angle of the LBO crystal. As shown in Fig. 2.13, we are able to convert about 40 % of incident power and have produced up to 4.2 W of 486 nm light.

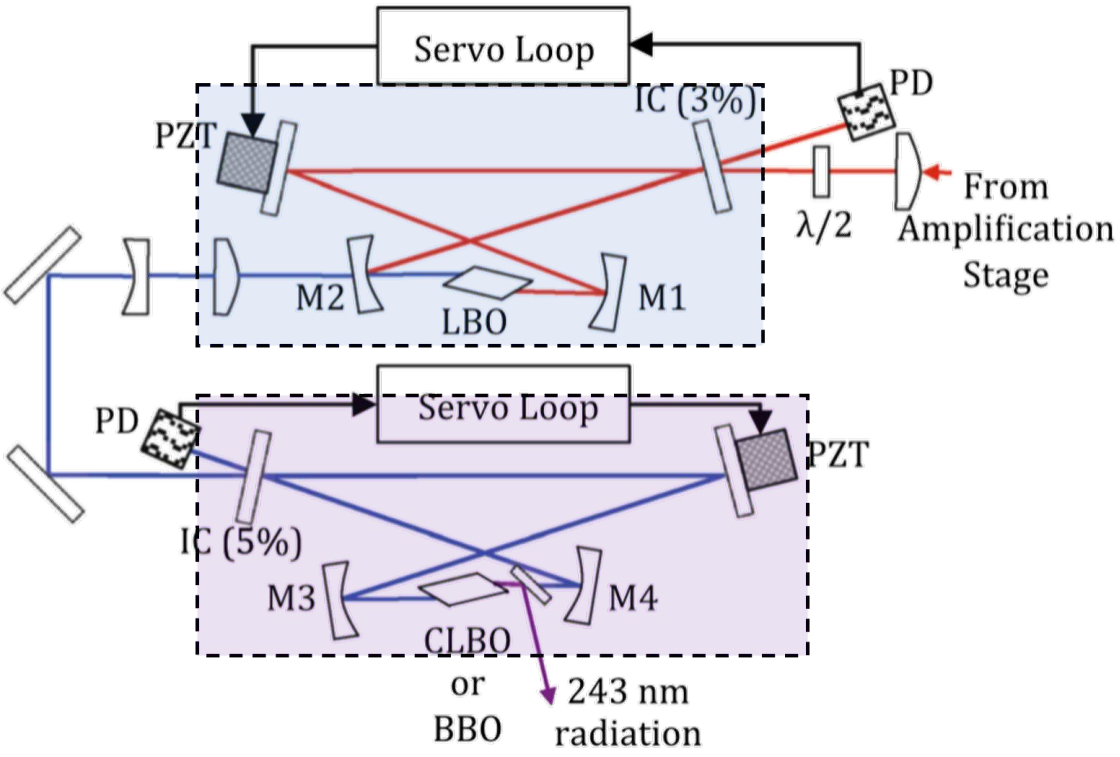

Figure 2.12: Frequency doubling cavities. The top cavity takes 972 nm power from the amplifying stages as an input and frequency doubles the radiation using an LBO crystal into 486 nm power. The 486 nm power is output coupled and seeded into the lower cavity where it is frequency doubled using a CLBO (or BBO) crystal. M1, M2, M3, and M4 are 150 mm radius-of-curvature mirrors.

2.6.6 CLBO Doubling Stage

Due to the spatial walk-off from the LBO cavity, beam shaping of the 486 nm light is required before injecting the second frequency doubling cavity. A pair of cylindrical lenses at 300 mm and -75 mm are oriented to collimate the horizontal axis of the 486 nm beam, then a pair of spherical lenses at 100 mm and -50 mm form a telescope to both reduce the size of the beam and mode match the CLBO cavity. The CLBO cavity is a replica of the LBO cavity in the cavity mirror choices (see Fig. 2.12); two flat mirrors and two 200 ROC mirrors form the ring cavity. A Brewster-cut CLBO crystal mounted in a tip-tilt oven held at 150° C performs frequency doubling, using type I critical phase matching. To output couple 243 nm radiation from the cavity, a Brewster-oriented dichroic mirror with transmission and 243 nm reflectivity is placed after the CLBO and the UV is reflected out of the cavity. An image of the cavity is shown in Fig. 2.16. Due to the high

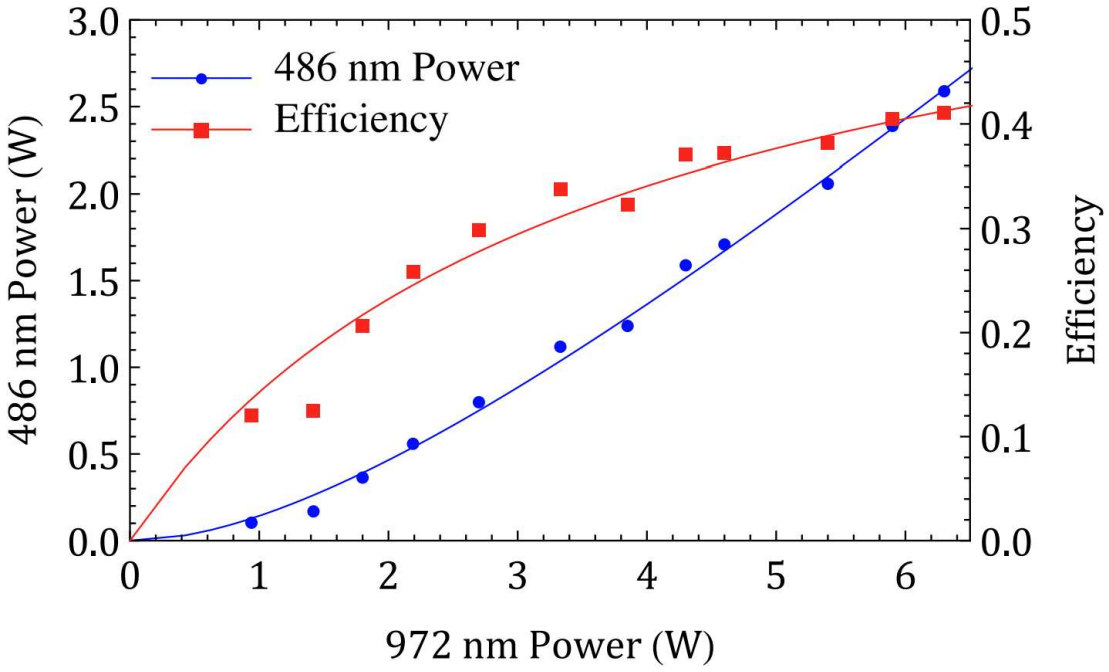

Figure 2.13: Performance of 972 nm to 486 nm conversion within the LBO resonant frequency doubling cavity.

hygroscopy of CLBO, we not only use an oven to maintain a dry crystal environment, but we also continuously purge the oven with nitrogen gas 24 hours a day. With this setup, we have not observed any degradation of frequency conversion performance over a 6 year period of near-daily use, as our conversion factors are still comparable to our 2016 results [26]. As shown in Fig. 2.15, we are able to produce up to 1.4 W of 243 nm power with a seed power of 4.2 W of 486 nm.

2.6.7 Enhancement Cavity

To achieve increased levels of metastable excitation compared to a single reflection two-photon excitation, the 243 nm radiation is built up in an enhancement cavity. The output beam from the CLBO cavity must again be reshaped before the next cavity due to the spatial walk-off deforming the beam's circularity. Two AR coated cylindrical lenses at 150 mm and -25 mm are used on individual translation stages to collimate the horizontal dimension. A pair of spherical lenses with focal lengths 500 mm and 750 mm are used to mode match the enhancement cavity. Two polarizing

beam splitters and a pair of Faraday rotators consisting of permanent magnets and AR coated, fused silica rods, are used as an isolator to prevent back-reflections from destabilizing the CLBO cavity.

The enhancement cavity itself (shown in Fig. 2.2) is composed of an input coupler with ≈ 97 % reflectivity and an output coupler with ≈ 99.7 % reflectivity, both having 1.0 m focal lengths. Each of these mirrors rests in a small housing filled with about 400 mTorr of oxygen gas in order to prevent hydrocarbon contamination degrading the buildup performance, as discussed in [27]. The output coupler is adhered onto a small PZT, which is dithered at about 300 kHz to produce sidebands for locking. This mirror is mounted onto a translation stage containing a long-throw PZT for correcting slow drifts and low frequency noise. An error signal is produced by collecting reflected radiation off of the input coupler and demodulating the signal in a mixer, then using a

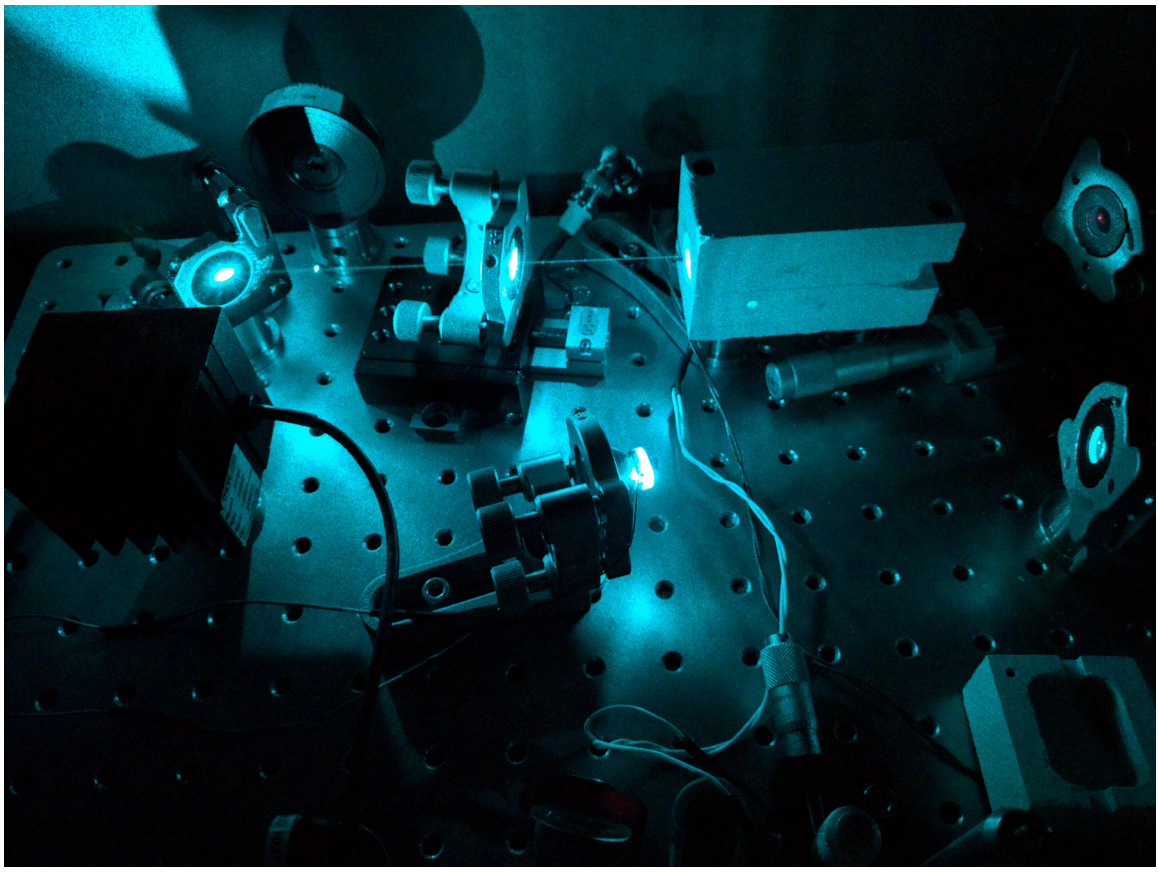

Figure 2.14: Picture of the first resonant frequency doubling cavity. The 486 nm light is shown passing through the output coupler.

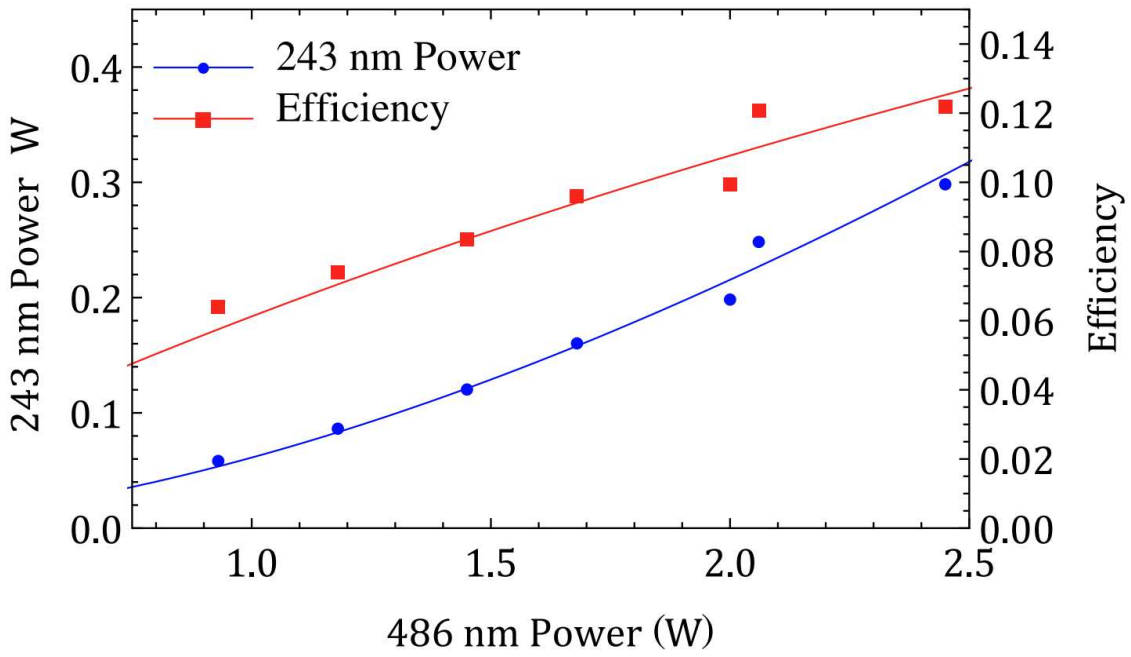

Figure 2.15: Performance of 486 nm to 243 nm conversion within the CLBO resonant frequency doubling cavity.

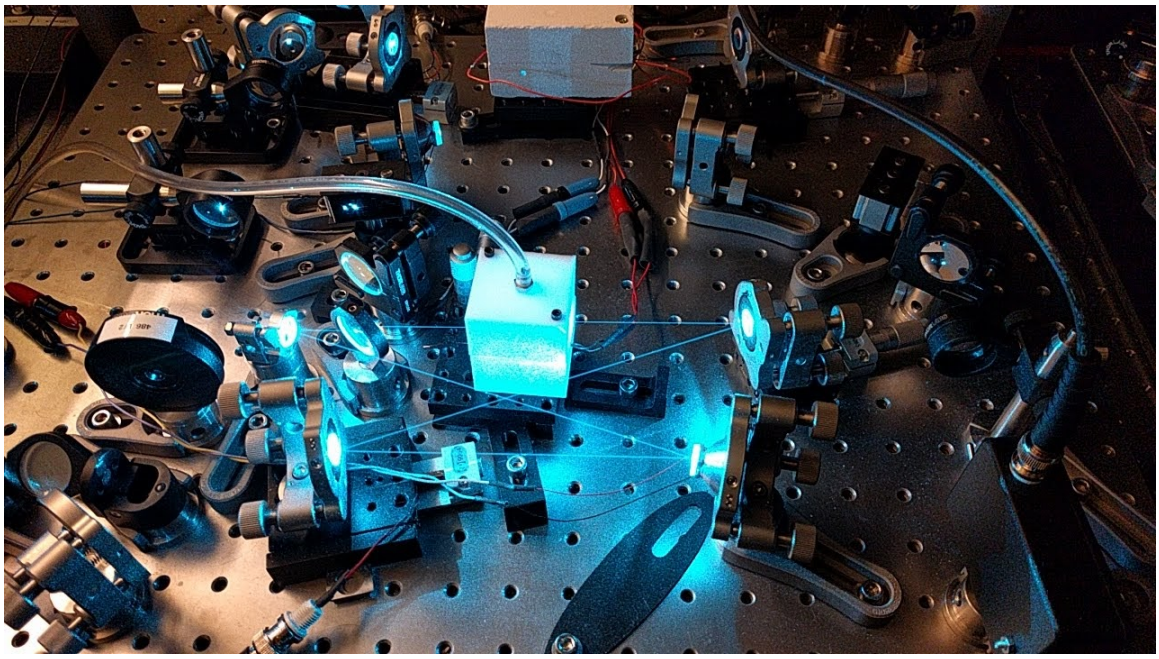

Figure 2.16: A picture of the second resonant frequency doubling.

standard PDH feedback system for the frequency lock. With careful mode matching and alignment, buildup factors of 80 have been observed [28], leading to intracavity powers of about 30 W.

2.6.8 Frequency Stabilization

The frequency stabilization of the system begins at the pickoff from the ECDL between the first two isolators. Of the 40 mW being produced from the ECLD, about 10 mW is split off for the frequency stabilization, allowing 30 mW to seed the TA. The total 10 mW consists of two 5 mW beams; one of these beams is coupled into a fiber to mix the frequency comb light. The other 5 mW is sent through a polarizing beamsplitter and $\lambda/4$ waveplate before being coupled into a standing-wave cavity. This cavity is composed of an input coupler with reflectivity of 99.7% and a high reflector with reflectivity of 99.7%, each with a ROC of 150 mm. The mirrors are attached to a 15 cm long invar tube, which has a very low coefficient of thermal expansion. The HR side contains an annular PZT to adjust the cavity length. The invar cavity sits in a v-grooved aluminum brick with sorbothane supports to dampen vibrational noise. This aluminum brick is housed inside of a wooden box with acoustic-dampening foam-lined walls.

After reflection from the cavity input coupler, the 972 nm beam is sent back through the $\pi/4$ waveplate and reflected off of a polarizing beam splitter (PBS). That radiation is sent to a photodiode, and after demodulating the 10 MHz sidebands through a mixer, an error signal is produced for detecting the cavity resonance. This error signal is sent through a loop filter and feeds back onto the intracavity EOM within the ECDL in order to adjust the laser frequency to match the cavity resonance.

With the ECDL frequency locked to a reference cavity, we then have to lock the laser to our frequency comb [29]. For this, we take the second band of 5 mW power out of the ECDL pickoff and couple into one side of a 50/50 fiber beam splitter. The other input side of the splitter has a narrow band (4 nm FWHM) of 972 nm frequency comb pulses coupled in. Both outputs of the 50/50 splitter are transmitted onto a balanced photodetector to allow the beatnotes between the 972 nm radiation and various comb teeth to be detected. The beatnote and a sine wave from a signal

generator (typically between 3-5 MHz) are transferred into a phase-frequency detector in order to generate an error signal for locking the cavity. This error signal is integrated and sent to the annular PZT on the HR within the reference cavity to complete the frequency stabilization of our system.

By integrating the phase noise of our frequency comb beatnote with the ECDL, the performance of the frequency control and stabilization has been estimated to give <100 Hz linewidths of fundamental frequency. Following frequency quadrupling, the estimated linewidth of the 243 nm radiation is less than 10 kHz. While this level of control is insufficient for attempting an improved $1S - 2S$ spectroscopic measurement, it is well within the transit-time broadened linewidth of the hydrogen atoms and is therefore ample for simply exciting the beam to the metastable state.

2.7 Results and Discussion

The first milestone of this hyperfine experiment was to measure lineshapes and to reliably determine the line center of these lineshapes. While determining the absolute frequency of the transition will take much more time due to characterizing systematic effects and working towards increasing the signal-to-noise, the initial goal to set up the experiment and take the first measurements has been achieved.

2.7.1 Data Acquisition

Lineshapes are generated by setting both RF loop frequencies near the hyperfine resonance, locking the phase between both loops, and then integrating the CEM counts for a set time period, typically 1 s. We perform this 1 s integration over a number of frequencies within a window of interest, randomly selecting frequencies in order to mitigate temporal systematic drifts. During these integration periods, we also collect a voltage signal of the 243 nm radiation from the buildup cavity transmission to normalize our count rate.

Before conducting a scan of the lineshape, we first have to determine the applied voltage to each RF loop which makes a π/2 pulse. Ensuring that each loop individually produces a $\pi/2$ pulse allows for maximum signal for Ramsey spectroscopy. To do this, we measure a baseline number of

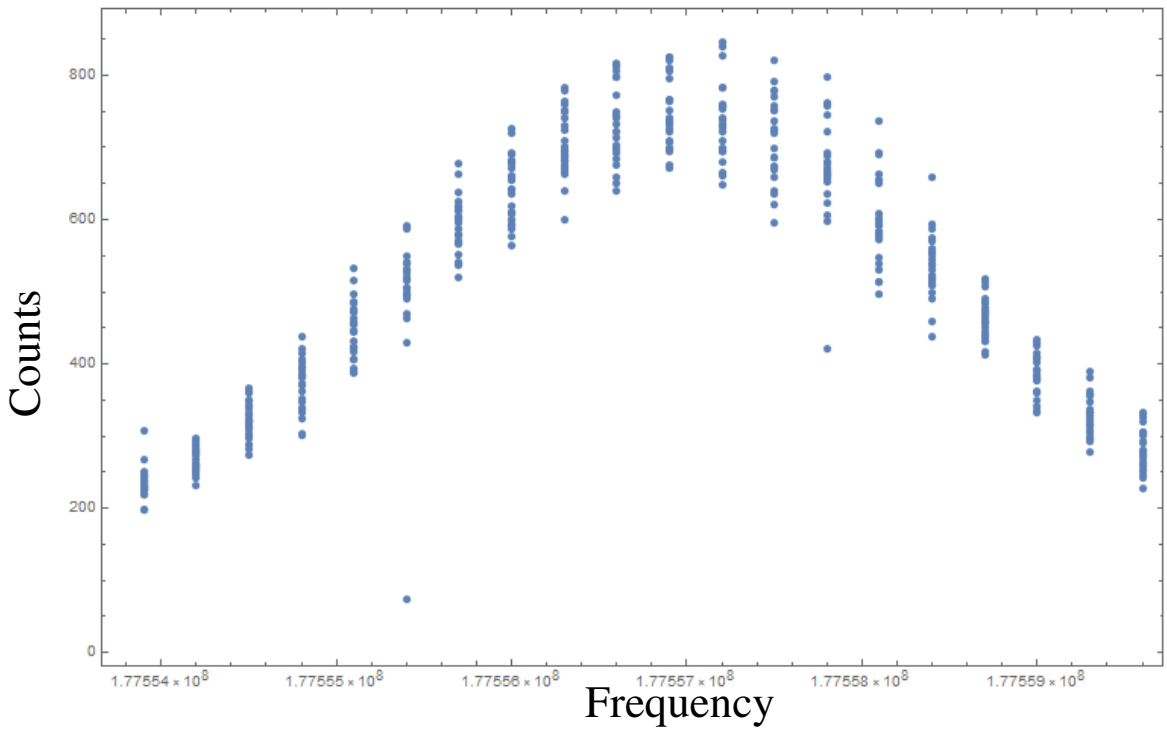

Figure 2.17: Raw data of typical hyperfine data runs. This figure shows a set of about 20 individual lineshape scans of the $2S$ hyperfine interval. There are excess deviations from the mean of each frequency; 243 nm radiation power fluctuations within the enhancement cavity is responsible for most of the additional noise; Fig. 2.18 shows the lineshapes after correcting for this effect.

metastable counts/s without the quench field on. Typical values using a room-temperature nozzle are near 5000 counts/s. Then turning the quench field on, we eliminate about 90% of the count rate. We then drive each RF coil individually on resonance while adjusting the output voltage until we recover half of the lost counts with each coil. This ensures that both RF coils are producing fields such that the atoms receive $\pi/2$ pulses, regardless of small manufacturing differences. This step is taken again with every nozzle temperature since slower-moving atoms will require a smaller magnetic field for a $\pi/2$ pulse.

A typical set of scans is shown in Fig. 2.17. Power fluctuations within the 243 nm buildup cavity add a large variance to the number of detected atoms at each frequency. To mitigate this effect, each 1 s integration value is divided by the root-mean-squared (RMS) value of the 243 nm voltage squared signal over that same period. The result is a nearly shot-noise-limited signal, shown in Fig. 2.18. The central peak of each line scan is then fit with a sinc^2 function to best

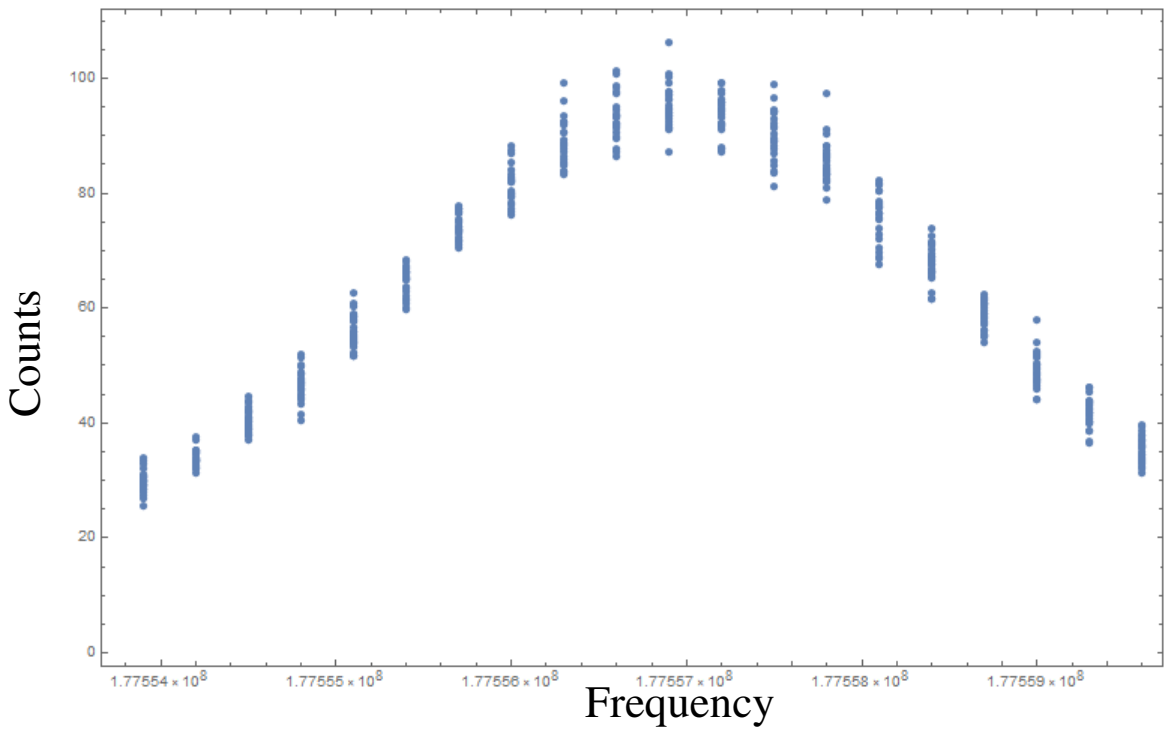

Figure 2.18: Typical hyperfine data runs after normalized by 243 nm power fluctuations. The deviations are nearly shot-noise limited in this case.

determine the line center. Many (10-100) line scans are completed for a given set of run parameters, and each of the line centers is determined, with a corresponding uncertainty based on parameter error analysis. A weighted average and corresponding uncertainty is then calculated. A total integration time of only 10-20 minutes leads to line center uncertainties on the order of 5 Hz.

In order to address effects arising from phase mismatch of the two RF coils, we can perform spectroscopy at several atomic velocities by adjusting our cryogenic nozzle temperature. Since the frequency shift has the form

$$\Delta\nu = \frac{v\delta}{2\pi L}, \tag{2.23}$$

we can determine the relative phase between the coils by fitting a line to several central frequency measurements and make appropriate corrections. Figure 2.19 shows averaged line scans at three different temperatures: 6 K, 100 K, and 300 K. After finding the line centers at each temperature,

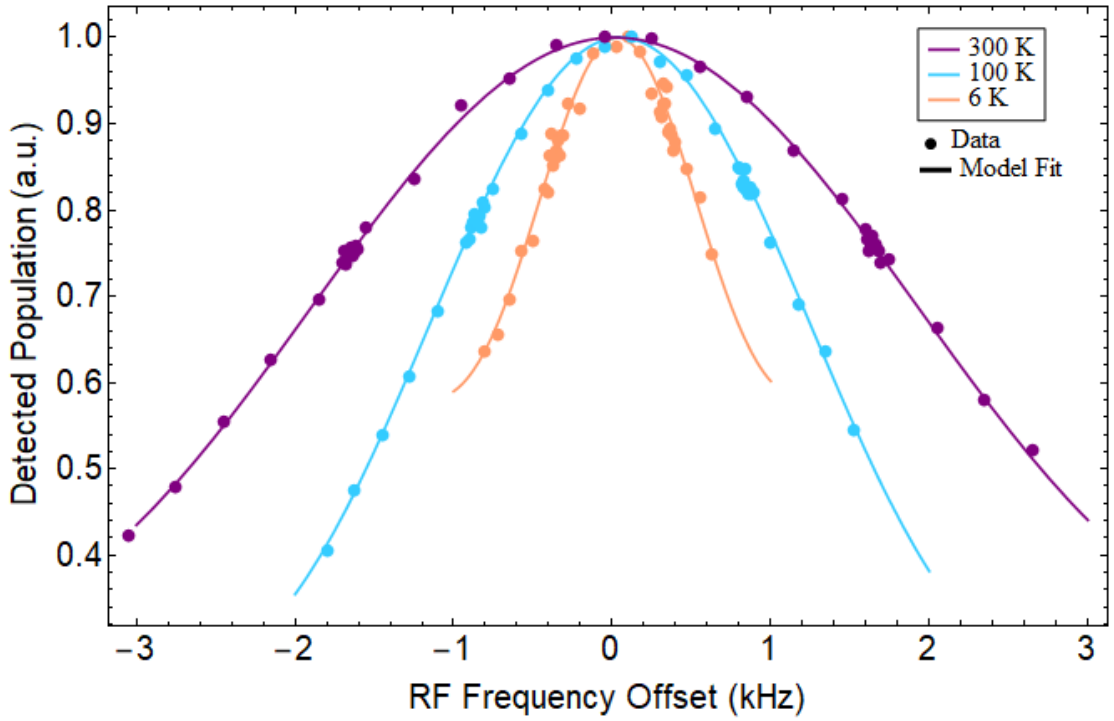

Figure 2.19: Three average line scans at different cryogenic temperatures: 6 K, 100 K, and 300 K. The effect of transit-time broadening is apparent here, as the atoms with lower average velocity results in the narrowest measured linewidth.

the red line in Fig. 2.20 shows an example of atomic velocity vs. frequency shift. The slope of the line gives the relative phase that exists between the two driving RF coils, and after applying that correction and remeasuring at the same temperatures, the line in blue is generated. This demonstrates one of the major benefits to having cryogenic control over the atomic beam velocity.

At the time of writing, we have accomplished the major first steps of this experiment. An apparatus has been designed and built, Ramsey spectroscopy using RF coils has been demonstrated, lineshapes have been measured at several temperatures ranging from 5 K - 300 K, and daily repeatability of the line center determination has been shown. Additionally, mitigation of RF coil phase mismatch has been shown using the atomic mean velocity extrapolation. Signal-to-noise on individual line centers at a given temperature is such that a 5 Hz measurement can be made in approximately 10 minutes of integration. Statistically, we can reach sub-Hertz measurements with only one hour of total integration, which is our next goal.

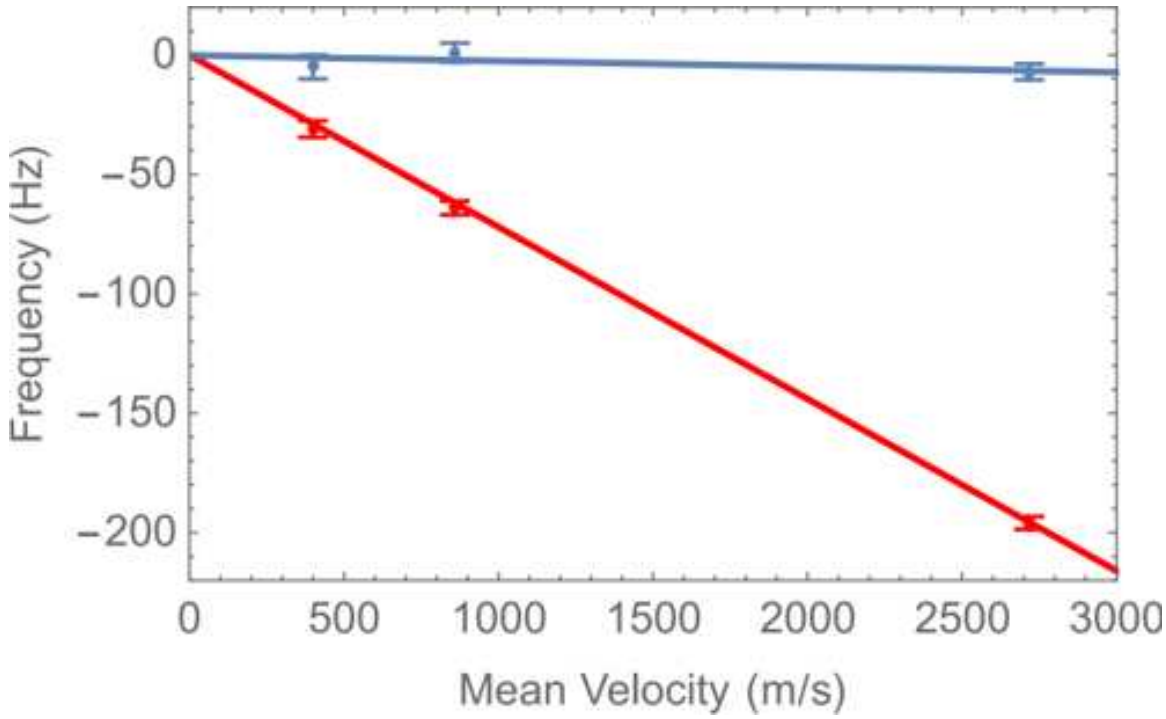

Figure 2.20: Two linear fits of line center measurements taken at 6 K, 100 K, and 300 K. The red line was produced without any relative phase information between the two RF coils. Based on the slope of the red line, a phase adjustment was applied to one RF coil and the blue line was the resultant measurement. This figure highlights the benefit of our ability to generate a cryogenic atomic source, showing effective mitigation of RF phase mismatch.

2.8 Continuing Work

To complete the $2S$ hyperfine measurement, a few systematic characterizations must be performed. Although considerable effort was made to mitigate Earth's magnetic field within the interaction region, imperfect simulations prevent a clear understanding of the extent to which this field has been negated. The stainless steel chamber along with all of the necessary spectroscopy components will affect the field with too complicated conditions to fully model. However, we expect a field no larger than 2 mG, resulting in a shift no larger than about 90 mHz, which is far below our precision goals of 1 Hz. The ± 1 m_F states shift at 1.4 MHz/G, though, and could contaminate the line center measurement. An additional magnetic field along the atomic beam direction will be applied with a solenoid along the length of the interaction region. An applied field of 1 mG will shift these lines by 1.4 kHz and the line center by only 20 mHz; since the linewidth of the hyperfine is on the order of only 1 kHz, the ± 1 states should be far enough detuned not to be present

in the $F = 0, m_F = 0 \rightarrow F = 1, m_F = 0$ line. Several measurements at varying magnetic field strengths will also be conducted so that a true extrapolation to zero transverse field will mitigate any stray field effects. Radial magnetic fields will be suppressed more than transverse with the passive magnetic shield, but a measurement of the magnitude of these fields would be helpful in deciding if further suppression is necessary.

Similarly, stray static electric fields can introduce Stark shifts to the line center. We have used colloidal graphite within our interaction regions in previous experiments [4] and have concluded that we are able to mitigate stray electric fields down to 3 mV/cm using this technique. Assuming a similar level of electric field and using the hyperfine shift rate of -(0.88E$E^2 + 0.23E_z^2$) kHz/(V/cm)^2 [19], we do not expect a shift larger than about 10 mHz, which is also negligible at our precision goal.

Other systematic effects will also be determined and accounted for before a final result can be reported. These include any shift caused by vacuum pressure (shift of 10 Hz/Torr [18] will be negligible), and AC Stark shifts (will perform a power extrapolation, but is expected to be negligible as well).

2.9 Conclusion

Determining the Zemach radius and testing high-orders of QED remains an important task for the field of high-precision measurements. Fundamental constants play an important role in developing our understanding of the natural laws and the ability to probe fundamental physics allows us to confirm hypotheses or make adjustments when observations disagree with current theory. Much progress has been made towards these goals with the design of a spectroscopy chamber, the development of a high-power 243 nm radiation system, frequency stabilization of the fundamental 972 nm source, and cryogenic control of a flowing atomic hydrogen beam.

The last steps for this measurement are laid out and are under way by the next generation of graduate students. A result is expected to follow in the coming months.

Chapter 3

Parity Nonconservation in Hydrogen

3.1 Parity Nonconservation Background

Parity violations can manifest in atomic systems through Z^0 boson exchange between electrons and nucleons in the form of weak neutral current. The strength of parity violating weak interaction can be characterized by dimensionless spin-independent coupling constants C_{1p}, C_{1n} (electron-proton and electron-neutron coupling, respectively) and spin-dependent coupling constants C_{2p} and C_{2n} [30]. These constants relate to the weak couplings of up and down quarks, C_u and C_d, as well as other weak interaction parameters such as the Weinberg Mixing angle, $\sin^2\theta_W$ [31], and the weak charge, Q_W [32]. Due to the nearly inappreciable interaction strength of the weak force, these parameters are extremely difficult to measure in an experimental setting. However, the task of measuring these values remains important for verifying our understanding of the Standard Model (SM) and searching for corrections or extensions to it. To this end, many experiments have been conducted, by means of both scattering and atomic parity violation (APV).

Scattering experiments have been conducted at various high momentum transfer to measure $\sin^2\theta_W$, and in particular to verify the "running" of the mixing angle, meaning that the angle varies with momentum transfer as in Fig. 3.1. The most precise measurements are results from LEP1 and SLAC conducted at the Z-pole, where e^+e^- collisions lead to Z^0 production [33–35]. Unfortunately, the two experiments have a 3.2σ discrepancy that has yet to be resolved, but the commonly used average of these two experiments yields $\sin^2\theta_W(m_Z) = 0.23125(16)$. Lower momentum transfer experiments such as SLAC-E158 have been performed, which was the first to confirm the running of $\sin^2\theta_W$. This was done by e^-e^- (Møller) scattering in which deflection angles were measured for different polarizations of incoming electrons, with results of $\sin^2\theta_W(0.026\text{GeV}^2) = 0.2397(13)$ [36]. Another experiment, based upon neutrino-neutron scattering from the NuTev collaboration, has also yielded a Weinberg mixing angle result. Their analy-

sis involved ratios of charged to neutral current cross sections for both neutrinos and antineutrinos resulted in $\sin^2\theta_W(2.2\text{GeV}^2) = 0.2277(16)$, which is $\approx 3\sigma$ away from the SM prediction [37].

While the collider experiments verified the running of the mixing angle, there remains large uncertainties in measured values and higher precision measurements are required to elucidate any possible physics beyond the SM. APV experiments have the benefit of appearing like atomic spectroscopy experiments, in which precision techniques are now highly developed and uncertainties are well understood. Several elements have been used for recent PNC studies, including bismuth, lead, thallium, cesium, and ytterbium [38–42]. Other experiments are underway utilizing francium [43] and a proposal to use radium ions [44] show potential experimental promise. To date, however, the Boulder Cs experiment remains the most precise APV experiment resulting in the only observation of an anapole moment, as well as a value $\sin^2\theta_W(0.0024\text{GeV}^2) = 0.2261(43)$ [42]. The low momentum transfer of APV experiments makes for an excellent test of the running of the Weinberg angle. Figure 3.1 summarizes the aforementioned experimental results and shows the SM prediction curve. While the current set of experimental results demonstrate a loose agreement with the SM, there are relatively large standard deviations in each, and none lie within the prediction curve. A theory of interest that explains the disagreement is a U(1) gauge symmetry of dark matter that mixes Z and Z_d masses, where Z_d is the so-called "dark Z boson." [45]

The effects of Z_d on parity violating experiments are described in [45] as

$$\Delta\sin^2\theta_W \simeq -0.42\epsilon\delta'\frac{m_Z}{m_{Z_d}} \tag{3.1}$$

where experimental bounds place $|\epsilon\delta'| \lesssim 0.0008$. These effects are shown in Figure 3.1, using assumed masses of 15 GeV and 25 GeV for m_{Z_d}, which are within the range of Z_d candidates from the ATLAS 8 TeV experiment [46]. Measuring a shift in the proposed SM prediction with little uncertainty could be the first step to an indirect measurement of dark matter. An indirect measurement of Z_d would be a monumental discovery which would revolutionize the field of particle physics as well as provide a firm picture of how the dark sector couples to our universe. However, we see relatively large errors in the best APV experiment to date. Further experimental development can

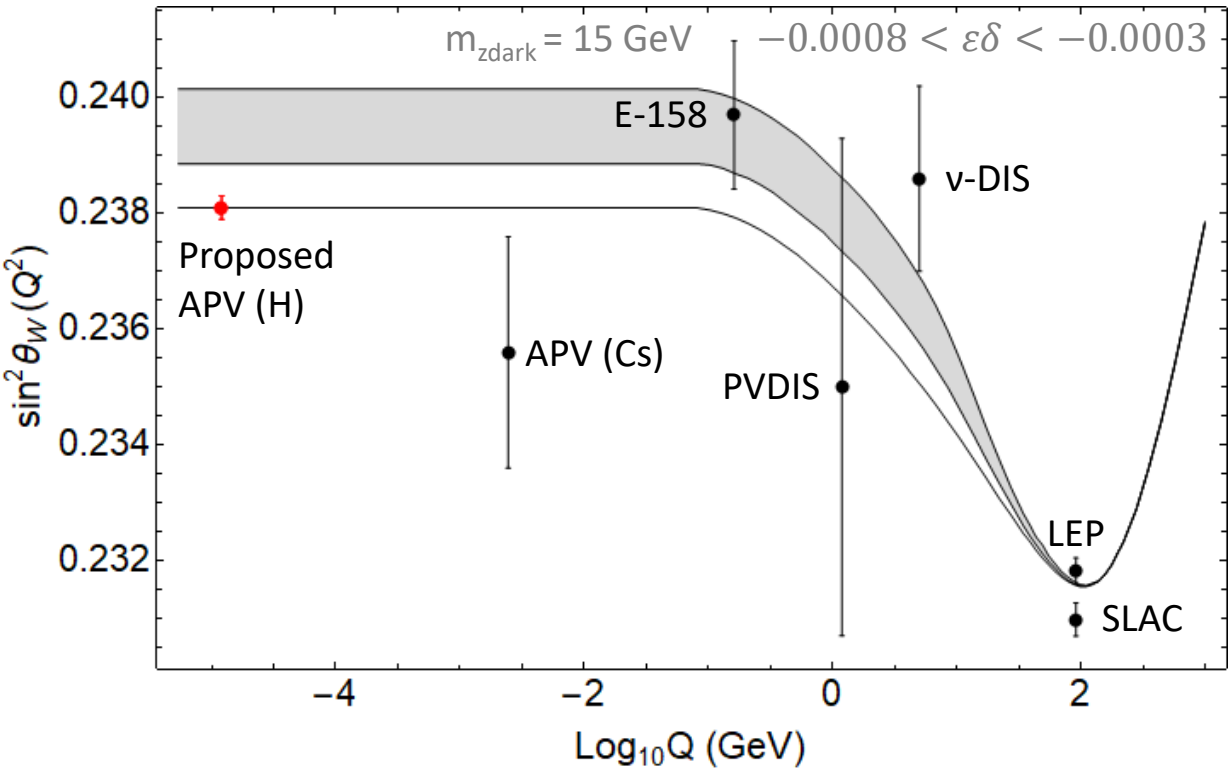

Figure 3.1: Running of the Weinberg mixing angle - Black points represent previously performed measurements (see text for details). The red point is placed on the energy axis where the momentum transfer in a hydrogen experiment would be [2] and located at the SM prediction.

be pursued in similar heavy atoms to reduce uncertainties, but the largest uncertainty contribution on the Cs experiment, for example, is theoretical ($\sigma_{exp} = 0.0012$ compared to $\sigma_{theory} = 0.0041$ on the mixing angle reported [42]).

The desire for a precise measurement on $\sin^2\theta_W$ along with the theoretical limitations of heavy atoms motivates us to examine the possibilities of a hydrogen PNC experiment. Being composed of a single proton and electron, hydrogen poses a much smaller theoretical limitations when interpreting results and extracting parity violating terms from experiments. Several parity violating experiments in hydrogen have been attempted. To date, groups at University of Michigan [47], University of Washington [48], and Yale University [49] have carried out experiments attempting to measure C_{2p}, which is the spin-dependent weak neutral current coupling constant, relating to the Weinberg mixing angle by $C_{2p} = 1/2(1 - 4\sin^2\theta_W)$. Williams in Michigan first reported an upper bound of $C_{2p} < 620$ in 1984 [50]. Later, in 1989, Hinds at Yale reported

$C_{2p} < 300$. The last and most recent limit was obtained by Fehrenbach, also at Michigan, of $C_{2p} = 1.5 \pm 1.5\ (statistical) \pm 22\ (systematic)$, while the expected value from SM predictions is $C_{2p} = 0.043$. Although the limits on C_{2p} were improving, none of the experiments were successful in observing parity violations.

Each of the hydrogen parity nonconservation experiments was plagued by systematic effects that made a detection of the violation impossible. These effects include motional electric fields, misalignments and inhomogeneities of magnetic fields, stray electric and magnetic fields, unwanted M1 transitions, and high background counts in photodetectors. Each of these groups created atomic hydrogen by forming a fast proton beam with a duoplasmatron, then sending this beam through a cesium vapor and cell where electron capture would generate hydrogen atoms, some of which were in the 2S metastable state. The atoms would then pass into an interaction region where transitions were driven from $2S_{1/2}, F = 1$ to $2S_{1/2}, F = 0$ by both a parity conserving route and parity nonconserving route, both involving microwave transitions. The atoms were then quenched to the ground states via 2S-2P transition and Lyman-alpha was detected. The interference between the PC and PNC transitions could be determined by repeating the experiment after inverting the experimental coordinate system and subtracting the two results. From this value, in principle C_{2p} can be determined.

One of the major problems in all of these experiments was the method of generating metastable 2S atoms. With electron capture, the newly formed hydrogen can be excited in very high lying states. It can then cascade down to the ground state while traveling through the apparatus, ultimately emitting a $L - \alpha$ (121 nm) photon and flooding the detector with noise. The second problem with the duoplasmatron method of generation is the velocity in which the atoms are traveling. On average, the hydrogen beam travels at 300,000 m/s, which creates large motional electric fields when traveling through a high magnetic interaction region. This causes the atoms to quench to the ground state, giving off $L - \alpha$ counts, which again results in large systematic errors.

3.2 Proposed Experiment

A newly designed measurement scheme is motivated by the use of a slow atomic hydrogen beam (300 m/s compared to previous 300,000 m/s) which mitigates many of the systematic effects previously observed. Using a slow beam of hydrogen greatly reduces the motional electric fields and by optically exciting the atoms to the 2S state, we ensure the population is strictly in that metastable state and will not cascade down to interfere with the rest of the experiment. In addition, we propose an experiment which utilizes optical transitions, opposed to previously performed microwave transitions, and we explore the use of a build-up cavity within the interaction region.

The scheme we propose involves a measurement of the interference between parity conserving (PC) and parity nonconserving (PNC) paths of a $2S_{1/2} \rightarrow 2P_{1/2}$ atomic transition, utilizing the $3S_{1/2}$ level as an intermediate state. Starting with a beam of cold atomic hydrogen in the metastable $2S_{1/2}$ state, we can excite atoms to the $3S_{1/2}$ state via a two-photon process with 1312 nm radiation and then cause stimulated emission to the $2P_{1/2}$ state with 656 nm radiation, resulting in a PC pathway. The PNC pathway comes from direct exchange of Z^0 bosons between the proton and electron, which mixes the $2S_{1/2}$ and $2P_{1/2}$ states.

As shown in [51], the weak interaction effects are enhanced by a factor of 21 at the 550 G level crossing in hydrogen. By decreasing the separation between energy levels, the energy denominator in the matrix element, $(\Delta E - i\Gamma_{2P})^{-1}$, is then limited to only the decay rate of the $2P_{1/2}$ state Applying this large magnetic field causes Zeeman shifts, shown in Fig. 3.3, but also mixes hyperfine states. In order to discuss the states of interest, we diagonalize the Hamiltonian of a free atoms in a magnetic field and define a new basis, following the nomenclature of Lamb [52]. The crossing hyperfine states of interest are shown in Fig. 3.2, labeled as $2f_0$ and $2\beta_0$. These states are linear combinations of (F, m_F) hyperfine states and the magnetic field mixing must be accounted for when computing dipole matrix elements.

The three interactions shown in Fig. 3.2 that we are interested in are the 656 nm one-photon electric dipole interaction, the 1312 nm two-photon electric dipole interaction, and the electroweak

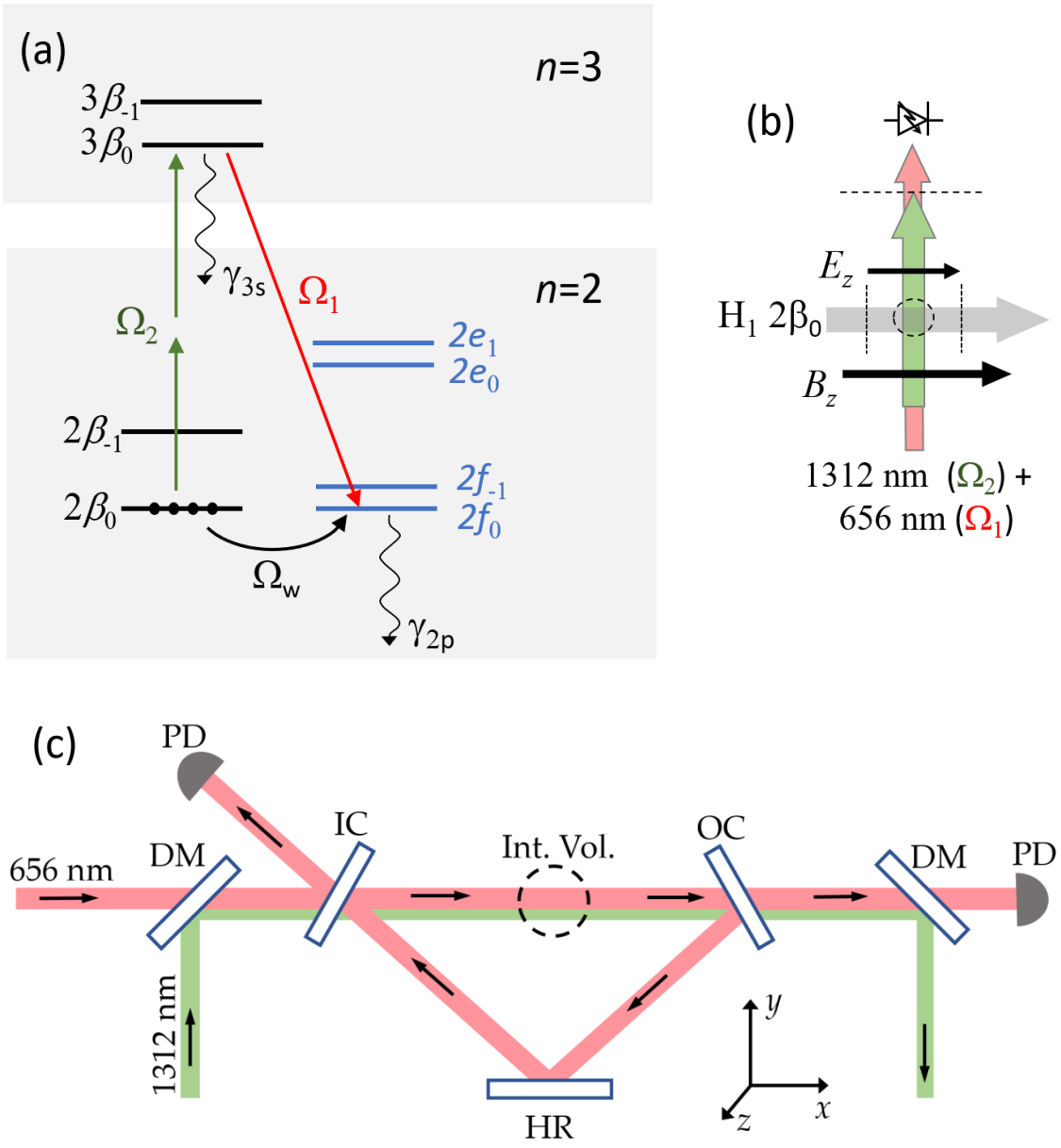

Figure 3.2: Measurement scheme showing the method of interfering parity conserving and parity nonconserving amplitudes. (a) The energy levels and their corresponding Rabi rates. (b) Directions of the applied fields within the proposed experiment. (c) Schematic of the proposed experiment. The 656 nm laser is built up in a low-finesse cavity comprised of an input coupler (IC), and output coupler (OC), and a high reflector (HR). To overlap and then separate the two fields, dichroic mirrors (DC) are used at the entrance and exit of the cavity.

interaction. Stark mixing with a static electric field is also applied to eliminate systematic uncertainties, explained later [53].

Our approach to quantify the feasibility of this measurement is to analyze the population dynamics of these interactions and to calculate an expected signal-to-noise ratio. In the following sections, all of the required calculations are discussed. The quantum mechanics and cavity QED calculations are used to derive the linear susceptibility of a beam of hydrogen atoms. Laser dynamics calculations are then used to determine the expected single-pass gain from a 656 nm laser traversing the atoms. Cavity enhancement calculations then show the benefits of building the experiment in a cavity. Systematic effects along with their relative size and proposed mitigation methods are also discussed.

3.3 Quantum Mechanics and Cavity QED

To analyze the feasibility of this proposed experiment, we consider the signal-to-noise ratio (SNR) of the measurement and discuss the total integration time required to produce a meaningful result. Several calculations are necessary to reach the final SNR – some mundane and others more involved – and these will be broken into subsections for clarity and completeness.

3.3.1 Dipole Matrix Elements

One-Photon Matrix Elements

The atomic states of interest are those separated by Zeeman splitting so we first need to compute the dipole matrix elements in the presence of a large magnetic field. To utilize Lamb's nomenclature, we form a new basis by diagonalizing the free-atom Hamiltonian H_a in a magnetic field. Starting in the hyperfine basis with quantum numbers $|n\ l\ j\ F\ m_F\rangle$ we construct a diagonal matrix of free-atom energies:

$$H_a = \begin{bmatrix} \Delta E_1 + E_1^{fs} + E_1^{hfs} & 0 & \dots & 0 \\ 0 & \Delta E_2 + E_2^{fs} + E_2^{hfs} & \dots & 0 \\ \vdots & \vdots & \ddots & \vdots \\ 0 & 0 & \dots & \Delta E_n + E_n^{fs} + E_n^{hfs} \end{bmatrix} \tag{3.2}$$

where ΔE_i, E_i^{fs}, and E_i^{hfs} are the energy differences between an arbitrary zero-energy point, fine structure splitting, and hyperfine splitting, respectively. Numerical values for E_i^{fs} and E_i^{hfs} values can be found in the Atomic Data and Nuclear Data Table. [54] Note that the fine structure splitting and most lines splittings are reported as centroid frequency differences. This means the frequency is weighted by the number total number of hyperfine states.

Applying a magnetic field to the system, we add the Zeeman Hamiltonian to H_a:

$$H_Z = \mu_B B_z \langle \psi_1 | L_z + g_s S_z | \psi_2 \rangle \tag{3.3}$$

where μ_B is the Bohr magneton (1.3996 MHz/G), B_z is the magnitude of the applied magnetic field (assuming for now a uniform field in the z-direction), L_z and S_z are the orbital and spin angular momentum operators.

L_z and S_z act on states as $L_z |\psi\rangle = m_l |\psi\rangle$ and $S_z |\psi\rangle = m_s |\psi\rangle$, which implies building the Zeeman Hamiltonian in the $|n\ l\ m_l\ m_i\ m_s\rangle$ basis. To convert from what will be refered to as the the "Coupled" basis, $|n\ l\ j\ F\ m_F\rangle$, to the so-called "Uncoupled" basis, $|n\ l\ m_l\ m_i\ m_s\rangle$, we can apply addition of angular momenta rules twice, using Clebsch-Gordan coefficients. The addition for each case of the two angular momenta are

$$|j\ m_j\ m_l\rangle = |m_l\rangle \sum_{m_i, m_s} |m_s\ m_i\rangle\, C^{m_j, J}_{m_i, I, m_s, S} \tag{3.4}$$

and

$$|F\ m_f\ j\rangle = \sum_{m_l, m_j} |j\ m_j\ m_l\rangle\, C^{m_F, F}_{m_l, l, m_j, j}. \tag{3.5}$$

We can insert Eqn. 3.4 into Eqn. 3.5 to get an overall change of basis from the "Uncoupled" basis to the "Coupled" basis:

$$|F\ m_f\ j\rangle = \sum_{\substack{m_i,m_s \\ m_l,m_j}} |m_l\ m_s\ m_i\rangle\, C^{m_F,F}_{m_l,l,m_j,j} C^{m_j,J}_{m_i,I,m_s,S} \tag{3.6}$$

and then we can generate the Zeeman Hamiltonian by inserting Eqn. 3.6 into Eqn. 3.3.

Now we diagonalize the new Hamiltonian, $H_a + H_Z$ to get a new basis, where we can now use Lamb's nomenclature. Figure 3.3 shows the degeneracy breaking of the $2S_{1/2}$ and $2P_{1/2}$ states with an applied magnetic field. The $2S_{1/2}$ states are labeled α_i and β_i and the $2P_{1/2}$ states labeled e_i and f_i where i is $m_j + m_i$.

Having defined the states within a magnetic field, we can now calculate dipole matrix elements. These are calculated by an overlap integral containing a position operator:

$$\langle\psi_1|q\vec{r}|\psi_2\rangle = q\int_V \psi_1^*\ \vec{r}\ \psi_2\ dV \tag{3.7}$$

Since the spatial wavefunctions are functions of n, l, and m_l, we convert the states of interest into the uncoupled basis before integrating. Our Zeeman basis, ψ_Z can be expressed as a sum of "coupled" basis states, which can then be changed into the uncoupled basis with the use of Eqn. 3.6 to calculate the dipole matrix elements. Each matrix element has the form

$$\langle\psi_1|q\vec{r}|\psi_2\rangle = q\int_V \psi^*_{1_{nlm}}(r,\theta,\phi)\ \vec{r}\ \psi_{2_{nlm}}(r,\theta,\phi)\ dV, \tag{3.8}$$

where $\psi_{i_{nlm}}(r,\theta,\phi) = R_{n,l}(\vec{r})Y_{l,m}(\theta,\phi)$ is the hydrogen wavefunction, composed of a radial function $R_{n,l}(\vec{r})$ and angular function $Y_{l,m}(\theta,\phi)$, which involve generalized Laguerre polynomials

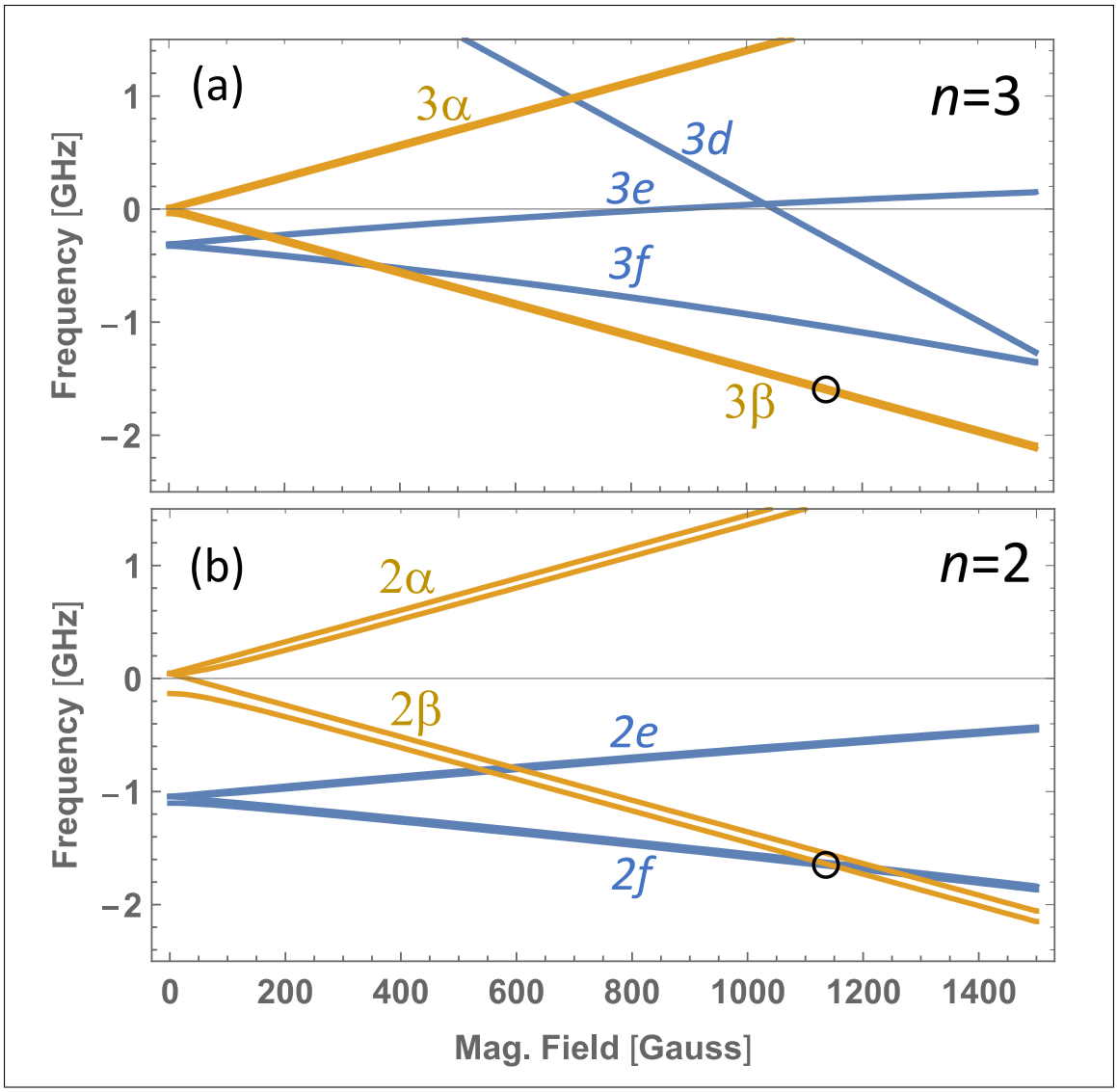

Figure 3.3: Hydrogen level structure of the $n = 2$ (a) and $n = 3$ (b) manifolds in the presence of a magnetic field. The magnetic field of interest near 1200 G at the location of the level crossing in (b) is highlighted in both figures.

Table 3.1: Transition matrix elements between both $2\beta_0$ and $3\beta_0$ and each of the the $2P_{1/2}$ states. The values are computer for $x-$ and $z-$polarization and are reported in units of ea_0

	$z\,\|3\beta_0\rangle$	$x\,\|3\beta_0\rangle$	$z\,\|2\beta_0\rangle$	$x\,\|2\beta_0\rangle$
$\langle 2e_1\|$	0	0.3267	0	1.8085
$\langle 2e_0\|$	0.0117	0	0.0951	0
$\langle 2f_{-1}\|$	0	0.00237	0	0.0447
$\langle 2f_0\|$	0.3439	0	01.903	0

$L_n^{\alpha}(\vec{r})$ and associated Legendre polynomials $P_{l,m}(\cos\theta)$. Each of these functions is defined as

$$R_{n,l}(r) = \sqrt{\left(\frac{2}{na_0}\right)^3 \frac{(n-l-1)!}{2n(n+l)!}} e^{-r/na_0} \left(\frac{2r}{na_0}\right)^l L_{n-l-1}^{2l+1}\left(\frac{2r}{na_0}\right) \tag{3.9}$$

$$Y_{l,m}(\theta,\phi) = (-1)^m \sqrt{\frac{(2l+1)}{4\pi}\frac{(l-m)!}{(l+m)!}} P_{l,m}(\cos\theta) e^{im\phi}, \tag{3.10}$$

where a_0 is the Bohr radius.

Using the described analysis, we can compute the matrix elements of interest. At an applied field of 1156 G, Table 3.1 shows the magnitudes of each electric dipole matrix element considered in this analysis.

The transition matrix elements are related to the Rabi frequency by

$$\Omega_{1p} = -\frac{E_0}{\hbar} \langle g \,|\, q\vec{r} \,|\, e\rangle \cdot \hat{E}_0 \tag{3.11}$$

with E_0 being the electric field amplitude of the radiation used for driving the transition.

Two-Photon Matrix Elements

The measurement scheme also involves a two-photon transition. To compute the two-photon transition elements, we can follow the analysis provided in [55] where the matrix elements are

defined as

$$\beta_{ge} = -\frac{e^2}{2hc\epsilon_0} \left\langle e \left| z \frac{1}{H_0 - (E_g + \hbar\omega_L)} z \right| g \right\rangle, \tag{3.12}$$

where H_0 is the free-atom Hamiltonian, E_g is the ground state energy, and ω_L is the applied radiation field frequency. The inner product can be written in terms of a Green's function, g_l, and recast in the form of an integral.

$$\left\langle e \left| z \frac{1}{H_0 - (E_g + \hbar\omega_L)} z \right| g \right\rangle = \sum_{l,m} \int_{V_1,V_2} g_l \psi_1 \psi_2 Y_{l,m}(\theta_1, \phi_1) Y^*_{l,m}(\theta_2, \phi_2) z_1 z_2 dV_1 dV_2 \tag{3.13}$$

The angular part of the integral can be performed separately from the radial, and in the case of an nS to $n'S$ transition, the result is simply 1/3. Simplifying, we are left with an expression for β_{ge} in terms of an integral over the Green's function and radial wave functions:

$$\beta_{ge} = -\frac{e^2}{6hc\epsilon_0} \int_{r_1,r_2} g_l R^{(1)}_{n,l}(r_1) R^{(2)}_{n,l}(r_2) r_1^3 r_2^3 dr_1 dr_2. \tag{3.14}$$

As noted in [55], several methods of calculating the Green's function exist. One of the least computationally intensive methods follows [56] and their result is

$$g_l(r_1, r_2, \nu) = \frac{m a_0 \nu}{\hbar^2} \frac{\Gamma(l + 1 - \nu)}{(2l+1)!} \frac{1}{r_1 r_2} M_{\nu, l+1/2}\left(\frac{2r_<}{a_0 \nu}\right) W_{\nu, l+1/2}\left(\frac{2r_>}{a_0 \nu}\right), \tag{3.15}$$

$$\text{where } \nu = \frac{\hbar}{a_0}\sqrt{-\frac{1}{2mE}}, \quad E = -\frac{e^2}{2a_0 n^2}. \tag{3.16}$$

The functions M and W are Whittaker functions with $r_<$ and $r_>$ being the respective lesser or greater between r_1 and r_2. The approach described here reproduces the numerical values in [55] and a values for $n = 1 - 4$ are shown in Table 3.2 for reference.

Table 3.2: Numerical values for two-photon transition matrix elementsβ_{ge} in units of Hz/(W/m^2).

n	$1S \Leftrightarrow nS$	$2S \Leftrightarrow nS$	$3S \Leftrightarrow nS$
2	3.68×10^-5		
3	1.00×10^-5	1.23×10^-3	
4	5.13×10^-6	7.79×10^-5	1.04×10^-2
5	3.28×10^-6	-4.40×10^-5	-1.63×10^-3
6	2.35×10^-6	-6.89×10^-5	-3.13×10^-3
7	1.80×10^-6	-7.26×10^-5	-4.93×10^-3
8	1.44×10^-6	-6.99×10^-5	-1.38×10^-2
9	1.18×10^-6	-6.53×10^-5	1.21×10^-2
10	9.98×10^-7	-6.01×10^-5	3.83×10^-3
11	8.58×10^-7	-5.52×10^-5	2.18×10^-3
12	7.48×10^-7	-5.06×10^-5	1.48×10^-3

From the transition matrix elements, the two-photon Rabi frequency is

$$\Omega = 4\pi\beta_{ge}I, \tag{3.17}$$

where I is the electromagnetic wave intensity.

3.4 Interaction Hamiltonian

Having defined the transition matrix elements in the previous section, we can now use those to set up the interaction Hamiltonian. To reiterate, the major interactions we are consider are: a two-photon transition from $2S_{1/2} \rightarrow 3S_{1/2}$, whose states will be labeled $|2\beta_0\rangle \rightarrow |3\beta_0\rangle$, a one-photon transition from $3S_{1/2} \rightarrow 2P_{1/2}$, labeled $|3\beta_0\rangle \rightarrow |2f_0\rangle$, and the weak interaction between states $|2\beta_0\rangle \rightarrow |2f_0\rangle$.

The total Hamiltonian is the sum of several terms,

$$H = H_a + H_{1p} + H_{2p} + H_W. \tag{3.18}$$

is determined from the atomic energy level splittings. Setting $|3\beta_0\rangle$ to be the zero-point energy, the atomic state Hamiltonian can be written as

$$H_a = \hbar\omega_{3\beta_0 2\beta_0} |2\beta_0\rangle \langle 2\beta_0| + \hbar\omega_{3\beta_0 2f_0} |2f_0\rangle \langle 2f_0| , \tag{3.19}$$

where ω_{if} is the angular frequency between initial state i and final state f.

H_{1p} is the one-photon electric dipole Hamiltonian which has the form: $H_{1p} = -\vec{d} \cdot \vec{E}$, where $\vec{d} = \langle 2f_0|q\vec{r}|3\beta_0\rangle (|3\beta_0\rangle \langle 2f_0| + |2f_0\rangle \langle 3\beta_0|)$ and $\vec{E} = \frac{E_o}{2}(e^{i\omega_1 t} + e^{-i\omega_1 t})\hat{E}_o$. This product gives:

$$H_{1p} = -\frac{E_o}{2} \langle 2f_0|q\vec{r}|3\beta_0\rangle \cdot \hat{E}_o (e^{i\omega_1 t} |3\beta_0\rangle \langle 2f_0| + e^{-i\omega_1 t} |3\beta_0\rangle \langle 2f_0| + e^{i\omega_1 t} |2f_0\rangle \langle 3\beta_0| + e^{-i\omega_1 t} |2f_0\rangle \langle 3\beta_0|). \tag{3.20}$$

Now, since $|3\beta_0\rangle \langle 2f_0|$ oscillates as $e^{-i\omega_{2f_0 f 3\beta_0} t}$, we have two terms in H_{1p} that are very fast, which can be ignored. This is the "Rotating Wave Approximation". Keeping the slowly oscillating terms, we're left with:

$$H_{1p} = -\frac{E_o}{2} \langle 2f_0|q\vec{r}|3\beta_0\rangle \cdot \hat{E}_o (e^{i\omega_1 t} |3\beta_0\rangle \langle 2f_0| + e^{-i\omega_1 t} |2f_0\rangle \langle 3\beta_0|) \tag{3.21}$$

We can now define the Rabi frequency and make the substitution $\Omega_{1p} = -\frac{E_o}{\hbar} \langle 2f_0|q\vec{r}|3\beta_0\rangle \cdot \hat{E}_o$, and simplify to

$$H_{1p} = \frac{\Omega_{1p}}{2} (e^{i\omega_1 t} |3\beta_0\rangle \langle 2f_0| + e^{-i\omega_1 t} |2f_0\rangle \langle 3\beta_0|). \tag{3.22}$$

The two-photon Hamiltonian is similar, with a starting point being Eq. (2) in [55]:

$$H_{2p} = \frac{\Omega_{2p}}{2} (e^{i\omega_{2p} t} + e^{-i\omega_{2p} t})^2 (|2\beta_0\rangle \langle 3\beta_0| + |3\beta_0\rangle \langle 2\beta_0|) \tag{3.23}$$

where $\Omega_{2p} = 4\pi\hbar\beta_{ge} I(t)$. Expanding these terms and again making the RWA by dropping the quickly oscillating terms, we're left with

$$H_{2p} = \frac{\Omega_{2p}}{2} (e^{i2\omega_{2p} t} |3\beta_0\rangle \langle 2\beta_0| + e^{-i2\omega_{2p} t} |2\beta_0\rangle \langle 3\beta_0|) \tag{3.24}$$

Lastly, we have an interaction Hamiltonian describing the weak coupling between states $|2\beta_0\rangle$ and $|2f_0\rangle$. This can also be written in terms of a weak Rabi frequency

$$H_W = \Omega_W |2f_0\rangle \langle 2\beta_0| + \Omega_W^* |2\beta_0\rangle \langle 2f_0| \tag{3.25}$$

where $\Omega_W = i\hbar(C_{1p} + 1.1C_{2p}) \langle 2f_0|V_W|2\beta_0\rangle$ [57].

Having defined the components of the total Hamiltonian, we can now work towards forming a matrix. Assume the state of our atoms can be described by $\Psi(t) = C_{3\beta_0}(t) |3\beta_0\rangle + C_{2\beta_0}(t) |2\beta_0\rangle + C_{2f_0}(t) |2f_0\rangle$. Taking the time derivative of $\Psi(t)$ and inserting the result into Schrodinger's Equation, $i\hbar\partial\Psi/\partial t = H\Psi$, we get

$$\begin{aligned}
&i\hbar(\dot{C}_{3\beta_0}(t) |3\beta_0\rangle + \dot{C}_{2\beta_0}(t) |2\beta_0\rangle + \dot{C}_{2f_0}(t) |2f_0\rangle) \\
&\quad = H(C_{3\beta_0}(t) |3\beta_0\rangle + C_{2\beta_0}(t) |2\beta_0\rangle + C_{2f_0}(t) |2f_0\rangle) \\
&\quad = (H_a + H_{1p} + H_2 + H_W)(C_{3\beta_0}(t) |3\beta_0\rangle + C_{2\beta_0}(t) |2\beta_0\rangle + C_{2f_0}(t) |2f_0\rangle) \\
&\quad = (\hbar\omega_{3\beta_0 2\beta_0} |2\beta_0\rangle \langle 2\beta_0| + \hbar\omega_{3\beta_0 2f_0} |2f_0\rangle \langle 2f_0| + \frac{\Omega_{1p}}{2}(e^{i\omega_1 t} |3\beta_0\rangle \langle 2f_0| + e^{-i\omega_1 t} |2f_0\rangle \langle 3\beta_0|) \\
&\quad + \frac{\Omega_{2p}}{2}(e^{i2\omega_{2p}t} |3\beta_0\rangle \langle 2\beta_0| + e^{-i2\omega_{2p}t} |2\beta_0\rangle \langle 3\beta_0|) + \Omega_W |2f_0\rangle \langle 2\beta_0| + \Omega_W^* |2\beta_0\rangle \langle 2f_0|) \\
&\quad \times (C_{3\beta_0}(t) |3\beta_0\rangle + C_{2\beta_0}(t) |2\beta_0\rangle + C_{2f_0}(t) |2f_0\rangle)
\end{aligned} \tag{3.26}$$

Since our states are orthogonal, we can simplify the RHS of 3.26 by distributing the kets. Then we have

$$\begin{aligned}
&i\hbar(\dot{C}_{3\beta_0}(t) |3\beta_0\rangle + \dot{C}_{2\beta_0}(t) |2\beta_0\rangle + \dot{C}_{2f_0}(t) |2f_0\rangle) \\
&\qquad = C_{3\beta_0}(t)(\frac{\Omega_{1p}}{2} e^{-i\omega_1 t} |2f_0\rangle + \frac{\Omega_{2p}}{2} e^{-i2\omega_{2p}t} |2\beta_0\rangle) \\
&\qquad + C_{2\beta_0}(t)(\hbar\omega_{3\beta_0 2\beta_0} |2\beta_0\rangle + \frac{\Omega_{2p}}{2} e^{i2\omega_{2p}t} |3\beta_0\rangle + \Omega_W |2f_0\rangle) \\
&\qquad + C_{2f_0}(t)(\hbar\omega_{3\beta_0 2f_0} |2f_0\rangle + \frac{\Omega_{1p}}{2} e^{i\omega_1 t} |3\beta_0\rangle + \Omega_W^* |2\beta_0\rangle)
\end{aligned} \tag{3.27}$$

Multiplying in turn Eqn. 3.27 by $\langle 3\beta_0|$, $\langle 2\beta_0|$, and $\langle 2f_0|$, we get a set of coupled differential equations:

$$\begin{aligned} i\hbar\dot{C}_{3\beta_0} &= C_{2\beta_0}\frac{\Omega_{2p}}{2}e^{i2\omega_2 t} + C_{2f_0}\frac{\Omega_{1p}}{2}e^{i\omega_1 t} \\ i\hbar\dot{C}_{2\beta_0} &= C_{2\beta_0}\hbar\omega_{3\beta_0 2\beta_0} + C_{3\beta_0}\frac{\Omega_{2p}}{2}e^{-2\omega_{2p}t} + C_{2f_0}\Omega_W^* \\ i\hbar\dot{C}_{2f_0} &= C_{2f_0}\hbar\omega_{3\beta_0 2f_0} + C_{3\beta_0}\frac{\Omega_{1p}}{2}e^{-i\omega_1 t} + C_{2\beta_0}\Omega_W \end{aligned} \tag{3.28}$$

We can consider the problem in any rotating frame of reference at a frequency of our choosing. Moving into a rotating frame at frequency ω_1, let $C_{2f_0} = \tilde{C}_{2f_0}e^{-i\omega_1 t}$ and $C_{2\beta_0} = \tilde{C}_{2\beta_0}e^{-i\omega_1 t}$. Substituting these into Eqn. 3.28 and simplifying, we get

$$\begin{aligned} i\hbar\dot{C}_{3\beta_0} &= C_{2\beta_0}\frac{\Omega_{2p}}{2}e^{i\Delta_2 t} + C_{2f_0}\frac{\Omega_{1p}}{2} \\ i\hbar\dot{C}_{2\beta_0} &= C_{2\beta_0}\hbar\Delta_{3\beta_0 2\beta_0} + C_{3\beta_0}\frac{\Omega_{2p}}{2}e^{-\Delta_2 t} + C_{2f_0}\Omega_W^* \\ i\hbar\dot{C}_{2f_0} &= C_{2f_0}\hbar\Delta_{3\beta_0 2f_0} + C_{3\beta_0}\frac{\Omega_{1p}}{2} + C_{2\beta_0}\Omega_W \end{aligned} \tag{3.29}$$

where Δ_2 is the frequency difference between the one- and two-photon radiation sources, and Δ_i are the frequency differences between the single photon laser frequency and the labeled transition frequencies. From Eqn. 3.29, we can pick out the Hamiltonian by examination. Adding arbitrary phase ϕ_1 and ϕ_2 to the electric fields (the relative phase maps onto the laser phase, which will be used as a parity reversal), the total Hamiltonian for the three interactions among the three states is

$$H = \begin{pmatrix} \hbar\Delta\omega_{3\beta_0 2f_0} & \Omega_W & \frac{\Omega_{1p}}{2}e^{-i\phi_1} \\ \Omega_W^* & \hbar\Delta\omega_{3\beta_0 2\beta_0} & \frac{\Omega_{2p}}{2}e^{-i\Delta_{\omega_2}t - i2\phi_2} \\ \frac{\Omega_{1p}}{2}e^{i\phi_1} & \frac{\Omega_{2p}}{2}e^{i\Delta_{\omega_2}t + i2\phi_2} & 0 \end{pmatrix} \tag{3.30}$$

3.4.1 Spontaneous Decay

Because the Hamiltonian derived above does not account for spontaneous emission, we must add in the decay rates post-hoc in order to properly describe the population dynamics. This can be

performed in the coupled set of equations, resulting in

$$\begin{aligned} i\hbar\dot{C}_{3\beta_0} &= C_{2\beta_0}\frac{\Omega_{2p}}{2}e^{i\Delta_2 t} + C_{2f_0}\frac{\Omega_{1p}}{2} - i\hbar\Gamma_{3\beta_0}/2 \\ i\hbar\dot{C}_{2\beta_0} &= C_{2\beta_0}\hbar\Delta_{3\beta_0 2\beta_0} + C_{3\beta_0}\frac{\Omega_{2p}}{2}e^{-\Delta_2 t} + C_{2f_0}\Omega_W^* \\ i\hbar\dot{C}_{2f_0} &= C_{2f_0}\hbar\Delta_{3\beta_0 2f_0} + C_{3\beta_0}\frac{\Omega_{1p}}{2} + C_{2\beta_0}\Omega_W - i\hbar\Gamma_{2f_0}/2, \end{aligned} \tag{3.31}$$

where Γ_{2f_0} is approximately 100 MHz and $\Gamma_{3\beta_0}$ is approximately 700 kHz.

A more formal method of accounting for the spontaneous decay and the effect on coherences between the states is the density matrix approach. The Liouville equation describes the time evolution for a quantum system without loss. To account the decays, we can add the Lindblad superoperator, making the so-called Lindblad Master Equation:

$$\dot{\rho} = i[\rho, H] + \mathcal{L}(\rho) \tag{3.32}$$

Here, $\mathcal{L}(\rho) = -1/2\sum_m\{C_m^\dagger C_m, \rho\} + C_m\rho C_m^\dagger$, with $C_m = \sqrt{\Gamma_m}\,|f\rangle\langle m|$ is any possible decay channel of rate Γ where population is transferred to state $|f\rangle$. In our problem, we are concerned with three particular states, two of which have decay channels to the ground state. This requires a 4x4 density matrix and thus four basis states to construct the Lindblad term:

$$|2f_0\rangle = \begin{pmatrix} 1 \\ 0 \\ 0 \\ 0 \end{pmatrix} \qquad |2\beta_0\rangle = \begin{pmatrix} 0 \\ 1 \\ 0 \\ 0 \end{pmatrix} \qquad |3\beta_0\rangle = \begin{pmatrix} 0 \\ 0 \\ 1 \\ 0 \end{pmatrix} \qquad |1S\rangle = \begin{pmatrix} 0 \\ 0 \\ 0 \\ 1 \end{pmatrix} \tag{3.33}$$

We have three terms to sum over in our Lindblad term:

$$\begin{aligned} C_{2f_0 1S} &= \sqrt{\Gamma_{2f_0 1S}}\,|1S\rangle\langle 2f_0| \\ C_{3\beta_0 2f_0} &= \sqrt{\Gamma_{3\beta_0 2f_0}}\,|2f_0\rangle\langle 3\beta_0| \\ C_{3\beta_0 1S} &= \sqrt{\Gamma_{3\beta_0 1S}}\,|1S\rangle\langle 3\beta_0| \end{aligned} \tag{3.34}$$

where C_{if} describes the decay from the $|i\rangle$ state to $|f\rangle$ state. Using vector notation and performing the outer products, each of the C_m terms is a matrix:

$$C_{2f_01S} = \sqrt{\Gamma_{2f_01S}} \begin{pmatrix} 1 & 0 & 0 & 0 \\ 0 & 0 & 0 & 0 \\ 0 & 0 & 0 & 0 \\ 0 & 0 & 0 & 0 \end{pmatrix} \qquad C_{3\beta_02f_0} = \sqrt{\Gamma_{3\beta_02f_0}} \begin{pmatrix} 0 & 0 & 1 & 0 \\ 0 & 0 & 0 & 0 \\ 0 & 0 & 0 & 0 \\ 0 & 0 & 0 & 0 \end{pmatrix}$$
$$C_{3\beta_01S} = \sqrt{\Gamma_{3\beta_01S}} \begin{pmatrix} 0 & 0 & 0 & 0 \\ 0 & 0 & 0 & 0 \\ 0 & 0 & 0 & 0 \\ 0 & 0 & 1 & 0 \end{pmatrix} \tag{3.35}$$

Inserting these C_m matrices into the Lindblad expression and simplifying, we get:

$$\mathcal{L} = -\frac{1}{2} \begin{pmatrix} 2(\Gamma_{f1}\rho_{ff} - \Gamma_{3f}\rho_{33}) & \Gamma_{f1}\rho_{f2} & (\Gamma_{f1} + \Gamma_{3f} + \Gamma_{31})\rho_{f3} & \Gamma_{f1}\rho_{f1} \\ \Gamma_{f1}\rho_{2f} & 0 & (\Gamma_{3f} + \Gamma_{31})\rho_{23} & 0 \\ (\Gamma_{f1} + \Gamma_{3f} + \Gamma_{31})\rho_{3f} & (\Gamma_{3f} + \Gamma_{31})\rho_{32} & 2(\Gamma_{3f} + \Gamma_{31})\rho_{33} & (\Gamma_{3f} + \Gamma_{31})\rho_{31} \\ \Gamma_{f1}\rho_{1f} & 0 & (\Gamma_{3f} + \Gamma_{31})\rho_{13} & -2(\Gamma_{31}\rho_{33} + \Gamma_{f1}\rho_{ff}) \end{pmatrix} \tag{3.36}$$

We can now solve the Lindblad master equation to get out a time-dependent density matrix, which tracks both the populations of each state as well as the coherence between states.

3.4.2 Steady State Solutions

Consider the on-resonant, steady state case of Eqn. 3.31. Assume a weak coupling between the $|2\beta_0\rangle$ and $|3\beta_0\rangle$ state so that $C_{2\beta_0} \approx 1$. Then we have a simple set of algebraic equations, which can be solved for the population coefficients.

$$
\begin{aligned}
0 &= C_{2f_0}\frac{\Omega_{1p}}{2}e^{i\phi} + \frac{\Omega_{2p}}{2} + -i\Gamma_{3\beta_0}/2 \\
0 &= C_{3\beta_0}\frac{\Omega_{1p}}{2}e^{-i\phi} + \Omega_W - i\Gamma_{2f_0}/2 \\
0 &= C_{3\beta_0}\frac{\Omega_{2p}}{2} + C_{2f_0}\Omega_W^*.
\end{aligned}
\tag{3.37}
$$

The pair of solutions for C_{2f_0} and $C_{3\beta_0}$ are

$$
\begin{aligned}
C_{3\beta_0} &= -\frac{i\Omega_{2p}}{\Gamma_{3\beta_0}} \\
C_{2f_0} &= -e^{-i\phi}\frac{\Omega_{1p}\Omega_{2p}}{\Gamma_{3\beta_0}\Gamma_{2f_0}} - 2i\frac{\Omega_W}{\Gamma_{2f_0}}.
\end{aligned}
\tag{3.38}
$$

Using these solutions, we can construct the off-diagonal density matrix term ρ_{3f} which describes the steady-state coherence between the $|3\beta_0\rangle$ and $|2f_0\rangle$ states, which will be used in determining the linear susceptibility of our atomic system. The linear susceptibility is proportional to single-pass gain through a lasing medium. Sections 3.6 and 3.7 explain how the susceptibility is used in calculating an expected photon flux out of a cavity to generate a PNC signal.

$$
\rho_{3f} = \frac{2\Omega_2\Omega_W}{\Gamma_{3\beta_0}\Gamma_{2f_0}} + i\frac{\Omega_1\Omega_2^2}{\Gamma_{3\beta_0}^2\Gamma_{2f_0}}e^{i\phi},
\tag{3.39}
$$

3.5 Cavity QED

The preceding analysis is sufficient for understanding the population dynamics of the atomic system. However, as will be discussed in the upcoming sections, knowledge of the photon number expectation value is necessary to conduct a full analysis of this experiment. Keeping in mind the proposed experiment is being conducted within a cavity, a cavity QED treatment is presented here.

The cavity QED treatment of this problem relies on utilizing the time-dependent density operator to solve for time varying expectation values. Specifically, we want to solve for the time dependent expectation value $\langle \dot{a} \rangle$ of the photon number within our buildup cavity:

$$\langle \dot{a} \rangle = Tr[a\dot{\rho}] \tag{3.40}$$

Since this calculation depends on $\dot{\rho}$, we can use the Lindblad master equation to evaluate this expression. In this case, we include spontaneous decay from the $|3\beta_0\rangle$ and $|2f_0\rangle$ states, as well as total mirror loss κ.

$$\dot{\rho} = -\frac{i}{\hbar}[\rho, H] + \kappa\mathcal{L}[a]\rho + \Gamma_3\mathcal{L}[\sigma_{3f}]\rho + \Gamma_f\mathcal{L}[\sigma_{fg}]\rho \tag{3.41}$$

with the Lindblad operators in this case taking the form

$$\Gamma\mathcal{L}[\sigma]\rho = \Gamma\left(\sigma\rho\sigma^\dagger - \frac{1}{2}(\sigma^\dagger\rho\sigma + \rho\sigma^\dagger\sigma)\right) \tag{3.42}$$

The Hamiltonian used is a sum of the cavity states, H_c, the seed laser, H_L, the energy states of $|2f_0\rangle$ and $|2\beta_0\rangle$ (again setting $|3\beta_0\rangle$ to be the atomic zero-point energy), H_{2f_0} and $H_{2\beta_0}$, the Jaynes-Cummings interaction between photons and atoms, H_{AF}, the two-photon atomic interaction, H_{2p}, and the weak interaction, H_W.

$$H = H_c + H_L + H_{2f_0} + H_{2\beta_0} + H_{AF} + H_{2p} + H_W \tag{3.43}$$

The following Hamiltonian terms are similar to the Schrodinger approach, but written here in terms of atomic σ and photon number a raising and lowering operators:

$$
\begin{aligned}
H_c &= \hbar\omega a^\dagger a \\
H_L &= \hbar\mathcal{E}(ae^{i\omega t} + a^\dagger e^{-i\omega t}) \\
H_\beta &= \hbar\omega_\beta \sigma_{\beta\beta} \\
H_f &= \hbar\omega_f \sigma_{ff} \\
H_{AF} &= \hbar g(\vec{r})(\sigma_{f3}a^\dagger + \sigma_{f3}^\dagger a) \\
H_{2L} &= \hbar\frac{\Omega_{2p}}{(}\sigma_{\beta 3}^\dagger + \sigma_{\beta 3}) \\
H_W &= \hbar(\Omega_W \sigma_{f\beta} + \Omega_W^* \sigma_{f\beta}^\dagger)
\end{aligned}
\tag{3.44}
$$

Having defined the components, we can now calculate the expectation value of the cavity photon number by inserting Eqn. 3.41 into Eqn. 3.40.

$$
\begin{aligned}
\langle \dot{a} \rangle &= Tr\left[a\left(-\frac{i}{\hbar}[\rho, H] + \kappa\mathcal{L}[a]\rho + \Gamma_3\mathcal{L}[\sigma_{3f}]\rho + \Gamma_f\mathcal{L}[\sigma_{fg}]\rho\right)\right] \\
&= Tr\left[a\left(-\frac{i}{\hbar}[\rho, H]\right)\right] + Tr\left[a\kappa\mathcal{L}[a]\rho\right] + Tr\left[a\Gamma_3\mathcal{L}[\sigma_{3f}]\rho\right] + Tr\left[a\Gamma_f\mathcal{L}[\sigma_{fg}]\rho\right]
\end{aligned}
\tag{3.45}
$$

Now there are four distinct trace terms to consider. The first term can be rewritten and arranged using permutation rules of trace algebra and expressed as

$$
\begin{aligned}
= Tr\left[a\left(-\frac{i}{\hbar}[\rho, H]\right)\right] &= -\frac{i}{\hbar}Tr\left[a\rho H - aH\rho\right] \\
&= -\frac{i}{\hbar}Tr\left[\rho H a - aH\rho\right] \\
&= -\frac{i}{\hbar}\sum_i Tr\left[\rho H_i a - aH_i\rho\right] \\
& i \in \{c, L, \beta, f, AF, 2L, W\}
\end{aligned}
\tag{3.46}
$$

Each Hamiltonian term can now be calculated. The case of $\langle \dot{a} \rangle$ will be shown in detail, but the results for the atomic terms will only be presented at the end, though the same process is followed.

$$
\begin{aligned}
H_c : -\frac{i}{\hbar}Tr\Big[\rho H_c a - a H_c \rho\Big] &= -\frac{i}{\hbar}Tr\Big[\rho(\hbar\omega a^\dagger a)a - a(\hbar\omega a^\dagger a)\rho\Big] \\
&= -i\omega Tr\Big[\rho a^\dagger a a - a a^\dagger a \rho\Big] \\
&= -i\omega Tr\Big[\rho a^\dagger a a - \rho a a^\dagger a\Big] \\
&= -i\omega Tr\Big[\rho [a^\dagger a] a\Big] \\
&= -i\omega Tr\Big[\rho(-1)a\Big] \\
&= i\omega Tr\Big[\rho a\Big] \\
&= i\omega\langle a\rangle
\end{aligned}
\tag{3.47}
$$

Here, the simplification simply comes from the permutation of traces, the fact that $[a^\dagger a] = -1$, and $\langle a\rangle = Tr[\rho a]$. Applying each of these rules to the remaining Hamiltonian terms, along with the additional fact that a commutes with σ, the following terms are generated for $\langle \dot{a}\rangle$:

$$
\begin{aligned}
H_c : -\frac{i}{\hbar}\ & Tr\Big[\rho H_c a - a H_c \rho\Big] && = i\omega\langle a\rangle \\
H_L : -\frac{i}{\hbar}\ & Tr\Big[\rho H_L a - a H_L \rho\Big] && = i\mathcal{E}e^{-i\omega t} \\
H_\beta : -\frac{i}{\hbar}\ & Tr\Big[\rho H_\beta a - a H_\beta \rho\Big] && = 0 \\
H_f : -\frac{i}{\hbar}\ & Tr\Big[\rho H_f a - a H_f \rho\Big] && = 0 \\
H_{AF} : -\frac{i}{\hbar} & Tr\Big[\rho H_{AF} a - a H_{AF} \rho\Big] && = ig(\vec{r})\langle\sigma_{f3}\rangle \\
H_{2L} : -\frac{i}{\hbar}\ & Tr\Big[\rho H_{2L} a - a H_{2L} \rho\Big] && = 0 \\
H_W : -\frac{i}{\hbar}\ & Tr\Big[\rho H_W a - a H_W \rho\Big] && = 0 \\
\mathcal{L}[a] : \quad & Tr\Big[a\kappa\mathcal{L}[a]\rho\Big] && = -\frac{\kappa}{2}\langle a\rangle \\
\mathcal{L}[\sigma_{3f}] : \ & Tr\Big[a\Gamma_3\mathcal{L}[\sigma_{3f}]\rho\Big] && = 0 \\
\mathcal{L}[\sigma_{fg}] : \ & Tr\Big[a\Gamma_f\mathcal{L}[\sigma_{fg}]\rho\Big] && = 0
\end{aligned}
\tag{3.48}
$$

The sum of each of these terms results in the time-dependent equation for the expectation value of cavity photon number,

$$
\langle\dot{a}\rangle = i\omega\langle a\rangle + i\mathcal{E}e^{-i\omega t} + ig(\vec{r})\langle\sigma_{f3}\rangle - \frac{\kappa}{2}\langle a\rangle. \tag{3.49}
$$

Here we see the only atomic expectation value we need to compute is the coherence between the $|2f_0\rangle$ and $|3\beta_0\rangle$ states. To do this, we build a matrix of all the time dependent expectation values $\langle\dot{\sigma_{ij}}\rangle$ where $i, j \in \{2f_0, 2\beta_0, 3\beta_0\}$. Performing the same calculations as was shown in the photon number case, we can build a differential matrix equation for the atomic states. The result is

$$\begin{pmatrix} -\Gamma_f & i\Omega_W & -ig\langle a^\dagger\rangle & i\Omega_W^* & 0 & 0 & ig\langle a\rangle & 0 & \Gamma_3 \\ -i\Omega_W^* & -\Gamma_f/2 & -i\frac{\Omega_2}{2} & 0 & i\Omega_W^* & 0 & 0 & ig\langle a\rangle & 0 \\ -ig\langle a\rangle & -i\frac{\Omega_2}{2} & -(\Gamma_3+\Gamma_f)/2 & 0 & 0 & i\Omega_W^* & 0 & 0 & ig\langle a\rangle \\ i\Omega_W & 0 & 0 & -\Gamma_f/2 & -i\Omega_W & -ig\langle a^\dagger\rangle & i\frac{\Omega_2}{2} & 0 & 0 \\ 0 & -\Omega_W & 0 & -i\Omega_W^* & 0 & -i\frac{\Omega_2}{2} & 0 & i\frac{\Omega_2}{2} & 0 \\ 0 & 0 & i\Omega_W & -ig\langle a\rangle & -i\frac{\Omega_2}{2} & -\Gamma_3/2 & 0 & 0 & i\frac{\Omega_2}{2} \\ ig\langle a^\dagger\rangle & 0 & 0 & i\frac{\Omega_2}{2} & 0 & 0 & -(\Gamma_3+\Gamma_f)/2 & -i\Omega_W & -ig\langle a^\dagger\rangle \\ 0 & ig\langle a^\dagger\rangle & 0 & 0 & i\frac{\Omega_2}{2} & 0 & -i\Omega_W^* & -\Gamma_3/2 & -i\frac{\Omega_2}{2} \\ 0 & 0 & ig\langle a^\dagger\rangle & 0 & 0 & i\frac{\Omega_2}{2} & -ig\langle a\rangle & -i\frac{\Omega_2}{2} & -\Gamma_3 \end{pmatrix} \begin{pmatrix} \langle\dot\sigma_{ff}\rangle \\ \langle\dot\sigma_{f2}\rangle \\ \langle\dot\sigma_{f3}\rangle \\ \langle\dot\sigma_{2f}\rangle \\ \langle\dot\sigma_{22}\rangle \\ \langle\dot\sigma_{23}\rangle \\ \langle\dot\sigma_{3f}\rangle \\ \langle\dot\sigma_{32}\rangle \\ \langle\dot\sigma_{33}\rangle \end{pmatrix}$$

At this point, we restrict ourselves to the nearly steady-state case, where all time derivatives equal zero, except the population change of the $2\beta_0$ state. We set $\langle\dot\sigma_{22}\rangle = 4\Omega_2^2/\Gamma_3$, the damped Rabi rate of the $|2\beta_0\rangle \rightarrow |3\beta_0\rangle$ transition. Even with these simplifications, it would be daunting to analytically solve this 9x9 matrix equation. However, since we are only interested in extracting $\langle\dot\sigma_{f3}\rangle$, we can use Cramer's rule, which lets us solve directly for one term of the matrix equation through determinants:

$$\langle\sigma_{f3}\rangle = \frac{Det[M^i]}{Det[M]} \tag{3.50}$$

where M is the matrix formed above, and M^i is the same matrix, but with the column vector $(0\ 0\ 0\ 0\ 4\Omega_2^2/\Gamma_\alpha\ 0\ 0\ 0\ 0)^T$ replacing the third column of M. At this point, it's cumbersome to try solving determinants of these 9x9 matrices, despite the many zeroes. Using a symbolic math program (we used Mathematica), the matrices can still be symbolically broken up using an LU decomposition. Then we get that

$$\langle\sigma_{f3}\rangle = \frac{Det[M^i]}{Det[M]} = \frac{Det[L^iU^i]}{Det[LU]} = \frac{Det[U^i]}{Det[U]} = \prod_{k=1}^{9}\frac{U^i_{kk}}{U_{kk}} \tag{3.51}$$

Using the assumption that $\Omega_W \ll 1$ and that $\Gamma_f \gg \Gamma_3$, we can perform these computations to recover an expression for $\langle\sigma_{f3}\rangle$. We get

$$\langle \sigma_{f3} \rangle = \frac{2\Omega_2 \Omega_W}{\Gamma_3 \Gamma_f} + \frac{i\langle a \rangle g \Omega_2^2}{\Gamma_3^2 \Gamma_f}. \tag{3.52}$$

Since $\langle a \rangle g = \Omega_1$, we can recast this density matrix element into the form

$$\langle \sigma_{f3} \rangle = \frac{2\Omega_2 \Omega_W}{\Gamma_3 \Gamma_f} + i\frac{\Omega_1 \Omega_2^2}{\Gamma_3^2 \Gamma_f} e^{i\phi}, \tag{3.53}$$

where the term $e^{i\phi}$ has been added in to account for the relative phase between the one- and two-photon radiation sources. Through the CQED formalism, we have recovered the same matrix element as with the Schrodinger approach.

3.6 Laser Dynamics

Having solved for the coherence between $|3\beta_0\rangle$ and $|2f_0\rangle$ in the form of a density matrix element allows us also calculate an electric susceptibility χ. From that, we can compute an expected laser gain, which is ultimately the signal for this proposed PNC experiment. To calculate χ, we look at two forms of polarization:

$$\begin{aligned} \vec{P} &= \epsilon_0 \chi \vec{E} \\ \vec{P} &= N\langle \vec{\mu} \rangle \end{aligned} \tag{3.54}$$

where ϵ_0 is the permittivity of free space, $\vec{E}$ is the applied laser electric field, N is the volume density of atoms, and $\langle \vec{\mu} \rangle$ is the average dipole moment of each atom. Because the polarization is a real, observable quantity, but it's constituents are not, we can first rewrite and simplify relation

involving $\vec{E}$.

$$\begin{aligned}\vec{P}_{real} &= \frac{1}{2}(\vec{P} + \vec{P}^*) \\ &= \frac{1}{2}(\epsilon_0\chi\vec{E} + \epsilon_0\chi^*\vec{E}^*) \\ &= \frac{\epsilon_0}{2}[(\chi' + i\chi'')(\vec{E}' + i\vec{E}'') + (\chi' - i\chi'')(\vec{E}' - i\vec{E}'')] \\ &= \epsilon_0(\chi'\vec{E}' - \chi''\vec{E}'')\end{aligned} \tag{3.55}$$

where the primes and double-primes indicate the real and imaginary parts, respectively, of each term. To calculate the polarization using the second equation of Eqn. 3.54, we can invoke the general result from the density matrix formalism that states an average observable quantity is equal to the trace of the product of that observable's operator and density matrix, $\langle A\rangle = Tr(\rho A)$. In our case, we want to look at gain from just a "probe" beam between the $|3\beta_0\rangle$ and $|2f_0\rangle$ states, which has a dipole matrix consisting of nearly all zeros. The only nonzero matrix elements are μ_{3f} and μ_{f3}. This results in

$$\vec{P}_{real} = N\langle\mu\rangle = N\ Tr(\rho\mu) = N(\mu_{f3}\rho_{3f} + \mu_{3f}\rho_{f3}) \tag{3.56}$$

Since $\mu_{f3} = \langle 2f_0|q\vec{r}|3\beta_0\rangle = \langle 3\beta_0|q\vec{r}|2f_0\rangle = \mu_{3f}$ and $\rho_{3f} = \rho^*_{f3}$, we can simplify:

$$\begin{aligned}\vec{P}_{real} &= N\mu_{3f}(\rho_{3f} + \rho^*_{3f}) \\ &= N\mu_{3f}(\rho'_{3f} + i\rho''_{3f} + \rho'_{3f} - \rho''_{3f}) \\ &= 2N\mu_{3f}\rho'_{3f}\end{aligned} \tag{3.57}$$

The coherence is proportional to the applied laser field, which contains phase information, so we can write $\rho_{3f} = Ae^{i\phi}$. A is some complex value as well, so we can expand and simplify:

$$\begin{aligned}\rho_{3f} &= Ae^{i\phi} \\ &= (A' + iA'')(cos(\phi) + isin(\phi)) \\ &= A'cos(\phi) - A''sin(\phi) + i(A'sin(\phi) + A''cos(\phi))\end{aligned} \tag{3.58}$$

Now we can pick off the real part, $\rho'_{3f} = A'cos(\phi) - A''sin(\phi)$. Rewriting Eqn. 3.54 after setting $\vec{E}' = \vec{E}_0 cos(\phi)$ and $\vec{E}'' = \vec{E}_0 sin(\phi)$ and then equating final polarization equations:

$$2N\mu_{3f}(A'cos(\phi) - A''sin(\phi)) = \epsilon_0 E_0(\chi'cos(\phi) - \chi''sin(\phi)) \tag{3.59}$$

This equations lets us set coefficients of the sine and cosine terms equal, resulting in expressions for χ' and χ'':

$$\chi' = \frac{2N\mu_{3f}}{\epsilon_0 E_0} Re(\rho_{3f} e^{-i\phi}) \qquad \chi'' = -\frac{2N\mu_{3f}}{\epsilon_0 E_0} Im(\rho_{3f} e^{-i\phi}). \tag{3.60}$$

The single-pass gain through a medium can be described [58] as

$$\Gamma^{(g)} = -\frac{\omega l}{c}\chi'', \tag{3.61}$$

where ω is the radiation frequency and l is the length of the gain medium. Inserting Eqn. 3.39 and Eqn. 3.60 into the gain equation, we have an expression for single-pass gain in terms of Rabi rates and state lifetimes:

$$\Gamma^{(g)} = \frac{n_a}{\Phi}\left(\frac{\Omega_1^2\Omega_2^2}{\gamma_3^2\gamma_f^2} + \frac{2|\Omega_W|\Omega_1\Omega_2}{\gamma_3\gamma_f}\text{cos}\phi\right), \tag{3.62}$$

where Φ is the photon flux associated with Ω_1 and n_a is the density of metastable hydrogen. To simplify notation, let

$$\Gamma_0^{(g)} = \frac{n_a}{\Phi}\left(\frac{\Omega_1^2\Omega_2^2}{\gamma_3^2\gamma_f^2}\right) \quad \text{and} \quad \Gamma_W^{(g)} = \frac{n_a}{\Phi}\left(\frac{2|\Omega_W|\Omega_1\Omega_2}{\gamma_3\gamma_f}\right) \tag{3.63}$$

so that $\Gamma^{(g)} = \Gamma_0^{(g)} + \Gamma_W^{(g)}\cos\phi$. The majority of the gain is induced due to the first term, while a small modulation occurs due to the presence of the weak interaction. Handedness reversals can be conducted by adjusting the relative phase between one- and two- photon sources by π, as is apparent by the $\cos\phi$ term.

The weak gain coefficient can be recast in terms of the larger coefficient, which is varied by adjusting the two-photon power. Doing so, we can write

$$\Gamma_W^{(g)} = 2\sqrt{\frac{n_a\Gamma_0^{(g)}}{\Phi\gamma_f}}|\Omega_W|. \tag{3.64}$$

3.7 Signal-to-Noise

The atomic system flowing through the radiation sources acts as a gain medium in this measurement. First, we analyze a single pass. To calculate the amount of gain produced in a single pass through the atoms of length l, we solve the differential gain equation

$$\frac{d\Phi}{dl} = \Gamma^{(g)}\Phi. \tag{3.65}$$

The result of this equation using the gain expressions define above are

$$\Phi(l) = \Phi(0)e^{\Gamma_0^{(g)}l} + 4\sqrt{\frac{\Phi(0)n_a}{\Gamma_0^{(g)}\gamma_{2f}}}|\Omega_W|\left(e^{\Gamma_0^{(g)}l} - e^{\frac{1}{2}\Gamma_0^{(g)}l}\right)\cos\phi. \tag{3.66}$$

The photon detection rate is simply calculated by multiplying the photon flux by the laser area A and net detection efficiency η. Doing so gives an expression for the number of photons/s, R, as the signal for the measurement. Considering now the actual PNC signal comes from a differential measurement of a measured value and that same value after an inversion, the PNC signal after a

total integration time τ is given by $S = \frac{1}{2}(R_+ - R_-)\tau$. Assuming for now a shot-noise limited signal with noise of $\sqrt{S}$, the signal-to-noise ratio (SNR) is then given by

$$\text{SNR} = \sqrt{\frac{(R_+ - R_-)\tau}{2}}. \tag{3.67}$$

Inserting $R_{+-} = \Phi(l)_{+-}\eta A$ and simplifying, we get a net result for the expected SNR of this single pass PNC measurement:

$$\text{SNR} = 4|\Omega_W|\sqrt{\frac{\eta N_a \tau}{\gamma_{2f}}}\left(\frac{e^{\frac{1}{2}\Gamma_0^{(g)}l} - 1}{\sqrt{\Gamma_0^{(g)}l}}\right). \tag{3.68}$$

Since the value in parentheses in Eqn. 3.68 is monotonically increasing with higher $\Gamma_0^{(g)}l$, it would seem the SNR is unbounded and a larger gain should always improve SNR. However, the analysis performed here ignores saturation effects and is only valid in the case $\Gamma_0^{(g)} \lesssim 1$. However, even with a centimeter-scale interaction region with a high density metastable hydrogen beam at 10^9cm^{-3} (limited by a 30 cm mean-free path, as described in [57]) and weak excitation from $|2\beta_0\rangle$ to $|3\beta_0\rangle$, $\Gamma_0^{(g)}l$ is only ≈ 0.03. In light of this, we now analyze the experiment with the addition of a cavity to enhance the field associated with Ω_{1p}, which effectively increases the interaction length due to the buildup cavity. A ring cavity is considered in order to maintain a well-defined phase relationship between the two-photon radiation and probe radiation. Assuming both the input and output couplers have transmission T and that the only optical loss comes from those mirrors, the relationship between input and output photon flux is then given by the semi-classical approximation

$$\frac{\Phi_{\text{out}}}{\Phi_{\text{in}}} = \frac{1}{(1 - \frac{\Gamma_0^{(g)}l}{2T})^2} \approx \frac{1}{(1-\alpha^{(g)})^2} - \frac{\Gamma_W^{(g)}l}{T}\frac{\cos\phi}{(1-\alpha^{(g)})^3}, \tag{3.69}$$

where $\alpha^{(g)} = \Gamma_0^{(g)}l/(2T)$. The experimental setup in this case resembles an injected laser below threshold with $\alpha^{(g)}$ being a parameter which indicates the proximity to the lasing threshold.

From Eqn. 3.69, we can again calculate the SNR assuming a shot-noise limit and going through the same steps as before. The result is

$$\text{SNR} = 4|\Omega_W|\sqrt{\frac{\eta N_a \tau}{\gamma_{2f}}}\left(\frac{\sqrt{\alpha^{(g)}}}{\sqrt{2}(1-\alpha^{(g)})}\right). \tag{3.70}$$

In this case, the value in parentheses becomes 1 if the lasing parameter $\alpha^{(g)}$ is set to 1/2. However, due to again saturation effects, this analysis is only valid for $\alpha^{(g)} < 1/2$, but $\alpha^{(g)}$, which can be controlled physically by adjusting the the two radiation powers, can approach 1/2.

3.8 Systematics

While having a baseline SNR which shows promise for realizing a PNC experiment is the first major benefit to this scheme, the arguably more important aspects of this proposal are the ways in which systematic effects are characterized and mitigated. The previous attempts at hydrogen PNC measurements were plagued by systematic effects that overshadowed any hint of weak coupling. The largest systematic effects was due to stray static and motional electric fields [47–49]. One of the most beneficial aspects of a laser-based PNC measurement is the ability to localize an interaction region far from any surface, reducing the effects of stray fields from patch or stray charge buildups.

The problem ensuing from stray electric fields comes into the coupling between the $|2\beta_0\rangle$ and $|2f_0\rangle$ states. An electric field in the z-direction of only 5 nV/cm can produce a Rabi frequency $\Omega_{Ez}^{f_0}$ of the same order of magnitude as Ω_W. However, because Ω_W is strictly imaginary, its effects can be differentiated from those of Stark mixing. In fact, a purposefully applied oscillating field can be added to the interaction region while continuously varying the relative phase between Ω_{1p} and Ω_{2p} in order to calibrate the size of Ω_W in a similar method described in [59].

There are three other states that a static field can couple $|2\beta_0\rangle$ to, as shown in Fig. 3.4. It is possible to emulate a PNC signal by Stark mixing to the $|2f_{-1}\rangle$, $|2e_0\rangle$, or the $|2e_1\rangle$ states with a variety of static field directions and laser polarizations. These states are not problematic, however,

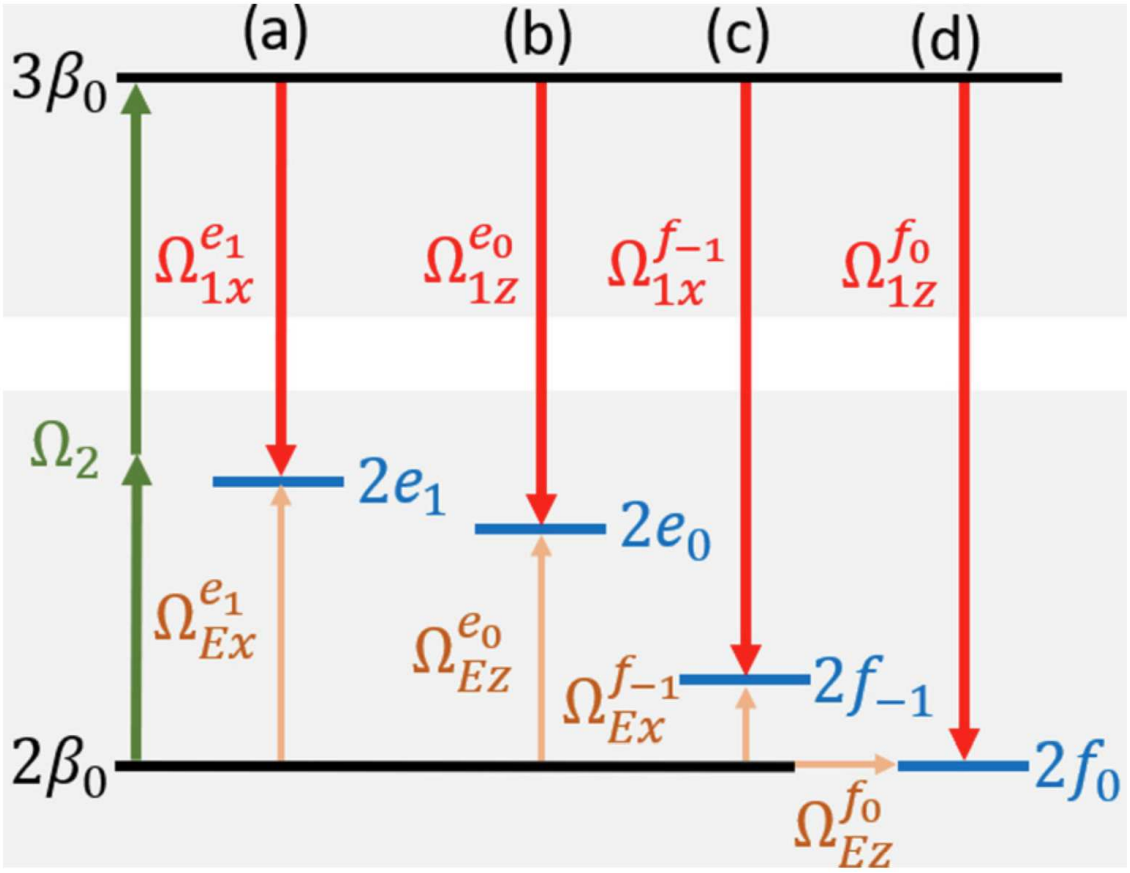

Figure 3.4: Possible transitions due to systematics such as stray electric fields, laser misalignment, and polarization mismatching. (a),(c) Stray electric fields in the x-direction and x-polarized 656 nm light. (b),(d) Stray electric fields in the z-direction and z-polarized 656 nm light.

Table 3.3: Relative photon flux due to stray electric fields compared to that of PNC effects using Eqn. 19. The assumed stray fields are expected upper limits on both the longitudinal and transverse directions. We assume a polarization purity of 10^4 in the $z-$direction. The ratio $\Omega_1^{2P}/\Omega_{1z}^{f0}$ is the ratio of single-photon Rabi rates from the upper $|3\beta_0\rangle$ state to each of the $2P_{1/2}$ states, $2P = \{2e_1, 2e_0, 2f_{-1}, 2f_0\}$. The ratio Ω_E^{2P}/Ω_W compares Rabi rates of Stark mixing due to stray electric fields at the different $2P_{1/2}$ states to the Rabi rate due to weak mixing. The term $\tilde{\alpha}$ describes the relative lasing thresholds of the medium due to weak interaction compared to stray electric field interactions. We note in the last column whether each systematic is in- or out-of-phase with the weak Rabi rate, Ω_w. The leading systematic, caused by $|2f_0\rangle$, is out-of-phase with Ω_w, which further suppresses its effects as discussed further in the text. The a) and c) systematics due to the presence of an x-direction electric field arise from spurious polarization of the 656 nm field, and thus cannot be said to have a defined phase with the weak amplitude. For our calculations, we assume these amplitudes to be in-phase with the weak rate. Therefore, the values listed here represent upper limits but would likely be further suppressed. [1]

	$2P_{1/2}$ sublevel	Stray $\vec{E}$ field	Pol. sup.	$\Omega_1^{2P}/\Omega_{1z}^{f0}$	Ω_E^{2P}/Ω_W	$\Delta\omega/2\pi$ (MHz)	$\tilde{\alpha}^{(g)}$	Φ_E/Φ_W	Relative phase to Ω_w
a)	$2e_1$	30 μV/cm $\hat{x}$	10^4	9.5×10^{-5}	5.7×10^4	1114	1/8	3.0×10^{-3}	und.
b)	$2e_0$	5 nV/cm $\hat{z}$	1	0.034	0.05	1085	1/8	9.8×10^{-6}	0
c)	$2f_{-1}$	30 μV/cm $\hat{x}$	10^4	6.9×10^{-7}	140	30	1/8	1.0×10^{-5}	und.
d)	$2f_0$	5 nV/cm $\hat{z}$	1	1	1	0	1	1	$\pi/2$

due to several factors. First, a large suppression factor $\Omega_1^{2p}/\Omega_{1z}^{f_0}$ exists solely based on the small electric dipole moments between these states and $|2\beta_0\rangle$. Additional suppression enters in by way of off-resonance; these states are 30, 1085, and 1114 MHz detuned, which limits the excitation probability. A large polarization suppression of about 10^4 exists for the $|2e_1\rangle$ and $|2f_{-1}\rangle$ states based on how pure the laser polarization in the $z-$direction can become. Table 3.3 (taken from [1]) of suppression factors is presented to summarize the mitigation levels of each of these PNC-mimicking transitions.

Each of the transitions which mimic the PNC effect is analyzed in the same manner as the PNC effect and a cavity output photon flux is computed due to each of these mixed states. A net comparison of flux Φ_E/Φ_W is shown in Table 3.3, where due to the undetermined relative phase between weak mixing and the $|2e_1\rangle$ and $|2f_{-1}\rangle$ parity conserving channels, these small relative fluxes are likely overestimates. This ratio of fluxes is computed as

$$\Phi_E/\Phi_W \approx \frac{\Omega_1^{2p}}{|\Omega_{1z}^{f0}|}\frac{\Omega_E^{2p}}{|\Omega_W|}\frac{\tilde{\alpha}^{(g)}}{\sqrt{1+(2\Delta\omega/\gamma_{2p})^2}} \tag{3.71}$$

where Ω_1^{2P} is the one-photon Rabi rate between the $|3\beta_0\rangle$ state and respective $2P_{1/2}$ states ($|2e_0\rangle$, $|2e_1\rangle$, $|2f_{-1}\rangle$, $|2f_0\rangle$), Ω_E^{2P} is the Rabi rate due to static electric fields, and $\Delta\omega$ is the frequency detuning of the laser to the corresponding sublevel. The term $\tilde{\alpha}^{(g)} = (1-\alpha_w^{(g)})^3/(1-\alpha_E^{(g)})^3$ is related to the relative lasing thresholds of the gain medium due to the respective weak interaction and to the stray electric fields. In this case we set $\alpha^{(g)} = 1/2$, which implies $\alpha_E^{(g)} \ll \alpha_w^{(g)}$ for $2P_{1/2}$ sublevels a), b), and c). For the values in Table 3.3, we assume a stray electric field amplitude in the $x-$ and $z-$directions of 30 μV/cm and 5 nV/cm, respectively.

3.9 Systematic Effects Mitigation

The experimentally assumed values in Table 3.3 appear to be of extraordinarily small magnitudes at first glance. In this section, a justification is shown for these fields and a demonstration of how to maintain active stray field mitigation is given.

Consider rotating the polarization of the 656 nm field by 90° from the PNC measurement. This would greatly increase the mixing to the $|2e_1\rangle$ state and would allow a sensitive electric field detection down to about 30 μV/cm in a 1 s integration time. Other experiments have also shown μV/cm-scale electric field detection; see [60] for an example using krypton atoms. By introducing additional electric field plates to the system, a cancellation field can be introduced once a precise determination is made and the polarization rotated back for the PNC measurements, as was done similarly in [42].

This same polarization rotation distinction can also be used for another potential problematic systematic effect. Namely, a motional electric field will be present if the atomic beam is not exactly colinear with the applied magnetic field. This is one benefit to using a cold atomic beam with low divergence [57], but again this effect can be measured and corrected.

To justify such a small stray longitudinal field of 5 nV/cm, we discuss a possible measurement sequence which can be used to actively minimize any stray field and continually mitigate a temporally drifting field. A relatively large (1 μV/cm) electric field can be applied in the z-direction while continuously ramping the phase between the two radiation fields. After reversing the direc-

tion of the applied field, the difference in these two interference signals can determine an amplitude of additional stray field present, which can then be canceled out with a small zeroing field before the actual PNC signal is measured [1]. One can see that this method can actively combat any short- and long-term temporal field drifts in a stray field, while faster fluctuations will simply average out over the length of total integration time.

As a demonstration of this field-zeroing process, we calculate the photon flux exiting our cavity when the atomic beam is subjected to a time-varying stray electric field within the interaction region. Following the Schrodinger analysis above, with the addition of an electric field in the z-direction, we get out a gain term for the electric field $\Gamma_E^{(g)}$. Keeping in mind the Stark mixing term is real while the weak mixing is completely imaginary, the total flux from the cavity has the form

$$\Phi_{\text{out}} = \Phi_{\text{in}} \left[\frac{1}{(1-\alpha)^2} - \frac{l}{T(1-\alpha)^3} \left(\Gamma_W^{(g)} \text{cos}\phi + \Gamma_E^{(g)} \text{sin}\phi \right) \right]. \tag{3.72}$$

Here, $\Gamma_E^{(g)}$ is the same as the weak gain signal, Eqn. 3.64, with the substitution $|\Omega_W| \rightarrow \Omega_E$. With complete generality in mind, we generate a random electric field with spectral composition $1/f^2$. The measurement cycle is conducted in three steps, two measurements with an applied E_z field followed by a PNC measurement with a zeroing field applied. A first measurement is collected by integrating the 656 nm photon flux while applying a 1 μV/cm magnitude field and ramping the phase between the two radiation sources from 0 to 2π over 1/2 s. From this data, we can extract $\Gamma_E^{(g)}$ directly by integrating the signal multiplied by sinϕ over the integration period, in a manner similar to the evaluation of Fourier components. Doing so ignores weak effects due to the cosine term. Performing the same measurement after reversing the sign of the applied electric field, we can use these two values to extract the magnitude and direction of any stray electric field. Having determined the stray field, we apply a small zeroing field and then conduct a PNC measurement over a 1 s integration time. We can now multiply by cosϕ to extract the weak gain term and further mitigate imperfect stray field zeroing.

Figure 3.5 shows a typical simulation of several measurement cycles using this electric field zeroing method. Specifically, Fig. 3.5(a) shows a randomly generated, temporally-drifting electric

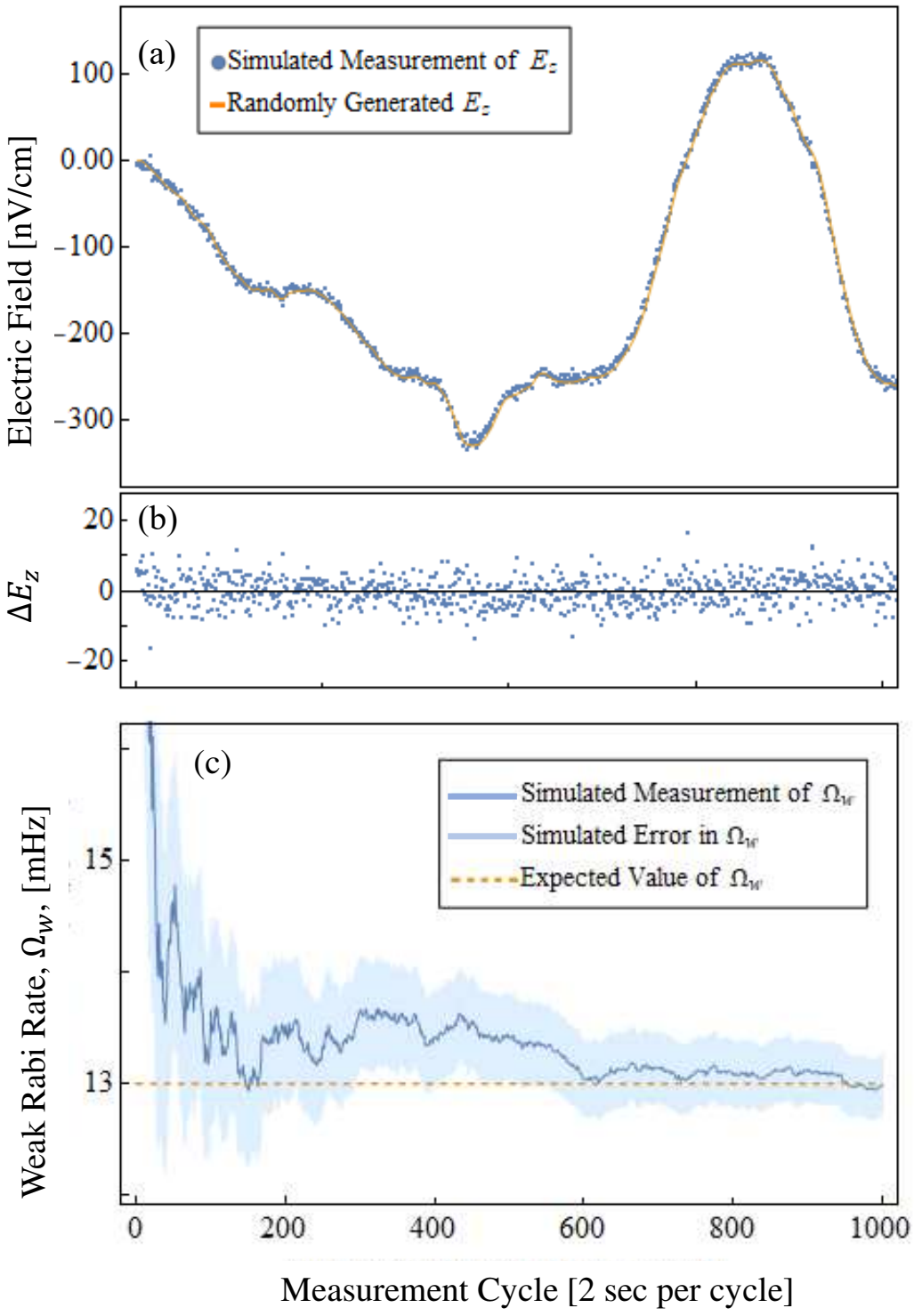

Figure 3.5: Simulation results of E_z field zeroing process. (a) Randomly generated E_z field with $1/f^2$ spectral composition along with simulated measurements at each 2 second measurement cycles. (b) The difference between the generated and measured electric field. (c) Simulated measurement of the weak Rabi rate, showing the expected increase in accuracy after averaging over multiple data collection cycles.

field along with the measured values using the aforementioned method. The difference between measured and simulated fields is shown in Fig. 3.5(b), demonstrating strong agreement. Note the determination of the field is at the 5 nV/cm level, as was assumed in the values determining Table 3.3. As a comparison, [60] measured an electric field of 10 μV/cm over several hours, which implies an electric field drift on the order of 1 nV/cm/s. This value was used as an upper limit in these simulations. The net systematic suppression is apparent looking at Fig. 3.5(c). This figure shows the extracted weak Rabi rate after each measurement cycle, gradually approaching the assumed expected value, reducing the uncertainty at a rate of $\sqrt{\tau}$ total integration time. This simulation reproduced similar results for a wide range of stray field profiles, all tending towards the expected weak Rabi rate for similar time scales.

3.10 Practical SNR Considerations

As can be seen from the expression in Eqn. 3.70, there are few approaches to take for increasing the SNR of a weak measurement since $|\Omega_W|$ and γ_{2f} are fixed physical parameters, η will always be less than 1 and $\alpha^{(g)} \approx 1/2$. The remaining terms are N_a and τ. Like most other spectroscopic experiments, the SNR will increase at a rate of $\sqrt{\tau}$. The one factor that allows some optimization is the atomic beam density N_a. The upper limit on this value, however, is outlined in [57]; collision-induced decay out of the $|2\beta_0\rangle$ state limits the density to about 3×10^9 atoms/cm^3, assuming a mean-free path of about 30 cm. At this density, a SNR $\approx 0.1\sqrt{\tau}$ is possible, allowing for a 10% measurement of Ω_W to be made with a few hours of integration time.

3.11 Auxiliary Experiments

The focus of the presented work has been on measuring the weak interaction at the $|2\beta_0\rangle$ and $|2f_0\rangle$ level crossing and extracting the linear combination of $C_{1p} + 1.1C_{2p}$. The generality of this experimental design allows a second measurement at the $|2\beta_0\rangle$ and $|2e_0\rangle$ level crossing at 550 G, which strictly extracts the C_{2p} weak coupling constant. In conjunction with the first measurement, both electron-proton weak neutral coupling constants can be extracted.

Additionally, the same experiment with only slight apparatus modifications could be conducted on deuterium in order to measure the C_{1n} and C_{2n} electron-neutron weak neutral coupling constants, giving a near-complete description of electroweak interactions between electrons and nucleons [1, 57].

Chapter 4

Conclusions

While initially (and naively) thinking the $2S_{1/2}$ hyperfine measurement would be a straightforward experiment since our group has several technological advantages over the others who had previously measured this interval, we proved to have underestimated the subtleties involved. We are benefited by having control over our atomic beam velocities, by the development of a 243 nm source to selectively excite the $F = 0$ metastable state, and by the vast RF resources which have been refined over decades. However, several trial-and-error sorts of steps were taken that demonstrated the nuances in performing such a high-precision RF measurement. For example, the initial coil design requiring a relatively large current induced an AC electric field through Faraday's law and was responsible for a velocity-dependent phase shift – it took weeks or months to resolve that problem with several iterations of coil design. Another setback in this experiment involved the solenoid we built to generate a magnetic field; initially wrapping a coil around a glass tube on the inside of our RF coils resulted in mistakenly creating a transformer that quenched all of our atoms. This problem was resolved by spacing the coils further apart and making them much larger than the RF coils.

With largest problems behind us now (hopefully), we are left with collecting data and performing systematic characterizations. Statistically, we have the signal-to-noise to determine the line center to about 1 Hz after only 10 minutes of data collection. However, systematic effects such as determining and extrapolating the magnetic field will take several measurements. RF-power-related systematics will have to be measured by varying and extrapolating the power down to zero. Pressure shifts within the atomic beam as well as the vacuum chamber will be determined, though these not currently predicted to pose any significant shifts. These measurements and characterizations are anticipated to be finished within a few months from the time of this writing.

Similar to the hyperfine measurement, our proposed parity violation measurement had similar levels of major roadblocks. Since each of the previous measurements and including the recently

proposed measurement by Dunford and Holt [57] had used RF transitions as their parity conserving channel, that was our starting point in designing an experiment. We designed measurements which takes advantage of technological developments in RF, such as ideas utilizing phased arrays or microwave ring cavities. Each of these designs, though, still had systematic effects which were difficult to account for due to the large interaction regions. Once we decided to explore a laser-based measurement, again several candidate methods were explored and systematic effects seemed to still swamp the desired signal. For example, we considered a parity conserving channel through the intermediate ground state by 121 nm and 243 nm radiation, but the background due to scatter from the high amount of 243 nm power would have drowned the signal.

Having found a promising path towards parity violation in hydrogen, it would be extremely satisfying to see this experiment come to fruition one day and produce meaningful results. However, the experimental prowess, expertise, and precision required would likely involve a collaboration of multiple specialized groups.

Hydrogen has been paramount in the study of physics and this simple atom continues to unveil new details as precision measurements improve. The work discussed in this thesis is but another stepping stone added to the mountain of knowledge that has been acquired before. However, a vast potential impact is possible from continued work in either chapter. The Zemach radius measurement and QED test coming from the $2S$ hyperfine interval measurement could discover beyond-Standard-Model physics and even hint at the axion influences. The parity violating weak interaction has never been measured at such low momentum transfer, and the proposed hydrogen experiment has the real possibility of probing the dark sector in energy regions untested at this time.

Additionally, hydrogen spectra can be compared to its antimatter counterpart, antihydrogen, as additional symmetry tests within the Standard Model. Work was performed on this front through a CSU collaboration with ATRAP; see Appendix A for details.

Bibliography

[1] C. Rasor and D. C. Yost. "Laser-based measurement of parity violation in hydrogen." *Phys. Rev. A*, **102**, 032801 (2020).

[2] C. Bouchiat and C. A. Piketty. "Parity violation in atomic cesium and alternatives to the standard model of electroweak interactions." *Phys. Lett.*, **128B**, 73 (1983).

[3] G. Gabrielse, S. E. Fayer, T. G. Meyers, and X. Fan. "Towards an Improved Test of the Standard Model's Most Precise Prediction." *Atoms*, **7**, 45 (2019).

[4] A. D. Brandt, S. F. Cooper, C. Rasor, Z. Burkley, and D. C. Yost. "Measurement of the $2S_{1/2} - 8D_{5/2}$ Transition in Hydrogen." *Phys. Rev. Lett*, **128**, 023001 (2022).

[5] A. C. Zemach. "Proton Structure and the Hyperfine Shift in Hydrogen." *Phys. Rev.*, **104**, 6 (1956).

[6] A. Dupays, A. Beswick, B. Lepetit, C. Rizzo, and D. Bakalov. "Proton Zemach radius from measurements of the hyperfine splitting of hydrogen and muonic hydrogen." *Phys. Rev. A*, **68**, 052503 (2003).

[7] S. Kanda *et al.* "Measurement of the proton Zemach radius from the hyperfine splitting in muonic hydrogen atom." *J. Phys. Conf. Ser*, **1138**, 012009 (2018).

[8] A. V. Volotka, V. M. Shabaev, G. Plunien, and G. Soff. "Zemach and magnetic radius of the proton from the hyperfine splitting in hydrogen." *Eur. Phys. J. D*, **33**, 23 (2005).

[9] M. Sternheim. "State-Dependent Mass Corrections to Hyperfine Structure in Hydrogenic Atoms." *Phys. Rev.*, **130**, 211 (1963).

[10] M. I. Eides, H. Grotch, and V. Shelyuto. "Theory of light hydrogenlike atoms." *Phys. Rep.*, **342**, 63 (2001).

[11] S. G. Karshenboim and V. G. Ivanov. "Hyperfine structure of the ground and first excited states in light hydrogen-like atoms and high-precision tests of QED." *Euro. Phys. J. D*, **19**, 13 (2002).

[12] S. G. Karshenboim. "Hyperfine structure interval of the 2s state of hydrogenlike atoms and a constraint on a pseudovector boson with mass below 1 keV/c^2." *Euro. Phys. J. D*, **19**, 13 (2002).

[13] F. Wilczek. "Two applications of axion electrodynamics." *Phys. Rev. Lett.*, **58**, 1799 (1987).

[14] K. Tullney *et al.* "Constraints on Spin-Dependent Short-Range Interaction Between Nucleons." *Phys. Rev. Lett.*, **111**, 100801 (2013).

[15] D. J. Wineland, J. J. Bollinger, D. J. Heinzen, W. M. Itano, and M. G. Raizen. "Search for anomalous spin-dependent forces using stored-ion spectroscopy." *Phys. Rev. Lett.*, **67**, 1735 (1991).

[16] M. P. Ledbetter, M. V. Romalis, and D. F. J. Kimball. "Constraints on Short-Range Spin-Dependent Interactions from Scalar Spin-Spin Coupling in Deuterated Molecular Hydrogen." *Phys. Rev. Lett.*, **110**, 040402 (2013).

[17] L. Essen, R. W. Donaldson, M. J. Bangham, and E. G. Hope. "Frequency of the Hydrogen Maser." *Nature*, **229**, 110 (1971).

[18] N. Kolachevsky, A. Matveev, J. Alnis, S. G. Karshenboim, and T. W. Hansch. "Measurement of the 2S Hyperfine Interval in Atomic Hydrogen." *Phys. Rev. Lett.*, **102**, 213002 (2009).

[19] J. W. Heberle, H. A. Reich, and P. Kusch. "Hyperfine Structure of the Metastable Hydrogen Atom." *Phys. Rev.*, **101**, 612 (1956).

[20] N. E. Rothery and E. A. Hessels. "Measurement of the 2S atomic hydrogen hyperfine interval." *Phys. Rev. A*, **61**, 044501 (2000).

[21] N. Kolachevsky, M. Fischer, S. G. Karshenboim, and T. W. Hansch. "High-Precision Optical Measurement of the 2S hyperfine Interval in Atomic Hydrogen." *Phys. Rev. Lett.*, **92**, 033002 (2004).

[22] S. F. Cooper, A. D. Brandt, C. Rasor, Z. Burkley, and D. C. Yost. "Cryogenic atomic hydrogen beam apparatus with velocity characterization." *Rev. Sci. Instrum.*, **91**, 013201 (2019).

[23] J. T. M. Walraven and I. F. Silvera. "Helium-temperature beam source of atomic hydrogen." *Rev. Sci. Instrum.*, **53**, 1167 (1982).

[24] P. Elleaume, O. Chubar, and J. Chavanne. "Computing 3D magnetic fields from insertion devices." *Proc. IEEE Accel. Conf.*, **3** (1998).

[25] F. Roser, C. Jauregui, J. Limpert, and A. Tunnermann. "94 W 980 nm high brightness Yb-doped fiber laser." *Opt. Express*, **16**, 17310 (2008).

[26] Z. Burkley, C. Rasor, S. F. Cooper, A. D. Brandt, and D. C. Yost. "Yb-fiber amplifier at 972 nm with frequency quadrupling to 243.1 nm." *Appl. Phys. B*, **123**, 5 (2017).

[27] Z. Burkley. "High-Power Deep-UV Laser for Improved and Novel Experiments on Hydrogen." PhD dissertation, Colorado State University, Department of Physics (2019).

[28] S. F. Cooper, Z. Burkley, A. D. Brandt, C. Rasor, and D. C. Yost. "Cavity-enhanced deep ultraviolet laser for two-photon cooling of atomic hydrogen." *Opt. Lett.*, **43**, 1375 (2018).

[29] A. D. Brandt. "A New Measurement of the $2S_{1/2} - 8D_{5/2}$ Transition in Atomic Hydrogen." PhD dissertation, Colorado State University, Department of Physics (2021).

[30] G. W. F. Drake. *The Spectrum of Atomic Hydrogen: Advances*, chap. Theory of Transitions and the electroweak interaction. World Scientific, Singapore (1988).

[31] P. L. Anthony *et al.* "Precision Measurement of the Weak Mixing Angle in Moller Scattering." *Phys. Rev. Lett.*, **95**, 081601 (2005).

[32] D. Androic *et al.* "Precision measurement of the weak charge of the proton." *Nature*, **557**, 207 (2018).

[33] K. Kumar, S. Mantry, W. Marciano, and P. Sounder. "Low-Energy Measurements of the Weak Mixing Angle." *Annu. Rev. Nucl. Part. Sci.*, **63**, 237 (2013).

[34] S. Collaboration. "High-Precision Measurement of the Left-Right Z Boson Cross-Section Asymmetry." *Phys. Rev. Lett.*, **84**, 5945 (2000).

[35] ALEPH Collab *et al.* "Precision Electroweak Measurements and Constrains on the Standard Model." *arXiv1012.2367hep-ex*, **47**, 777 (2010).

[36] SLAC E158 Collaboration. "Precision Measurement of the Weak Mixing Angle in Moller Scattering." *Phys. Rev. Lett.*, **95**, 081601 (2005).

[37] G. Zeller *et al.* "Precise Determination of Electroweak Parameters in Neutrino-Nucleon Scattering." *Phys. Rev. Lett.*, **88**, 091802 (2002).

[38] M. Macpherson *et al.* "Precise measurement of parity nonconserving optical rotation at 876 nm in atomic bismuth." *Phys. Rev. Lett.*, **67**, 2784 (1991).

[39] S. J. Phipp, N. H. Edwards, P. E. G. Baird, and S. Nakayama. "A measurement of parity non-conserving optical rotation in atomic lead." *J. Phys. B*, **29**, 1861 (1996).

[40] P. A. Vetter *et al.* "Precise Test of Electroweak Theory from a New Measurement of Parity Nonconservation in Atomic Thallium." *Phys. Rev. Lett.*, **74**, 2658 (1995).

[41] K. Tsigutkin *et al.* "Observation of a Large Atomic Parity Violation in Ytterbium." *Phys. Rev. Lett.*, **103**, 071601 (2009).

[42] C. S. W. et al. "Measurement of Parity Nonconservation and an Anapole Moment in Cesium." *Science*, **275**, 1759 (1997).

[43] E. Gomez *et al.* "Measurement method for the nuclear anapole moment of laser-trapped alkali-metals." *Phys. Rev. A*, **75**, 033418 (2007).

[44] M. N. Portela *et al.* "Towards a precise measurement of atomic parity violation in a single Ra+ ion." *Hyperfine Interact*, **214**, 157 (2013).

[45] H. Davoudias, H.-S. Lee, and W. J. Marciano. "Low Q2 weak mixing angle measurements and rare Higgs decays." *Phys. Rev. D*, **92**, 055005 (2015).

[46] G. Aad *et al.* "Search for new light gauge bosons in Higgs boson decays to four-lepton final states in pp collisions at $\sqrt{s} = 8$ TeV with ATLAS detector at the LHC." *Phys. Rev. D*, **92**, 092001 (2015).

[47] C. C. W. Fehrenbach. "An experimental limit on parity mixing in atomic hydrogen." PhD dissertation, University of Michigan, Department of Physics (1993).

[48] M. Z. Iqbal. "A Search for Parity-Nonconservation in the Hydrogen Atom." PhD dissertation, University of Washington, Department of Physics (1983).

[49] J. M. Hettema. "Upper Bound on Parity Nonconservation in 2S Hydrogen." PhD dissertation, Yale University, Department of Physics (1990).

[50] L. P. Levy and W. L. Williams. "Parity nonconservation in the hydrogen atom. III." *Phys. Rev. A*, **30**, 220 (1984).

[51] R. W. Dunford, R. R. Lewis, and W. L. Williams. "Parity nonconservation in the hydrogen atom. II." *Phys. Rev. A*, **18**, 2421 (1978).

[52] W. E. L. Jr. "Fine Structure of the Hydrogen Atom III." *Phys. Rev.*, **79**, 549 (1952).

[53] B. Roberts, V. Dzuba, and V. Flambaum. "Parity and Time- Reversal Violation in Atomic Systems." *Annu. Rev. Nucl. Part. Sci.*, **65**, 63 (2015).

[54] A. E. Kramida. "A critical compilation of experimental data on spectral lines and energy levels of hydrogen, deuterium, and tritium." *Atomic Data and Nuclear Data Tables*, **96**, 586 (2010).

[55] M. Haas. "Two-photon excitation dynamics in bound two-body Coulomb systems including ac Startk shift and ionization." *Phys. Rev. A*, **73**, 052501 (2006).

[56] R. A. Swainson and G. W. F. Drake. "A unified treatment of the non-relativistic and relativistic hydrogen atom II: the Green functions." *J. Phys. A: Math Gen.*, **24**, 95 (1991).

[57] R. Dunford and R. Holt. "Parity Violation in Hydrogen Revisited." *J. Phys. G: Nucl. Part. Phys.*, **34**, 2099 (2007).

[58] J. Verdeyen. *Laser Electronics*, chap. 13, 593. Printice Hall, Inc, New Jersey, 3 edn. (1995).

[59] D. Antypas and D. S. Elliott. "Measurement of a weak transition moment using two-pathway coherent control." *Phys. Rev. A*, **87**, 042505 (2013).

[60] A. Osterwalder and F. Merkt. "Using High Rydberg States as Electric Field Sensors." *Phys. Rev. Lett.*, **82**, 1831 (1999).

[61] R. Abegg *et al.* "Charge-symmetry breaking in np elastic scattering at 477 MeVF." *Phys. Rev. D*, **39**, 2464 (1989).

[62] S. E. Vigdor *et al.* "Charge symmetry breaking in n->-p-> scattering at 183 MeV." *Phys. Rev. C*, **46**, 410 (1992).

[63] C. S. Wu, E. Ambler, R. W. Hayward, D. D. Hoppes, and R. P. Hudson. "Experimental test of parity conservation in beta decay." *Phys. Rev.*, **105**, 1413 (1957).

[64] J. P. Lees *et al.* "Observation of Time-Reversal Violation in the B^0 Meson System." *Phys. Rev. Lett.*, **109**, 211801 (2012).

[65] J. H. Christenson. "Evidence for the 2π Decay of the K_2^0 Meson." *Phys. Rev. Lett.*, **13**, 138 (1964).

[66] G. Luders. "On the equivalence of invariance under time reversal and under particle-antiparticle conjugation for relativistic field theories." *Dan. Mat. Fys. Medd.*, **28**, 1 (1954).

[67] R. Lehnert. "CPT Symmetry and Its Violation." *Symmetry*, **8**, 114 (2016).

[68] G. M. Shore. "Strong equivalence, Lorentz and CPT violation, anti-hydrogen spectroscopy and gamma-ray burst polarimetry." *Nucl. Phys. B*, **717**, 86 (2005).

[69] J. M. Michan, G. Polovy, K. W. Madison, M. C. Fujiwara, and T. Momose. "Narrowband solid state vuv coherent source for laser cooling antihydrogen." *Hyperfine Interact*, **235**, 29 (2015).

[70] I. D. Setija, H. G. C. Werij, O. J. Luiten, M. W. Reynolds, T. W. Hijmans, and J. T. M. Walraven. "Optical cooling of atomic hydrogen in a magnetic trap." *Phys. Rev. Lett.*, **70**, 2257 (1993).

[71] K. S. E. Eikema, J. Walz, and T. W. Hansch. "Continuous Coherent Lyman-α Excitation of Atomic Hydrogen." *Phys. Rev. Lett.*, **86**, 5679 (2001).

[72] L. Cabaret, C. Delsart, and C. Blondel. "High resolution spectroscopy of the hydrogen Lyman-α line stark structure using a vuv single mode pulsed laser system." *Opt. Commun.*, **61**, 116 (1987).

[73] P. W. Milonni and J. H. Eberly. *Laser Physics*, chap. 10. John Wiley and Sons (2010).

[74] R. Hilbig and R. Wallenstein. "Enhanced production of tunable VUV radiation by phase-matched frequency tripling in krypton and xenon." *IEEE J. Quantum Electron.*, **17**, 1566 (1981).

Appendix A

CPT Symmetry Test in Anti-Hydrogen

A.1 CPT Theorem

The Standard Model of Particle physics classifies all known elementary particles, which are subdivided into matter fermions (quarks and leptons) and force mediating bosons. For every fermion $|\phi\rangle$, there exists a corresponding antimatter equivalent $|\bar{\phi}\rangle$whose charge is reversed. The charge conjugation operator C simply inverts the sign of charge for each particle it acts upon, or equivalently converts matter to antimatter and vice-versa, $C|\phi\rangle = |\bar{\phi}\rangle$. Supposing an experiment is performed using matter, charge conjugation symmetry states that the same experiment with anti-matter will yield the same result. While once thought to have been a universal symmetry, multiple groups have observed charge symmetry breaking (CSB) [61, 62].

Parity is the comparison of a state with given spatial coordinates $|\phi(\vec{r})\rangle$ to a corresponding state with all coordinates being reversed $|\phi(-\vec{r})\rangle$. Parity is said to be conserved if a measurement in both coordinate systems are consistent. Parity was also thought to have been a universal symmetry until the late 1950s [63] – since then, parity violation has been the focus of a number of studies [38–42].

Time reversal involves inverting all signs on time and time-dependent terms such as momentum and angular momentum. Time symmetry is maintained if both forward and backward time experiments yield the same results. The first confirmed direct measurement of time symmetry violation occurred in 2012 at SLAC through the BaBar collaboration [64].

Each of these symmetries individually was once thought to be a universal law. However, each has now been broken in multiple instances. In most cases, if a single symmetry, charge C, parity P, or time T is broken, a second symmetry can be flipped to once again recover the initial results and thus conserve total symmetry. Due to this observation, it had also been thought that combinations CP, CT, and PT would be considered universal symmetries. However, in 1964, CP violation was observed in neutral kaons [65], shattering the idea of these combined symmetries.

Another approach to find universal symmetry is the product all of three terms, CPT. In fact, a mathematical proof in the Hamiltonian framework under the assumption of Lorentz invariance was given in 1954 [66]. To-date, this symmetry has been upheld and no violation of CPT has been observed. If, however, CPT is shown to be violated, that will be clear evidence of BSM physics and revisions to the general framework will then be required. Several Standard Model Extensions (SME) already exist including various string theories and nontrivial spacetime topology with modified Minkowski space [67].

One method to stringently test CPT invariance is to juxtapose the $1S-2S$ transition frequency of hydrogen with that of antihydrogen. The CPT theorem implies that these two frequencies should be exactly identical, and thus any discrepancy between them would be evidence of CPT violation. If Dirac's equation is modified to allow for Lorentz violation, specific CPT violating coupling terms can be introduced and a determination of these coupling strengths can be made [68]. The primary goal of the ATRAP collaboration was to generate and trap antihydrogen atoms and perform 1S-2S spectroscopy to search for any violation of CPT.

One challenging aspect of this experiment is performing spectroscopy on a very small number of antihydrogen atoms; generating antimatter bound states is extremely difficult and few atoms (5-100) are able to be created and trapped at one time. Due to the magnetic trapping of these atoms, large Zeeman shifts would severely limit the precision of the spectroscopy. To combat this effect, laser cooling would be implemented to drive the atoms closer to the center of a Penning trap, thus reducing the average Zeeman shift and increasing precision. Colorado State University joined the ATRAP collaboration in 2015 to build a laser cooling system for antihydrogen.

A.2 Lyman-α Radiation Source

Lyman-α radiation is notoriously difficult to produce with successful groups creating systems which generate 20-100 nanowatts of average power [69–72]. Due to the small nonlinear frequency conversion coefficients, pulsed systems have been able to produce higher average power than continuous-wave (cw) systems – CSU decided to pursue a pulsed approach for this reason.

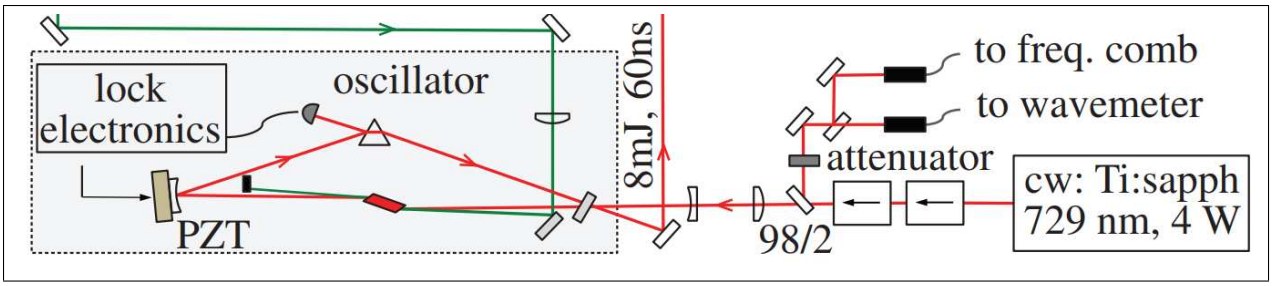

Figure A.1: Schematic of the 729 nm oscillator.

The system begins with a commercial M-squared titanium-sapphire (Ti:sapphire) laser tuned to 729 nm and frequency locked to a Menlo frequency comb. To generate as much power as possible, the 729 nm light is amplified in a multipass Ti:sapphire amplifier crystal. Following amplification, two frequency multiplying stages convert the 729 nm light to Lyman-α – frequency doubling is performed with a lithium triborate (LBO) crystal and then frequency tripling occurs in a phase-matched krypton-argon (Kr-Ar) gas cell. The following sections detail this process.

A.2.1 Oscillator

As shown in Fig. A.2, the oscillator is composed of an 80% output coupler, a 3 m radius-of-curvature (ROC) concave mirror, and a dispersive prism to allow for coarse frequency selectivity. A 2 cm long, Brewster-cut Ti:sapphire crystal within the cavity provides means to generate pulses of 729 nm light when pumped. To provide fine frequency control, the oscillator is injected locked with 100 mW of cw power from a commercial Ti:sapphire laser system.

Power from the Ti:sapphire system passes through two Faraday isolators followed by a 98/2 beam splitter. The lower power branch is used to stabilize the Ti:sapphire system to a Menlo frequency comb, while the majority of the power is used to injection lock the oscillator. In order to lock the oscillator, the curved mirror is mounted on a piezoelectric transducer (PZT), which is dithered at 200 kHz and a small amount of reflected light from the prism is detected and demodulated or produce a resonance error signal. The error signal is processed through a loop filter and then fed back onto the PZT to maintain a cavity resonance. The same curved mirror is also mounted onto a translation stage fitted with a stacked PZT for long-term cavity length corrections.

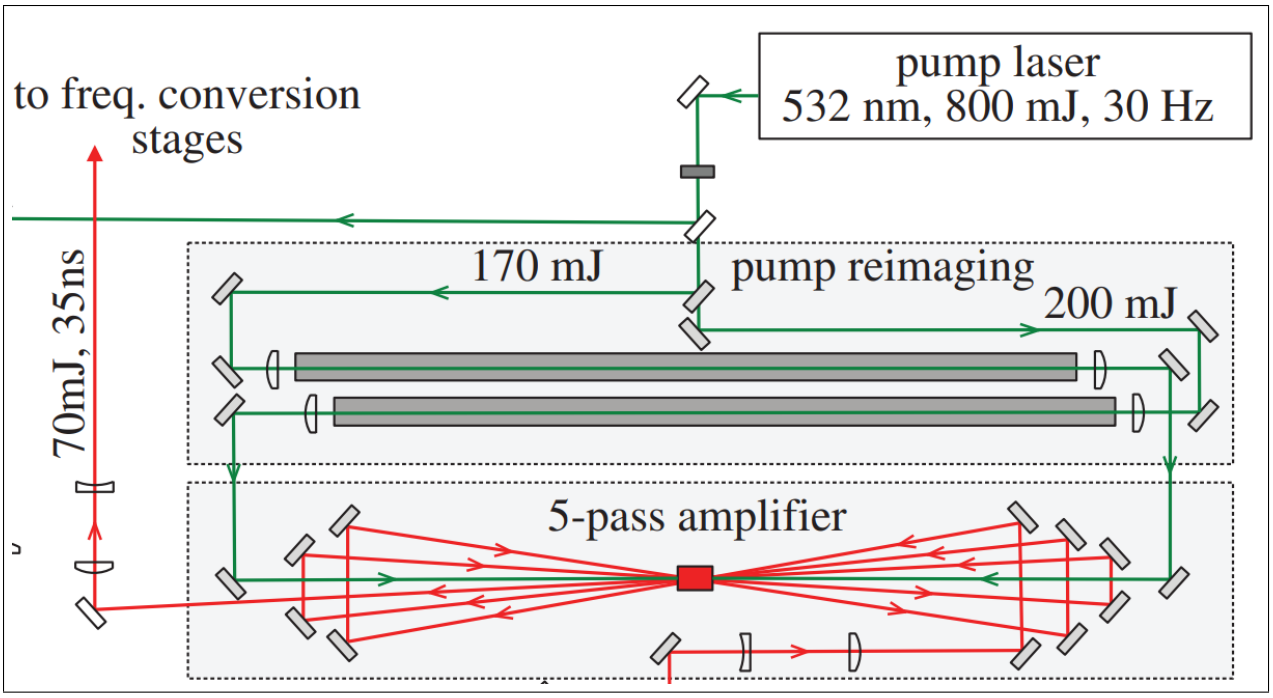

Figure A.2: Schematic of the 729 nm amplifier.

To generate high intensity pulses, the intracavity Ti:sapphire crystal is pumped with by a 532 nm Nd:YAG laser at 10 ns pulse length and 30 mJ per pulse of energy at a repetition rate of 30 Hz. To pump the crystal without causing damage, the Nd:YAG is relay-imaged and sized down from the laser output onto the crystal, which absorbs about about 94% of the pulse energy. Much longer pulses at 729 nm are then generated due to the long lifetime (3.2 μs) of Ti:sapphire – multiple trips around the cavity continue to extract available gain after the crystal is pumped, temporally elongating the output pulse. The typical output of the oscillator is about 8 mJ per pulse.

A.2.2 Amplifier

For harmonic generation to be effective, high intensities are required. The 8 mJ output pulses from the oscillator must first be amplified before they can be used for frequency conversion. Amplification is achieved by multipassing a 15 mm long Ti:sapphire crystal being pumped by 200 mJ of 532 nm energy from each side. To prevent damage to the crystal, relay-imaging was once again done to produce a spatially uniform, flattop beam profile. However, sending 200 mJ through a tight focus would cause a dielectric breakdown of air and distort the relayed image. Vacuum tubes with

windows were constructed to prevent this breakdown by allowing the beam to focus through rough vacuum pressure.

Different numbers of passes were attempted with the amplifier, ranging from a 3-pass up to the largest of an 8-pass. A variety of factors affected the final value of a 5-pass. More passes would typically allow for a more complete gain extraction, but would require pumping the crystal with more energy per pulse. Higher pump powers leads to more thermal lensing when the crystal heats up, so we mount the crystal in a water-cooled copper holder. However, the risk of damaging optics increases with higher powers. For the sake of system longevity, we reduced the pump power to about 200 mJ per side and settled on 5 passes. The amplifier reliably produces 70 mJ pulses with records above 120 mJ. An image of the final setup is shown in Fig. A.3.

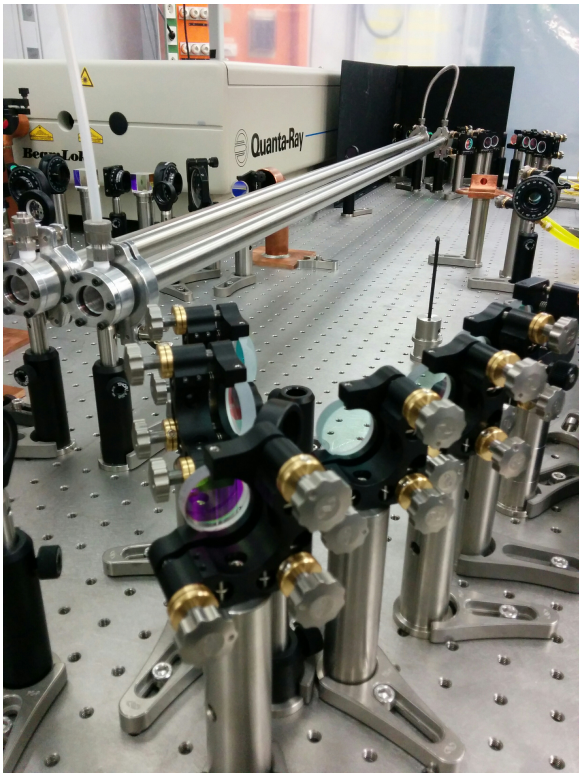

Figure A.3: Image of the 729 nm Ti:Sapp amplifier. The two steel tubes are maintained at rough vacuum pressures in order to perform pump reimaging; the 300 mJ pump pulses passing through a focus causes dielectric breakdown in the air and negates any effective reimaging.

A.2.3 Frequency Conversion

When subjected to an electric field, atoms comprising a local volume can be described by a polarizability – the degree in which a material obtains an electric dipole moment. Polarizability $P(t)$ is related to the electric field $E(t)$ by $P(t) = \epsilon_0 \chi E(t)$, where ϵ_0 is the permittivity of free space. Expanding the polarizability as a power series in field strength, we can write

$$P(t) = \epsilon_0 \left(\chi^{(1)} E(t) + \chi^{(2)} E(t)^2 + \chi^{(3)} E(t)^3 + \cdots \right), \tag{A.1}$$

where $\chi^{(n)}$ is the optical susceptibility. For a given material, the effect of inducing nonlinear polarizabilities is to produce radiation of integer multiples from the fundamental field.

Frequency Doubling

If we consider second-order polarizability $P^{(2)}(t) = \epsilon_0 \chi^{(2)} E(t)^2$ with a driving field $E(t) = E_0 e^{-i\omega t} + E_0^* e^{i\omega t}$, then we get terms corresponding to double the fundamental frequency:

$$P^{(2)}(t) = \epsilon_0 \chi^{(2)} \left(2E_0 E_0^* + E_0^2 e^{-i2\omega t} + E_0^{*2} e^{i2\omega t} \right). \tag{A.2}$$

By applying the scalar wave equation

$$\nabla^2 E - \frac{1}{c^2} \frac{\partial^2 E}{\partial t^2} = \mu_0 \frac{\partial^2 P}{\partial t^2}, \tag{A.3}$$

and following, for example Section 10.5 in [73], we arrive at an expression for the frequency doubled radiation intensity through a nonlinear medium of length L and second order susceptibility $\chi^{(2)}$

$$I_{2\omega}(L) = \frac{\mu_0}{2c} \left(\chi^{(2)} \right)^2 \frac{\omega^2}{n^2(\omega) n(2\omega)} I_\omega^2(0) L^2 \text{sinc}^2 \left(\frac{1}{2} \Delta k L \right), \tag{A.4}$$

where μ_0 is the permeability of free space, $n(\omega)$ is the refractive index at the fundamental frequency, $I_\omega(0)$ is the fundamental intensity at the entrance of the nonlinear medium and $\Delta k L =$

$(2k_\omega - k_{2\omega})L$ is represents a phase mismatch between the fundamental and doubled frequencies at the output of the medium.

Phase matching between the two wavelengths is required to produce optimal conversion of doubled radiation. Two methods of achieving this are *critical* and *noncritical* phase matching. In the case of critical phase matching, the nonlinear crystal is angle tuned to adjust the index of refraction of the optical axis. With noncritical phase matching, the indices are tuned by adjusting the temperature of a crystal, usually within some sort of crystal oven.

In the case of the ATRAP system, a lithium triborate (LBO) crystal was used for the frequency doubling stage. Critical phase matching was performed by fixing the crystal on a tip-tilt stage and adjusting the axes with respect to the input 729 nm beam until maximum 365 nm pulse energy was achieved. Typical pulse energies of 70 mJ at 729 nm could produce about 21 mJ of 365 nm energy, resulting in a single-pass conversion efficiency of 30%.

LBO crystals are slightly hygroscopic, meaning they tend to absorb water, which can lead to a reduction in harmonic conversion efficiency. Therefore, the crystal was also contained in a small acrylic housing and purged with dry nitrogen as shown in Fig. A.4.

Frequency Tripling

Generating third-harmonic radiation is similar to that of second-harmonic as described above, except a third multiple of the fundamental frequency along with the third-order susceptibility $\chi^{(3)}$ are considered. The intensity of third-harmonic radiation produced is proportional to square of the number density N of the nonlinear gas medium [74]:

$$I_{3\omega}(L) \propto \left(\chi^{(3)}\right)^2 N^2 I_w^3(0) \left(\pi b \Delta k\right)^2 \mathrm{e}^{b\Delta k}, \tag{A.5}$$

where b is the confocal beam parameter (twice the Rayleigh range) and Δk is the phase mismatch. While based on this approximate expression, simply increasing the gas density will produce higher conversion rates, there are other factors which limit the production of harmonic generation. In this case, the gas medium that is responsible for harmonic generation is krypton (Kr), which has

a fairly low dielectric breakdown constant – limiting the intensity of the fundamental radiation source and thus the conversion efficiency. If, for example, a looser focus is made through the gas to compensate for a lower intensity, then the natural dispersion of Kr will lead to a large phase mismatch and again result in low conversion efficiency.

To remedy the phase mismatch problem, a buffer gas can be introduced as a mixture to counteract the dispersion of Kr. Both xenon (Xe) and argon (Ar) have been used [69–72] to this end and Ar has shown larger gains in conversion efficiency. Measurements were performed to optimize the partial pressures as well as total pressure of the mixture to generate as much 121 nm radiation as possible. As shown in Fig. A.5, a conversion efficiency peak was found at about 1.5 bar total pressure with an Ar/Kr partial pressure ratio of 2.3. At these values, 190 nJ per pulse were produced at 30 Hz, resulting in an average power of 5.7 μW.

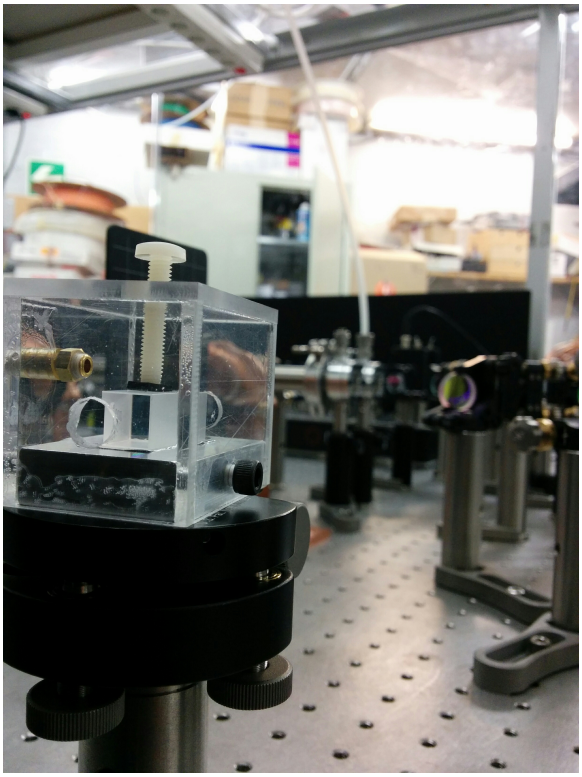

Figure A.4: Picture showing the tip-tilt mounting stage and dry nitrogen purge setup for the LBO crystal used for single-pass frequency doubling.

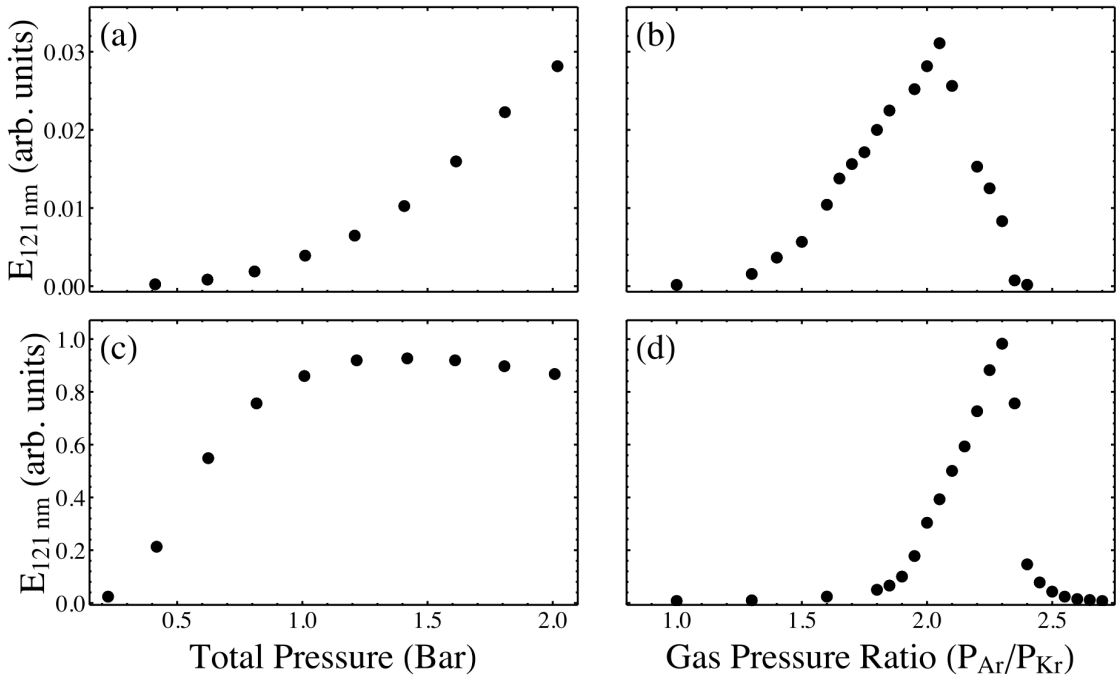

Figure A.5: Optimization data for frequency tripling cell partial pressures of krypton and argon.

A.2.4 Results

The pulse duration of the 121 nm radiation is 16 ns, resulting in a transform-limited Gaussian spectral bandwidth of 27.5 MHz. Since the natural linewidth of the $1S_{1/2} - 2P_{1/2}$ line is 100 MHz, the radiation we produced would be sufficient for laser cooling. A second gas cell was created and mounted directly on the ATRAP apparatus in order to reduce the number of optics the Lyman-α radiation must interact with before reaching the antihydrogen atoms. We estimate that after optical losses, about 200 nW would be delivered to the trapped antihydrogen atoms, which would cool them from 170 mK down to 17 mK on the order of an hour.